AWS-TR-74-250

DUGWAY P...
TECHNIC.L ...

AIR WEATHER SERVICE

DEFENSE METEOROLOGICAL SATELLITE PROGRAM (DMSP) USER'S GUIDE

PUBLISHED BY
AIR WEATHER SERVICE (MAC)
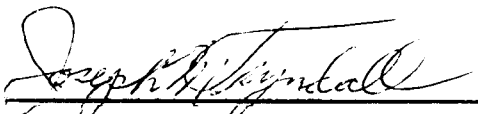**UNITED STATES AIR FORCE**
1 DECEMBER 1974

This report approved for public release. There is no objection to unlimited distribution of this report to the public at large, or by DDC to the National Technical Information Service (NTIS).

This technical report has been reviewed and is approved for publication.

CHESTER C. LUKAS, Colonel, USAF
Director, Aerospace Services Directorate
DCS/Aerospace Sciences

FOR THE COMMANDER

JOSEPH M. TYNDALL, Colonel, USAF
DCS/Aerospace Sciences

DOCUMENT UNCLASSIFIED JCP-I,DPG

DISCLAIMER NOTICE

This document may contain pages which do not reproduce legibly. Inconsistent page numbers are due to omittance of blank pages.
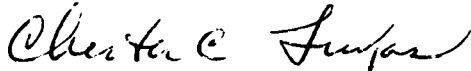
DOCUMENT UNCLASSIFIED JCP-I,DPG

REPORT DOCUMENTATION PAGE		READ INSTRUCTIONS BEFORE COMPLETING FORM
1. REPORT NUMBER AWS TR-74-250	2. GOVT ACCESSION NO.	3. RECIPIENT'S CATALOG NUMBER
4. TITLE *(and Subtitle)* Defense Meteorological Satellite Program (DMSP) User's Guide		5. TYPE OF REPORT & PERIOD COVERED
		6. PERFORMING ORG. REPORT NUMBER
7. AUTHOR*(s)* Major Lee G. Dickinson, HQ Air Weather Service; Capt S. Edward Boselly III and Capt Walter S. Burgmann, USAFSAAS, Dept of Weather Training		8. CONTRACT OR GRANT NUMBER*(s)*
9. PERFORMING ORGANIZATION NAME AND ADDRESS Headquarters Air Weather Service Scott AFB, Illinois 62225		10. PROGRAM ELEMENT, PROJECT, TASK AREA & WORK UNIT NUMBERS
11. CONTROLLING OFFICE NAME AND ADDRESS Headquarters Air Weather Service Scott AFB, Illinois 62225		12. REPORT DATE December 1974
		13. NUMBER OF PAGES 109
14. MONITORING AGENCY NAME & ADDRESS*(if different from Controlling Office)*		15. SECURITY CLASS. *(of this report)* Unclassified
		15a. DECLASSIFICATION/DOWNGRADING SCHEDULE

16. DISTRIBUTION STATEMENT *(of this Report)*

Approved for public release; distribution unlimited.

17. DISTRIBUTION STATEMENT *(of the abstract entered in Block 20, if different from Report)*

18. SUPPLEMENTARY NOTES

19. KEY WORDS *(Continue on reverse side if necessary and identify by block number)*

DMSP
Meteorological Satellite

20. ABSTRACT *(Continue on reverse side if necessary and identify by block number)*

The capabilities of the spacecraft, sensors, and data processor for the Defense Meteorological Satellite Program are described. Many meteorological and geophysical uses of these data are examined, and examples used to illustrate the capabilities of the system to tailor the imagery for a large variety of present and future users.

DD FORM 1473 1 JAN 73   EDITION OF 1 NOV 65 IS OBSOLETE

Defense Meteorological Satellite Program (DMSP) User's Guide

PREFACE

The eyes of the meteorological world were opened to a view from space when the first NASA experimental weather satellite, TIROS-I, was launched on 1 April 1960. Several generations of satellites have come and passed since then, each one an improvement on its predecessor. On 6 March 1973 Dr. John L. McLucas, Under Secretary of the Air Force (now Secretary of the Air Force), announced that meteorological satellite imagery from the Air Force Defense System Applications Program (DSAP) satellite was to be made available to the world's community of meteorologists. Data from this system were called Data Acquisition and Processing Program (DAPP) data. Both the DSAP and DAPP names have since been superseded by Defense Meteorological Satellite Program (DMSP). DMSP is a total system involving sensors, data communications, and ground processing equipment. Information on all the components of the system is necessary to be able to understand and apply DMSP data to meteorological problems. This Technical Report describes the DMSP system and some of its applications for the Air Force Air Weather Service.

This report could not have been written without the help of many persons in several USAF commands. The greatest credit goes to Major L. G. Dickinson, HQ Air Weather Service, Aerospace Sciences Deputate, Scott AFB, IL, and two former personnel of USAFSAAS, Department of Weather Training, Chanute AFB, IL, on duty at the Air Training Command DMSP School, Keesler AFB, MS. Instructors Captain S. E. Boselly, III, and Capt W. S. Burgmann wrote major portions of the original DAPP User's Guide, and contributed hundreds of hours in transcribing their collective knowledge of DMSP into the drafting and editing of this technical report. A former instructor of the DMSP School, Capt D. D. Waltman, was responsible for much of the editing and proof reading in the original DAPP User's Guide and several of the data application examples presented herein. Credit also goes to the maintenance technicians of the DMSP School for operating the display equipment and producing most of the data examples used in the Technical Report. Mr. Robert L. Sempek of Aerospace Corporation photocopied most of the data examples and processed them into the proper format for insertion into the master manuscript. Mrs Mildred A. Revoire typed and retyped this manuscript several times. Many AWS individuals at DMSP sites around the world contributed examples of techniques they developed to apply these data to meteorological problems. Without their work DMSP data would just be data. It is their application of DMSP data to operational problems requiring meteorological support that is the most important link in the chain from spacecraft to support for the operational commander.

CHESTER C. LUKAS

CHESTER C. LUKAS, Colonel, USAF
Director, Aerospace Services Dir.
DCS/Aerospace Sciences

TABLE OF CONTENTS

Figures

Where satellite data are shown, the legend for the figures takes the following formats:

A. Visual data

13 Dec 1972, 6530/487, HR, Norm, Norm, Off.

Where:

13 Dec 1972 = date of the data.

6530 = spacecraft number.

487 = number of revolutions around the earth the spacecraft has completed since launch.

HR = data type, either HR or VHR

Norm = scale of the data. Norm is 1:15,000,000. Exp L, Exp C, Exp R (standing for expand left, center, or right-hand portions of the data) are 1:7,500,000.

Norm = polarity of the data. Norm means dark objects are displayed as dark and light objects as light. Inv means dark objects are displayed light, and light objects are dark.

Off = enhancement mode. Off means a linear distribution of the shades of gray. Low means that more contrast is present in the dark end of the gray scale. High means that more contrast is present in the light end of the gray scale. Low/High means that both ends of the gray scale have more contrast at the expense of middle-gray shades.

B. Infrared data.

1. Brilliance Inversion type.

13 Dec 1972, 6530/487, WHR, Norm, Inv 310 X1, Off

Where:

13 Dec 1972, 6530/487 = same as for visual data

WHR = data type, either WHR or MI.

Norm = scale of data, same as for visual data.

Inv 310 X1 = polarity of data. Inv means cold objects displayed light, warm objects displayed dark. Norm means cold objects displayed dark, warm objects displayed light. 310 X1 means that 64 shades of gray are spread over the 100 degree interval from 210 - 310K. 300X2 means that 32 shades of gray are spread over the 50 degree interval from 250 - 300K. 310X4 means that 16 shades of gray are spread over the 25 degree interval from 285-310K.

Off = enhancement mode, same as for visual data except that Off is the preferred enhancement mode for infrared data.

2. Threshold Type

19 Apr 1973, 5528/5536, MI, Norm, Thresh Inv, 285-275-266.

Where:

19 Apr 1973, 5528/5536, MI, Norm = same as for base type infrared data.

Thresh Inv = thresholding mode selected where coldest temperature selected appears as lightest gray shade, warmest temperature selected appears as darkest gray shade.

285-275-266 = temperatures selected for thresholding process. For this example all radiating objects 285K and warmer are displayed as black. All radiating objects from 275 to just under 285K are displayed as a dark shade of gray. All radiating objects from 266 to just under 275K are displayed as a light shade of gray. All radiating objects colder than 266K are displayed as white.

If the Thresh Norm mode had been selected, then the order of gray shade would have been reversed. (e. g., ≥ 285 = white, 275 to nearly 285K = light gray, 266 to nearly 275K = dark gray, < 260K = black)

DOCUMENT UNCLASSIFIED JCP-I,DPG

DOCUMENT UNCLASSIFIED JCP-I,DPG

Defense Meteorological Satellite Program (DMSP)

User's Guide

Chapter 1 - Introduction

Data from the Defense Meteorological Satellite Program (DMSP) system became available to the public following two announcements. The first was by Capt Walter D. Meyer, Air Force Global Weather Central (AFGWC), to the 53rd American Meteorological Society Annual Meeting, St Petersburg, Florida on 1 February 1973. The second was by Dr. John L. McLucas, Under Secretary of the Air Force, at a press conference at The Pentagon, 6 March 1973. At these announcements it was stated that DAPP meteorological sensors are carried on board a Department of Defense satellite program to provide responsive, operational meteorological data to the Air Weather Service (AWS) to enhance the AWS's ability to meet its military commitments. It was later identified that the total satellite and sensor program was the Defense Meteorological Satellite Program.

The mission for DMSP is to:

1. Provide globally recorded visual and infrared cloud cover and other specialized environmental data to the Air Force Global Weather Central (AFGWC), Offutt AFB, NE.

2. Provide real time direct readout of local area environmental data to mobile receiving terminals at key locations throughout the world.

3. Continue the advancement of environmental satellite technology to meet Department of Defense requirements.

The DMSP User's Guide is designed to provide military meteorological personnel working with this data an introductory and reference publication for use in their application of the data.

Global DMSP data received and processed at AFGWC are furnished to the Department of Commerce's National Oceanic and Atmospheric Administra-

tion. Public requests for future data may be sent to:

National Oceanic and Atmospheric Administration, National Environmental Satellite Service - S Federal Office Building No. 4 Suitland, MD 20233

AFGWC DMSP data are archived for NOAA at the University of Wisconsin's Space Science and Engineering Center. The archival starting date was 23 February 1973. Requests for these data may be sent to:

Mr. Thomas Haig 10th Floor ATS-SMS Library Space Science and Engineering Center 1225 West Dayton Street Madison, Wisconsin 53706

Direct readout DMSP data from the tactical sites are also available from the University of Wisconsin. The archival starting date was 1 November 1973.

The nighttime visual DMSP imagery from AFGWC showing the aurora have been microfilmed by NOAA's National Geophysical and Solar-Terrestrial Data Center (NGSDC) in Boulder, CO. Microfilm and photographic copies are available from June 1972. Requests for microfilm or photographic paperprint copies may be sent to:

Mr. Herb Kroehl National Geophysical and Solar Terrestrial Data Center NOAA Boulder, Colorado 80302

This DMSP User's Guide is not intended to replace the Air Weather Service Technical Report 212, "Application of Meteorological Satellite Data in Analysis and Forecasting," June 1969. The basic interpretation techniques are valid for both conventional meteorological satellite data and DMSP data. However, DMSP data have several unique

characteristics that were not touched upon in the earlier report. These characteristics plus the startling detail apparent in one-third nautical mile (nm) spatial resolution imagery are described in later chapters.

The U S Air Force Weather Service DMSP data are now a part of the public domain. We encourage full exploitation of this national resource.

Chapter 2 - Sites

The prime DMSP site is at the Air Force Global Weather Central (AFGWC), Offutt AFB, Nebraska. Analog data from the spacecraft's tape recorders are read out to tracking sites at Fairchild AFB, Washington, and Loring AFB, Maine. These two sites do not display or process the DMSP data. Their role is to relay the satellite data "dump" over special wide band communications lines to AFGWC. Most of these data are relayed to AFGWC as they are received; however, some are relayed later from tape recordings made at the time of data dump. Global coverage of the world's weather is received and processed by AFGWC twice daily for each spacecraft. These data, both from the primary imagery sensors and supplementary sensors, are used to provide major inputs to the Three-Dimensional Nephanalysis, Space Environmental Support System, current weather operations, numerical prediction models, classified special projects, and other tasks too numerous to list. A Navy Detachment at AFGWC forwards selected DMSP data to the Navy's Fleet Numerical Weather Central in Monterey, CA. AFGWC also acts as a transmission site for relaying DMSP, and other data via the Digital Facsimile System (DFS) network to DFS receivers at The Pentagon and Langley AFB, Virginia.

There are three other Air Force readout sites in the conterminous United States. These are tactical readout sites not connected with AFGWC. The Vandenberg AFB, California site is not a full time operational site. It is contractor operated and used for spacecraft and sensor checkout prior to and after a DMSP launch. Forecasters and maintenance technicians are trained at the Keesler AFB, Mississippi site. Operational support is provided to the Air Force

Weather Service "hurricane hunter" unit and other agencies at Keesler AFB on an "as needed and equipment availability" basis. The remaining site is at McClellan AFB, California. It is the Intermediate Maintenance Shop for most DMSP aerospace ground equipment. One of the tactical vans located there is kept ready for air deployment to support any contingencies that may occur.

The U S Navy currently has one site. It is a semi-permanent site built into the aircraft carrier Constellation. Other aircraft carriers will be DMSP equipped over the next several years.

Nine other Air Force tactical sites are scattered about the world. They are:

Hickam AFB, Hawaii
Elmendorf AFB, Alaska
Nakhon Phanom AB, Thailand
Patrick AFB, Florida
Fuchu AB, Japan
Ramstein AB, Germany
Howard AFB, Canal Zone
Kadena AB, Okinawa
Nimitz Hill, Guam

All the Navy and Air Force tactical sites are configured to read out digital, encrypted DMSP data. Their missions are diverse, because in general, they provide tailored data in support of the decisionmakers for the commands they serve.

The tactical sites are mobile. One should not assume that the site locations listed are fixed. They have moved several times in the past, and can be expected to do so again to support Department of Defense needs for weather information in a changing world.

Chapter 3 - Sensors

A.   Primary Sensors.

     The primary sensors used to ob-
tain DMSP Data are contained in a
sensor AVE (aerospace vehicle
electronics) package (SAP). The SAP
is mounted on the DMSP so that with
nominal spacecraft attitude control
the sensors are always oriented
toward the earth. These sensors are
scanning radiometers which respond
to amounts of radiation within
specific spectral ranges. Two types
of data are obtained: visual data,
which is a measure of reflected
solar radiation; and infrared data,
which is a measure of emitted earth
and cloud radiation.

     The spectral interval used for
obtaining visual data is 0.4 - 1.1
micrometers (μm). Figure 3-1 depicts
the sensor's nomalized response
curve for this spectral range. It
shows that the sensor reacts as if
there was a minus blue filter block-
ing most of the response in the blue
end of the spectral range. This

minimizes the blue light backscatter-
ing of the atmosphere and allows good
contrast between dark objects in the
earth scene, such as terrain and
water boundaries.

     The response at the other end of
the spectral range is a result of the
type of detector used. A silicon
detector is used in order to sense
small amounts of radiation in the
visual spectrum. Its natural response
provides sensing into the near infra-
red. However, the radiation sensed
primarily is still reflected solar
radiation. Two benefits are derived
from this response: First, vegetation
is more reflective at wave lengths
longer than 0.7 μm than it is for
shorter visible wavelengths, which
provides good vegetation, soil, or
water contrasts. Secondly, it allows
good sensor response to lunar illumina-
tion. The lunar radiation curve
approximates the emission from a 4000K
blackbody. This emission peaks inside
the sensor's response range. The
earth scene under lunar illumination
is therefore more perceptible than it
would be for a sensor whose response
approximates the human's eye. The
sensor's half power response points
are at 0.57 μm and 0.97 μm.

     In order to sense infrared radia-
tion, a thermister bolometer, combined
with filtering, is used to respond in
the 8 - 13 μm spectral range. The
sensor response curve approximates
that in Figure 3-1 except the abscissa
would be labelled 8 - 14 μm rather than
0.4 - 1.2 μm. The 8 - 13 μm range is
used primarily because it contains the
peak radiations emitted by the earth
and its atmosphere. The broad spectral
range was selected so that the field
of view of the detector could be
narrowed to obtain good spatial
resolution while still maintaining
a good signal-to-noise ratio at the
detector. A fortunate by-product of
this spectral interval is that nearly
all cirrus, even that just barely
visible to a ground based observer, is
detected by the sensor.

Fig 3-1.   Normalized sensor response
           for a simulated solar
           radiation source.

     The SAP consists of two scanning
radiometers. One is a two-channel

DOCUMENT UNCLASSIFIED JCP-I,DPG
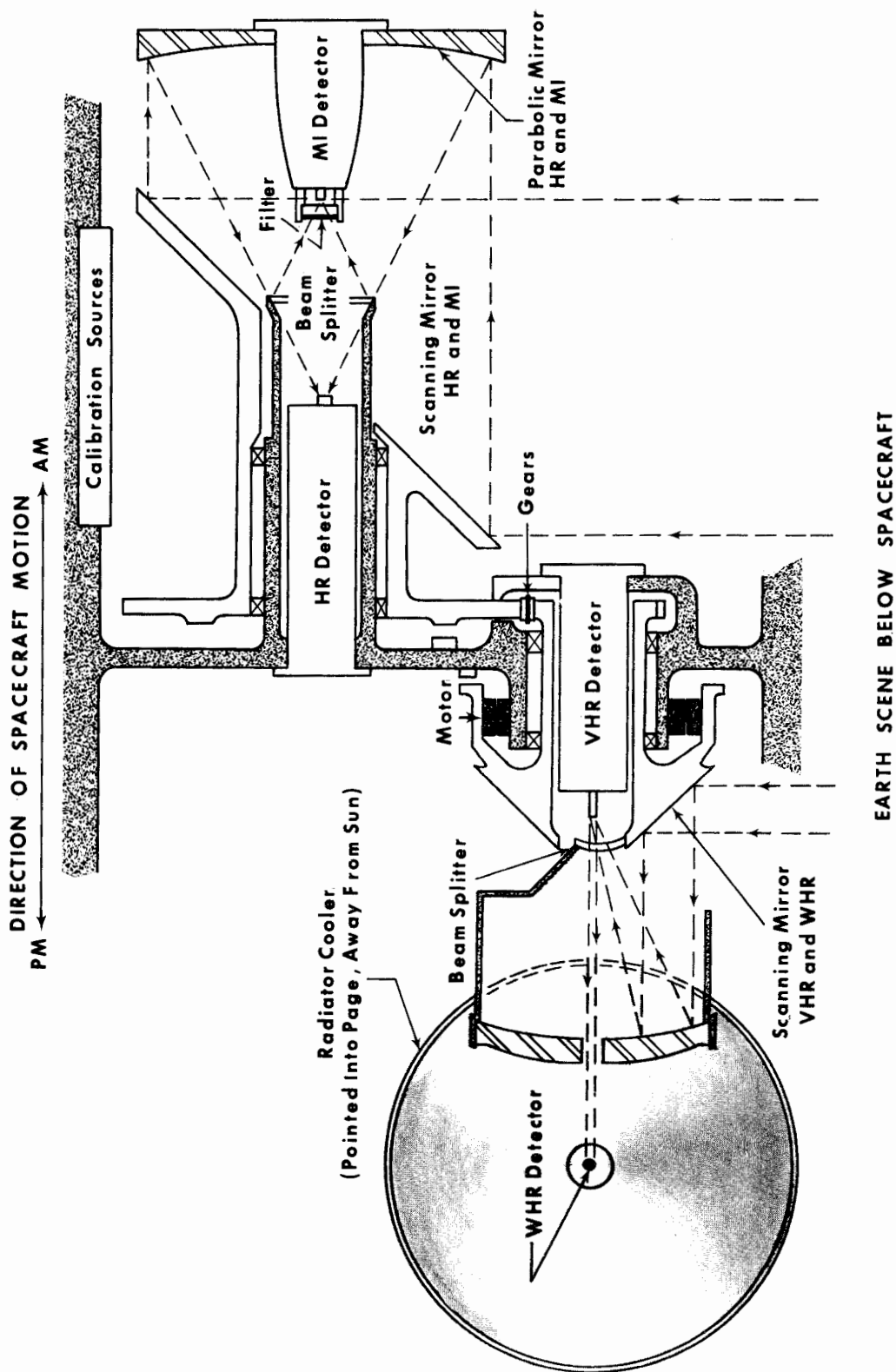
Fig 3-2. DMSP Scanning Radiometer Optics

scanner for high resolution (HR) visual and mode infrared (MI) data; the other scanner is a two-channel device for very high resolution visual (VHR) and very high resolution infrared (WHR) data. Each radiometer consists of a mirror mounted on a shaft which rotates such that the mirror (which is mounted 45° to the direction of motion) scans the earth scene from horizon to horizon (See Figure 3-2). The VHR/WHR shaft revolves at 5.34 hertz (HZ). The mirror on the shaft is double-faced so that for each shaft revolution two scans are made of the earth scene. This scan rate combined with a 0.766 milliradian field of view from 450 nm, gives a spatial revolution of 0.33 nm at subpoint.

The HR/MI scanner is driven by a 3:1 reduction gear from the VHR/WHR shaft and revolves at 1.78 HZ. Since this mirror is single-faced and rotates at one-third the speed of the VHR/WHR mirror, only one-sixth the number of scan lines are produced.

This scan rate, combined with a 4.56 milliradian field of view, provides 2.0 nm resolution visual data at subpoint. The MI detector has a 5.33 milliradian field of view which yields 2.4 nm resolution infrared data. For either radiometer the incoming scene radiation is reflected from the scanning mirror to a parabolic mirror which, in turn, focuses that radiation onto a dichroic beam splitter. The beam splitter allows visual spectrum radiation to pass without reflection, while at the same time reflecting infrared radiation. The visual radiation is collected at the respective HR and VHR detectors, and the infrared radiation is collected at the MI and WHR detectors.

In order to obtain the proper spatial resolution the detectors for VHR and WHR are physically smaller than their counterparts for HR and MI radiation. Consequently, for visual radiation, the VHR data are only available during the daytime where there is sufficient reflected solar illumination of the earth scene
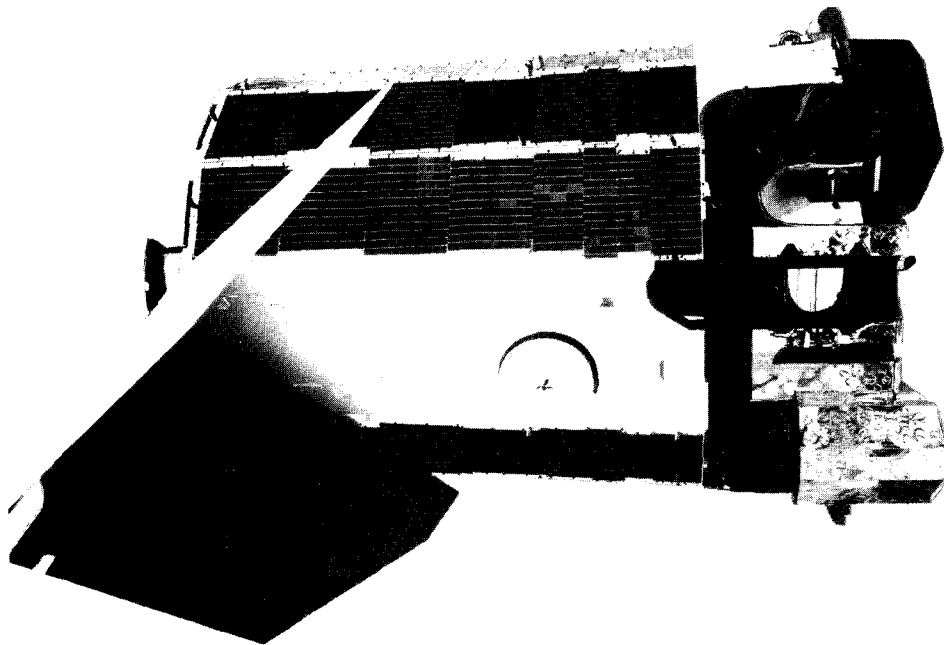
Fig 3-3. Defense Meteorological Satellite Program satellite and sensors

to provide an adequate signal-to-noise ratio at the detector. (The light level under full sunlight is between five and six orders of magnitude greater than full moonlight). For infrared data there is little difference between the total amount of radiation emitted from the earth during day or night. However, due to the fact that a different type of detector is used than for VHR or HR, and the WHR detector area is approximately 1/36th that of the MI detector, a greater signal-to-noise ratio problem exists than with the other sensors. In order to accurately discern the small amounts of infrared energy available to the WHR detector, it is passively cooled using a radiational cooling patch so that the thermal noise of the detector is reduced and does not obscure the scene radiation.

Figure 3-3 is a photograph of the Defense Meteorological Satellite Program (DMSP) satellite with the sensors mounted near the bottom of the spacecraft (right). The white face on the spacecraft is earth oriented and therefore the sensors on the right are earth oriented. The top of the spacecraft (left)

always is oriented toward the sun. The panels on the left form a sun shade which shields the SAP when the spacecraft is in an early morning orbit. In this orbit, near the poleward portion of each revolution, there is a possibility of direct sunlight impinging on the sensors.

The specific details of the sensor package are more readily apparent in the cutaway drawing, Figure 3-2. However, the shiny box-like structure in the lower right contains the radiative cooler for the WHR detector. The cooler is pointed to the right, away from the sun. Above the cooler is a narrow aperture in which the VHR/WHR wedge-shaped mirror rotates. Just above the narrow aperture is the larger opening for the HR/MI scanning mirror. Of interest is the fact that these mirrors are precisely weighted and rotate in opposite directions so that there is no net momentum transfer to the spacecraft from their operation. The circular area on the white face to the left of the sensors, contains the antenna for the data transmitter.

Not seen in the picture, but extremely important to data production, is a unique feature in this
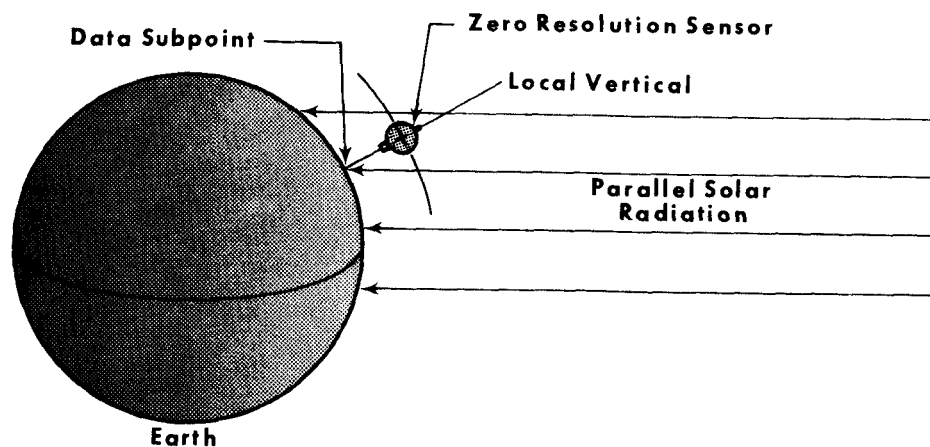
Fig 3-4.   Relationship between zero-resolution sensor and data subpoint. Incident solar radiation at each place is essentially identical.

system. A zero-resolution, super hemispheric radiometer is mounted 180° away from the SAP nadir. This radio-meter measures the amount of sunlight incident on the spacecraft, and, with the earth oriented sensor system, essentially measures the solar illu-mination of the earth scene at the data subpoint (see Fig. 3-4). The output from this radiometer, in conjunction with a programmable gain memory unit, controls the signal level output for the visual data. In other words, the visual data received at tactical sites and AFGWC are normal-ized on the spacecraft for solar illu-mination. The data appears to have the same brightness whether from near the solar subpoint or near the terminator. Crossing the terminator, however, causes additional problems.

line A-A' (see Figure 3-6) the scene on the left begins to get progres-sively darker and the area of dark-ness expands. When the data subpoint reaches the terminator, half of the sensor scan is in the dark area and half in the light. At this point, scanning from horizon to horizon, the brightness change from far left to far right is spread over 26.8° longitude at the equator. This is a brightness change of six orders of magnitude. In order to receive mean-ingful data across the terminator, one must have more than the along-track gain control provided by the zero resolution sensor, one must also have along scan gain control. In other words, as the sensor scans from dark to light (HR), the gain for each scan line must change as the scanner moves into increasing brightness. As the spacecraft moves further into darkness, the along-scan gain must occur at a different location along the scan line. This compensation also will occur as the spacecraft leaves darkness on the other side of the earth. Additionally, the along-scan gain control must vary season-ally as the orientation of the terminator to the orbit changes.

Fig 3-5.   Orientation of orbit termi-
           nator for a 0600 sun-
           synchronous orbit at
           equinox.

Figure 3-5 shows the orientation of a sun synchronous orbit to the terminator for an 0600 equator cross-ing at equinox. Notice how the sensor will have to scan from horizon to horizon through full brightness in the southern hemisphere progressing to full darkness in the northern hemi-sphere. Once the spacecraft reaches

Fig 3-6.   Data swath across the
           terminator from AA' to
           BB' in Figure 3-5.
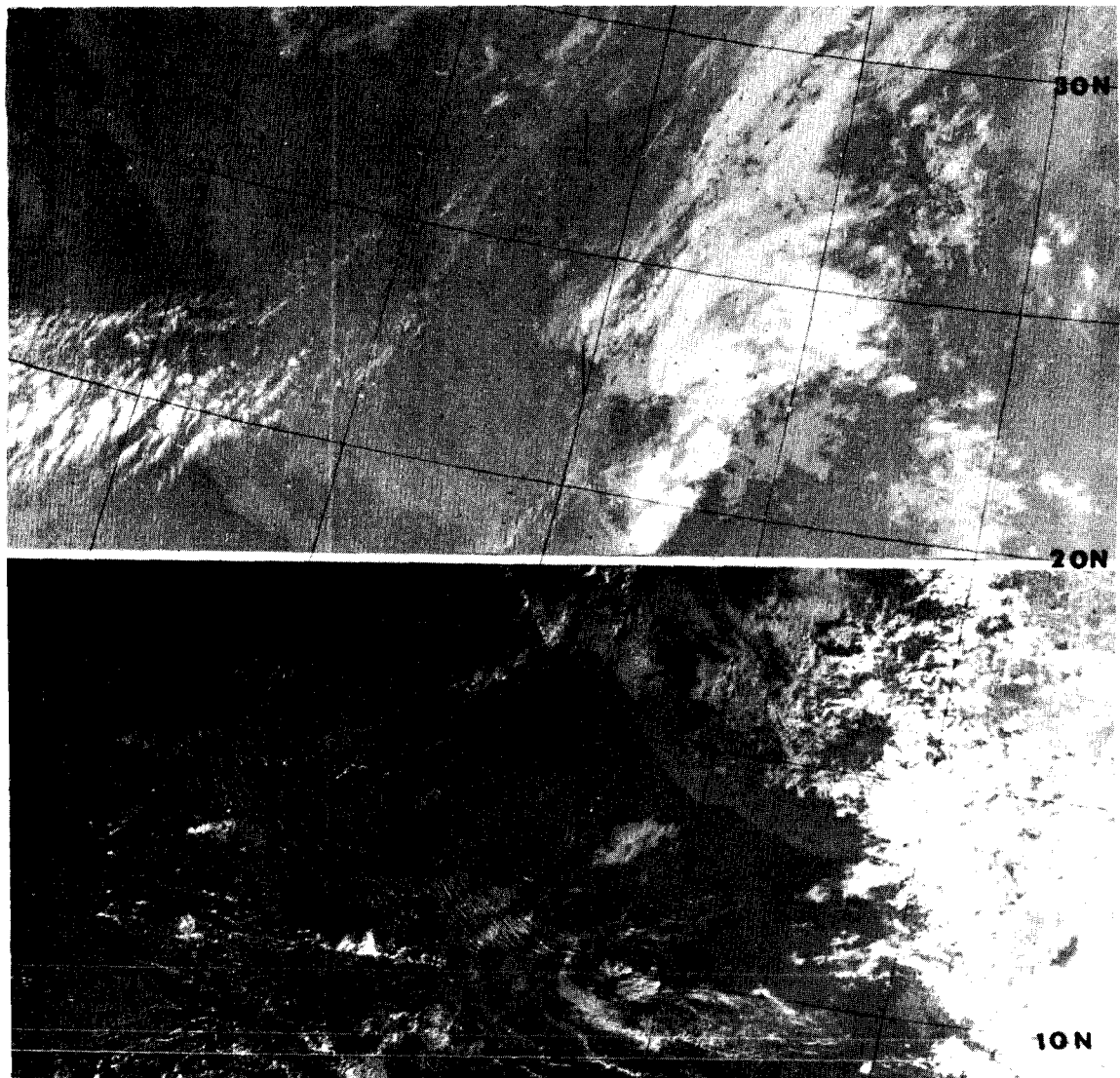
Fig 3-7.   13 Dec 1972, 6530/487, VHR (Bottom), Norm, Norm, Off; WHR
           (Top), Norm, Inv 310 Xl, Off

Figure 3-7 is an example of DMSP data obtained 13 Dec 72. At the bottom of Figure 3-7 is VHR data. Notice in the upper left corner of the VHR data there is essentially only darkness as the spacecraft is approaching the terminator. Near 18°N the spacecraft was programmed to stop transmitting VHR data and to start WHR data (Fig 3-7 top) which is not affected by lack of solar illumination. Figure 3-8 is HR data which was obtained at the same time. Notice the changes in brightness occurring in the upper left. This is the along scan automatic gain control (ASAGC) compensating for the decreasing scene brightness. With the ASAGC, useable information is available through the sun terminator region and beyond if there is sufficient moonlight to illuminate the clouds.
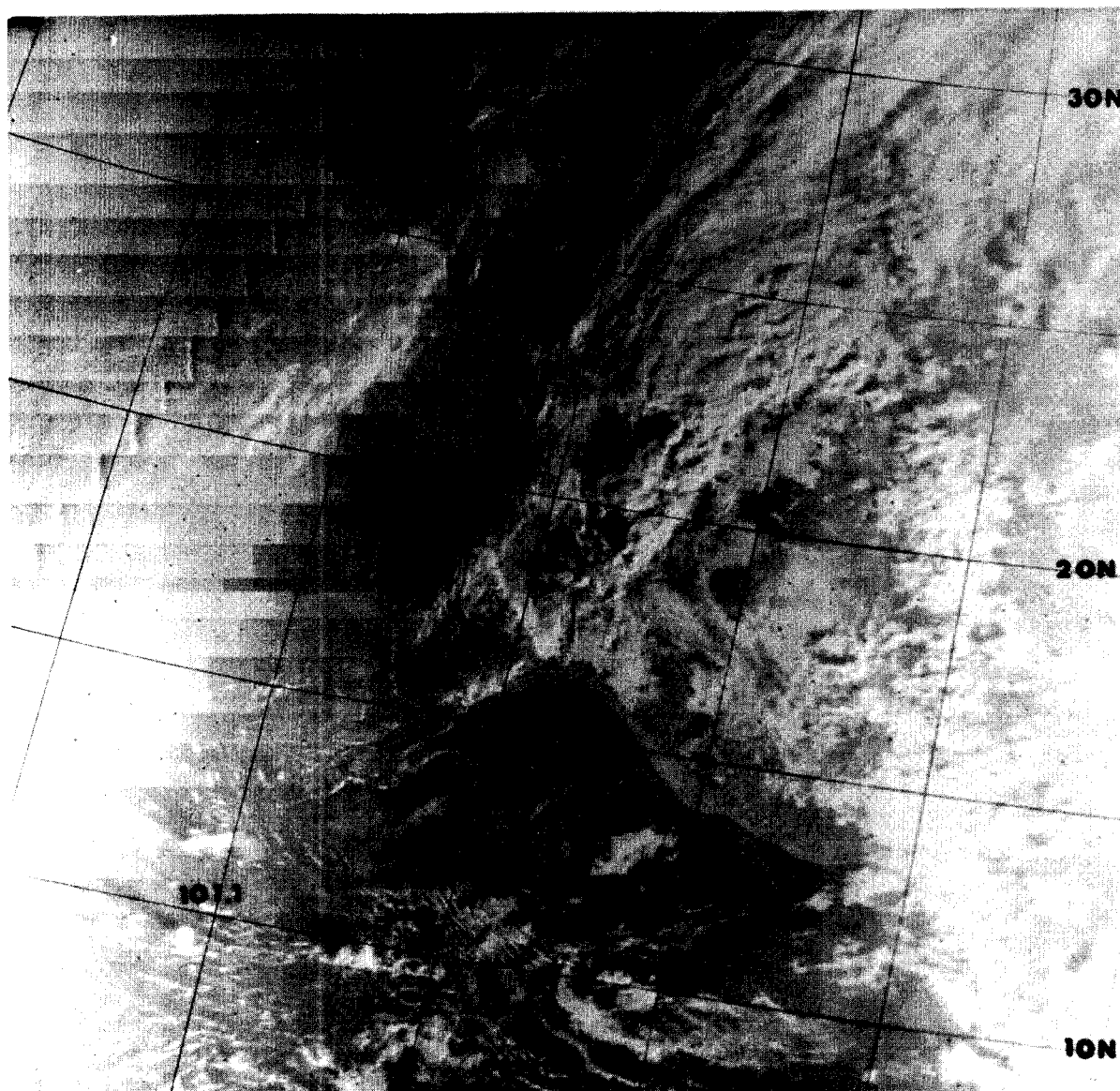
Fig 3-8. 13 Dec 1972, 6530/487, HR, Norm, Norm, Off

B. Supplementary Sensors.

There are four supplementary
sensors which go on the DMSP space-
craft. Normally each DMSP carries
two supplementary sensors, the exact
complement differing according to
the time period the orbit is planned

for, and the condition of the various
supplementary sensors on older space-
craft.

Supplementary sensor E (SSE) is
a vertical temperature profile radio-
meter. It is an eight channel
instrument with six channels (668.5,

677, 695, 708, 725, and 747 cm^{-1}) in the carbon dioxide 15 μm absorption region; one channel (535 cm^{-1}) in a water vapor absorption band; and one channel (835 cm^{-1}) in the 11 μm atmospheric window. A scanning mirror steps across the subtrack of the satellite, allowing the SSE to view 25 separate columns of the atmosphere every 32 seconds over a cross-track ground swath of 100 nm. While the scanning mirror is stopped at a scene station, the channel filters are totaled through the field-of-view. The detected radiation is measured by a tri-glycine pyroelectric detector. Surface resolution at nadir for the SSE half power points is approximately 20 nm.

Supplementary Sensor J (SSJ) is an electron spectrograph with one fixed channel and one stepping channel. The channels detect energetic electrons over ranges of energies associated with visible aurora. The fixed channel is 6 KeV and the stepping channel cycles through eight energy thresholds: 54, 98, 219, 600, 1400, 3540, 8200, and 1970 eV. The data sample is taken approximately every second. The field-of-view is 3 degrees by 12 degrees.

SSJ has been improved. The second generation is called SSJ/2. It

consists of a single stepping channel with six energy ranges. Nominal energy steps are 0.3, 0.68, 1.6, 3.5, 7.9, and 18 KeV. The sampling rate is 0.0922 seconds per energy step and the field of view is a 30 degree anti-earth cone.

Supplementary Sensor L (SSL) is a lightning detector. It operates only at night to detect lightning flashes in the 0.4 to 1.1 μm range. Peak response is near 0.8 μm. Twelve silicon photodiodes are used to detect the flashes, each photodiode viewing a different nominal 400 x 400 nm field on the earth's surface. The photodiodes are aligned in a 3x4 array such that the SSL's field of view is 1200 x 1600 nm. The SSL stores the value of the largest pulse observed by each photodiode during a one second sampling interval. The peak pulse and total number of counts per second for each detector makes up the information in the SSL data stream.

The data from all supplementary sensors are low volume, on the order of 100 bits per second. Their data are multiplexed into the primary sensor data stream and recorded on board the spacecraft. No real-time readout is made to tactical sites since some computer processing is necessary for all supplementary sensor data.

Chapter 4 - DMSP Data Display Segment System

A. General

The function of the Data Display Segment (DDS) is to accurately reproduce the image scenes which are viewed by the spacecraft's primary sensors. The DDS electrically processes these data to correct several perspective distortions, and permits the selection of the type and scale of data to be produced. The DDS equipment and operation are described in detail in several SAMSO and AWS documents, the most readily available being a Space and Missile Systems Organization (SAMSO) publication [1]. Several DMSP system capabilities were evaluated and documented during AWS Projects Cold Flight I and Cold Flight II. These projects provide much of the information contained in this section. Operational site experience from several worldwide locations is also incorporated.

There are two types of display systems -- the central site (AFGWC) and the remote or tactical site. The imagery from the two types of display appear similar but, due to different areas of data coverage and formats of data transmission, the two displays differ in their details. AFGWC receives analog data which has been stored on the spacecraft tape recorders. These recorders have a storage capacity of 210 minutes of 2/2.4 nm data or 20 minutes of one-third nm data. Therefore, sometimes several hundred minutes of these data suddenly become available for display. As a result the AFGWC equipment is configured to process a much larger volume than tactical sites. The tactical sites receive only digital, direct transmission data. The maximum amount of data they can receive from an orbital pass is about one-sixth orbit. The following discussion will focus on equipment at the tactical sites. Central site differences, where they exist, will be noted.

B. DDS Equipment

The DDS consists of five assemblies (Figure 4-1): Signal

Processor No 1 (SIG PROC No 1), Signal Processor No 2, converter, and the Power Supply. Additionally, a tape recorder is an integral part of the data processing system. The incoming digital (analog for central site) data stream is recorded on tape so that it can be replayed for display in several formats. For detailed descriptions of the assemblies in the remote site DDS, the reader is referred to [2], which provides the basis for the following information on the two Signal Processors and the Basic Display.

SIG PROC No 1 is the "watchdog" of the DDS. It operates in one of three possible modes: acquisition, tracking, or test. Acquisition and tracking are operational modes; test is an operator initiated maintenance mode.

When an electronic signal enters the DDS, it is verified against a memory circuit in SIG PROC No 1 to insure that only correctly formatted data signals are passed on to the rest of the display -- this is the acquisition mode. If a correct signal is noted, the equipment cycles automatically into the tracking mode. In addition to the "watchdog" function the SIG PROC No 1 also controls the production of the different types of video signals, and four test patterns. These will be discussed later.

In order to correctly reproduce the scene observed by the spacecraft's sensors, the display must duplicate, in correct ratio, two motions of the spacecraft: its movement through the orbit plane, and the cross-track scan of the sensing mirrors (See Chapter 3 for a description of the sensors). The first matching is accomplished by controlling the speed of the film with a capstan drive assembly. The film speed is regulated by the spacecraft altitude setting which the operator dials into SIG PROC No 2. If the spacecraft is at the nominal 450 nm orbit altitude (Figure 4-2), it will take an elapsed time, T, to cross over objects A and B along the ground track. If it is at a higher altitude than the nominal orbit it will take time T + ΔT to
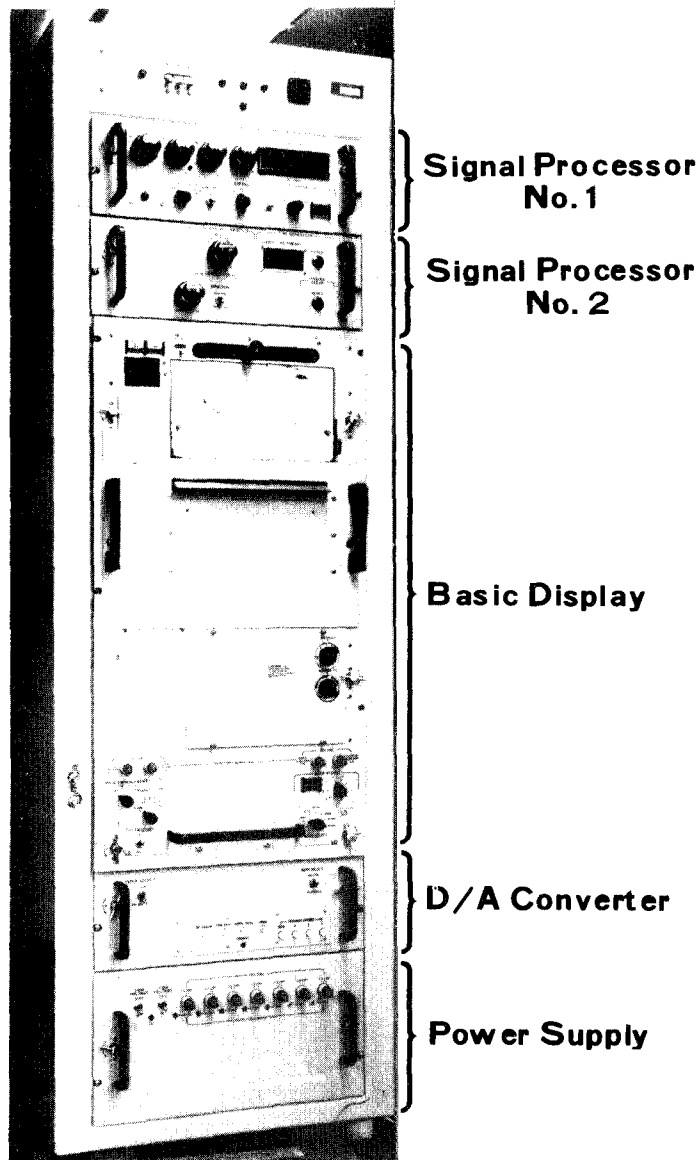
Fig 4-1.. DDS Assemblies

traverse the same two points. If it is lower the elapsed time will be T - ΔT. In all three cases the same ground surface distance is covered. Therefore, to maintain the proper display ratio of scan lines per inch to ground displacement, the altitude settings placed in SIGN PROC No 2 cause the film speed to be faster than normal for a low orbit and slower than normal for a high orbit.

The operator computes either the mean altitude of the spacecraft for the duration of the orbit he will receive, or the specific altitude for the latitude of a particular point of interest. That altitude setting on SIG PROC No 2 results in the genera- tion of a correcting speed trim voltage which is applied to the capstan drive assembly in the basic display. There are two differences in the central

site DDS for matching spacecraft altitude with the ground track distance being traversed: (1) In order to process the large volume of data received, the equipment is geared to operate 21 times faster than a tactical site's, and (2) Since whole orbits or more are processed at a time, the altitude setting is taken care of by a modified SIG PROC No 2. From ephemeris data both apogee and perigee are known for all DMSP spacecraft. Also known is the latitude end point for the last stored data. Given this information the orbital altitude variations are calculated within SIG PROC No 2 assuming the variations approximate a sine wave function. This assumption results in altitude corrected data with minimum data location error throughout an entire orbit.

Fig 4-2. Altitude Variations.

The second matching, that with the scan rate of the sensors' mirrors, is done in the display by the linear sweep generator in SIG PROC No 2. Included in the data stream is a flutter signal derived from the sensors which indicates changes in shaft speed. This flutter signal, when applied from SIG PROC No 1, produces sweep voltage changes to the linear sweep generator which automatically compensate the linear sweep for sensor speed fluctuations.

An operator computed roll correction for the spacecraft can also be set into SIG PROC No 2 which further adjusts the sweep voltage. Finally, the sweep is rectified to compensate for fore-shortening effects (displaying a curved surface on a flat image plane) by curving the sweep voltage at both ends. The curving of the sweep voltage increases the scanning velocity (sweep speed) of the cathode-ray tube (CRT) beam as the beam traverses the CRT face place. As the sweep speed increases, greater distances per unit time are covered, thus compensating for the shortened sensor scan dwell time on those areas removed from the subpoint. After rectification has been applied the sweep voltage is routed to the Basic Display.

The Orbit Time (OT) generator is also located in SIG PROC No 2. This device, which must be manually started at each tactical receiving site for each orbit, is used to provide a timing sequence to aid in correct data location procedures. These procedures will be discussed in Chapter 6. The OT is the only display generated signal which is placed onto the tape recorder. This is done so that the OT clock may be counting for a forthcoming orbit while the display is being used to produce data from a previous orbit. At AFGWC the analog data signal contains timing information from a spacecraft clock which is converted to the time used for data location. This is done by computer.

The Basic Display processes the electronic signals routed to it from the two signal processors and produces a film transparency suitable for direct viewing or reproduction. The Basic Display consists of a scan trace generator and a camera/processor. The scan trace generator transforms the video signal into a modulated light source by way of a high-resolution CRT. The light source, in turn, exposes the film through the camera lens. The camera/processor chemically processes the exposed film to make the film transparency. The film transparencies are produced such that the normal output is a bright image for a maximum amount of sensed radiation. This gives a positive image for visual data; that is, clouds appear white and the earth surface dark. Because most clouds are cooler and radiate less energy than the background, for infra-red data to image white clouds the

input signal must be inverted. The result is a negative infrared image which is directly comparable with the positive visual image. Either visual or infrared data may be produced as a positive or negative image. The data are displayed on mylar backed 9.5 inch wide film so that frequent handling will not degrade the picture quality. The picture width on the film is approximately 7.78 inches. Additional information is placed on the margin of the film. It includes fiducial marks, time code (two minute intervals), gain code (sensor gain state), and data card image (device for recording type of data and display system settings). Up to 35 feet of film can be exposed at a time, and then run through the developer, fixer, rinse tank, and dryer before exiting the DDS. From the time the film starts through the developer until it begins to depart the DDS, 90 seconds elapse.

The Basic Display contains operator controls, equipment status indicators, and control functions. The control functions allow the selection of data type, degree of contrast enhancement, and scale.

1. Control Functions.

As described in Chapter 3, the DMSP sensors produce four basic types of imagery data. Two of these are sensed in the 0.4-1.1 μm spectral interval and are generally referred to as "visual" data. Visual data are the one-third nm very high resolution (VHR) and two nm high resolution (HR). The other two types of DMSP data are in the infrared spectrum's 8 - 13 μm atmospheric window. These data are the one-third nm very high resolution infrared (WHR) and 2.4 nm mode infrared (MI). Each of these four data types and their meteorological applications are more fully discussed in Chapter 7. In producing these data several of the display functions are universal to all products. Other functions are unique to an individual product. The universal control functions have been provided so that DMSP data products may be used by the forecaster to help solve the many varied environmental needs of his customers.

Contrast enhancement is used to vary the distribution of gray shades in these data. The four

enhancement modes are graphically shown in Figure 4-3, and pictorially, using gray shade step wedges, in Figure 4-4. DMSP data are normally processed to show 16 shades of gray spread linearly over the maximum signal range of three volts. This linear distribution of voltage vs gray shade is called OFF ENHANCEMENT (OFF ENH). This mode may be used with all of the types of DMSP data and is the only enhancement which should be used with infrared data. In LOW ENH the linear distribution of gray shades is changed so that more contrast is present in the dark range than in the light range. This mode is useful in highlighting terrain detail or in showing the structure of relatively low albedo objects such as thin fog and stratus. HIGH ENH is the opposite of LOW ENH. In this mode the linear distribution of gray shades is changed so that more contrast is present in the light range than in the dark range. The topside structure of cirrostratus, penetrating towers in cumulonimbus, and other high-albedo objects may be examined by using this mode. In the LOW/HIGH ENH mode both dark and light objects are emphasized at the expense of the middle shades of gray. This setting can be useful in analyzing thunderstorm activity over land by permitting analysis of the anvil structure as well as the terrain features.

All types of DMSP data may be displayed in either of two scales -- normal, 1:15 million (approximately 200 nm per inch), or expand, 1:7.5 million (approximately 100 nm per inch). The normal scale may be used with all types of DMSP data and is the preferred scale for HR and MI data. When the expand scale is selected, normally only VHR and WHR data are processed. The expansions are produced by spreading one-half of the data signal over the full width of the CRT, and at the same time advancing the film twice as fast over the capstan drive assembly. Three portions of the signal can be expanded: center half (EXP C), left half (EXP L), or right half (EXP R). Left and right are defined with respect to the along subpoint track motion of the spacecraft (e. g., for northward moving spacecraft left is west and right is east).

2. Data Types

Four types of data are

DOCUMENT UNCLASSIFIED JCP-1,DPG
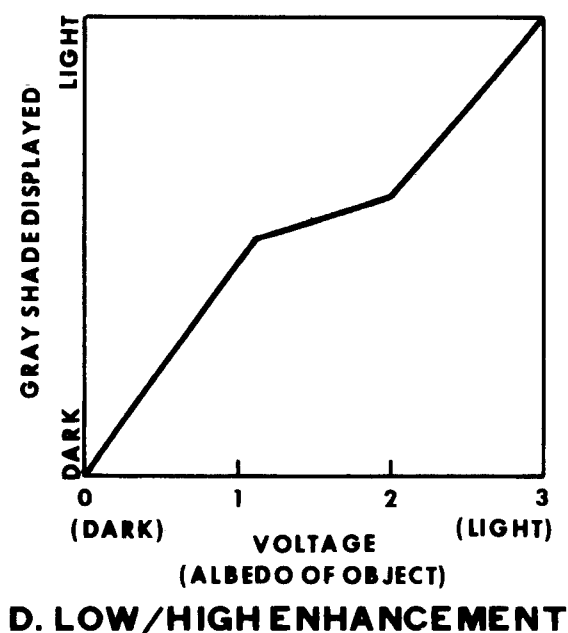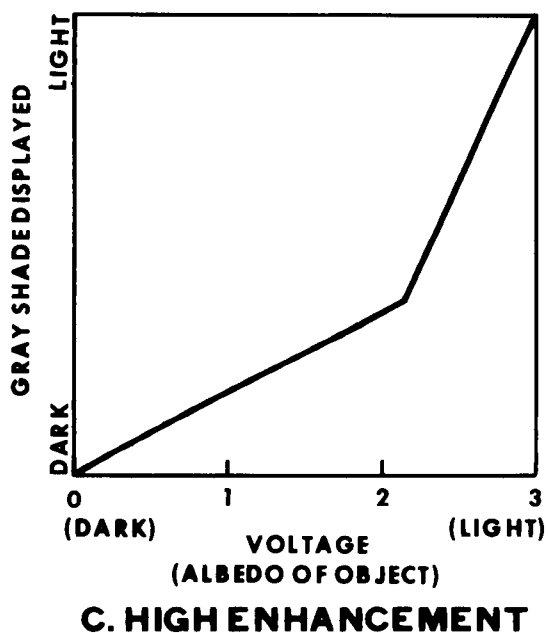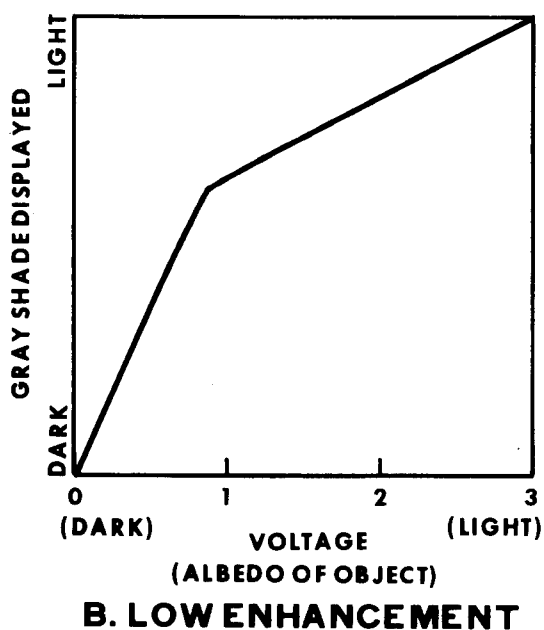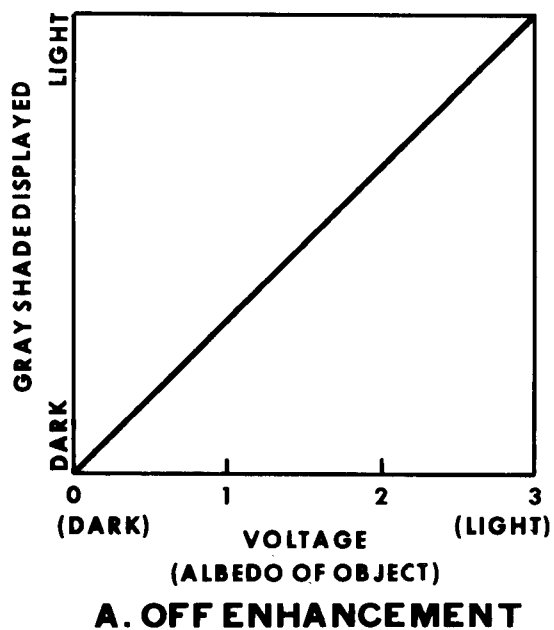
Fig 4-3.   Enhancement Modes - Graphical Representation.
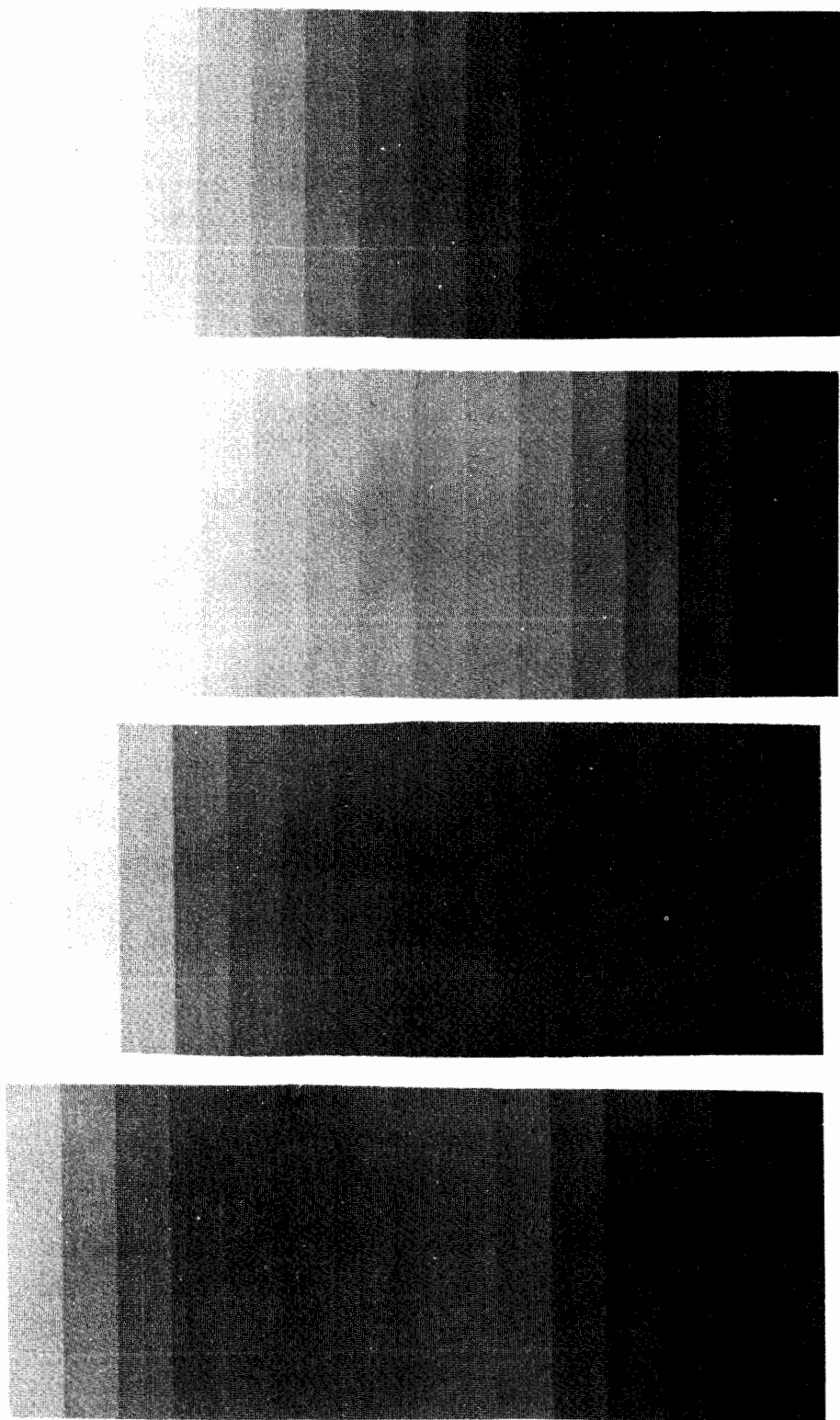
Fig 4-4.   Enhancement Modes - Pictorial Representation

produced by the spacecraft's primary sensors; however, it is not possible for a tactical readout site to receive all of them. The DMSP transmitter operates at 512 kilobits per second (kbs). This allows transmission of a multiplexed data stream consisting of HR, MI, and either VHR or WHR. The data rates of VHR and WHR are so massive that both cannot fit into a 512 kbs data stream. The normal operating mode is for VHR transmission on the ascending portion of an orbit and WHR on the descending orbit. Both HR and MI data are transmitted to all receiving sites. If the spacecraft is placed in an early morning ascending (early evening descending) orbit where there is an earth terminator problem in the visual scene, the VHR data are transmitted on the ascending portion of the orbit near the equator where there is sufficient daylight illumination for visual imagery (along scan automatic gain control for visual imagery through the terminator region exists only for the HR sensor). When the spacecraft progresses poleward far enough so that the edge of the VHR scan line enters the terminator, the transmission is switched to WHR. An example is shown of this in Chapter 3, Figure 3-7.

Analog data transmission to AFGWC has the same VHR, WHR data constraints as the tactical site; however, the multiplexing is different. HR and MI data are multiplexed together and transmitted on a 26 KHz base band-width signal. VHR or WHR data are transmitted on a 45 KHz base band-width signal.

a. Visual Data.

The two types of visual data, VHR and HR, complement each other for several meteorological applications. The VHR is designed to examine weather systems in detail such that not only is the overall synoptic pattern readily identifiable, but the details of the cloud patterns and their structure are observed. As such, VHR is the primary visual product used at the tactical sites during daylight. VHR is available to AFGWC for selected geographical areas. HR data are available to both AFGWC and the tactical sites; however, it is the primary visual data used at AFGWC. Since HR data has a lower data volume rate than VHR, it is

preferred for computer processing. The HR is used as a backup to the VHR during daytime operations at tactical sites. At nighttime the low-light capability of the HR sensor provides a useful product which greatly improves the analyst's capability to correctly interpret nighttime infrared data.

The capabilities of the DDS are illustrated by an orbit covering Mexico and the western U. S. On 19 April 1973 the DMSP data showed a wide range of both terrain features and cloud types. Products from the same orbit will be used in the next section to illustrate the MI capabilities. Examples of VHR data products using each of the four enhancement modes are shown in Figures 4-5 through 4-8. Figure 4-9 is a center expand of Figure 4-5. Coincident HR data is shown in Figure 4-10 with the same enhancement as Figure 4-5. A low light, nighttime, HR example is shown in Figure 4-11 for a different time and location.

Probably the most common way to display these data is to use the normal scale (1:15 million) with off enhancement. In this manner these data are presented with a linear distribution of gray shades over the signal range. Figure 4-5 shows this VHR product. Note that cloud texture and terrain details both are well discriminated. By selecting low enhancement (LOW ENH), imagery is produced in which low albedo objects (like most terrain features) are more easily identified. This is shown in Figure 4-6. If one compares Figures 4-5 and 4-6 he will note that the mountainous terrain appears to have sharper relief in the latter figure.

However, when low albedo objects are enhanced by the LOW ENH mode, this is done at the expense of losing some detail in high albedo objects. Compare the structure of the thunderstorm activity in the upper right portion of Figures 4-5 and 4-6; less detail is seen where LOW ENH is used than in the OFF ENH product.

A high enhancement (HIGH ENH) mode should be selected in order to more clearly see the details of high albedo objects. This is shown in Figure 4-7. Compare the thunderstorm activity in all three examples (Figures 4-5, 6, & 7). Observe that the HIGH ENH mode (Figure 4-7) best

DOCUMENT UNCLASSIFIED JCP-I,DPG

Fig 4-5.   19 Apr 1973, 5528/5536, VHR, Norm, Norm, Off

Fig 4-6. 19 Apr 1973, 5528/5536, VHR, Norm, Norm, Low

Fig 4-7.   19 Apr 1973, 5528/5536, VHR, Norm, Norm, High

brings out the detail of the high albedo cloud structure. This is accomplished, however, with a corresponding loss of detail in low albedo objects. These objects are less distinct than in either the OFF ENH or LOW ENH modes.

If one desires to see both low and high albedo objects simultaneously enhanced, a low/high enhancement (LOW/HIGH ENH) mode may be selected. This is shown in Figure 4-8 where both thunderstorm and terrain features show well. In this mode enhancement loss occurs to objects in the middle albedo range. The best way to display the details of middle range albedo objects is to use the OFF ENH mode.

The VHR can also be processed in an expanded scale (1:7.5 million) with the complete range of enhancement modes available to normal scale (1:15 million) data. When data are expanded no new information is created; it is simply an enlargement of the picture which aids in visual identification of the small scale features already existing in the normal scale picture. Expanded data can be processed directly from the spacecraft's transmission signal or replayed from the tape recorder. At AFGWC expanded data can be processed directly from the signal relayed by the tracking site, or from the ground tape recorders. Figure 4-9 is an example of expand center VHR data. Compare Figure 4-9 with Figure 4-5 and note that the lower half center portion has been expanded. This product makes an excellent briefing aid when used to describe the weather for relatively small areas. It is also possible to expand the left or right hand halves of the picture (Exp L, Exp R); however, examples are not shown for these cases.

High resolution (HR) visual data can be processed using all the modes that are available for VHR data. Normally, expanded scale is not used for HR data due to the wider spacing of its scan lines compared with VHR. (Recall from Chapter 3 that there are six VHR scans to one HR scan.) The HR daylight data may be used for the same meteorological purposes as the VHR. The only loss is in the capability of the sensor to resolve objects

smaller than two nm. The loss of resolution is illustrated in Figure 4-10, which is HR data recorded concurrently with the VHR data shown in Figure 4-5. Note the fuzziness at the edges of Figure 4-10 compared with Figure 4-5. This is caused by the degradation of the resolution from two nm at the center to twelve nm at the data edge.

HR data from the descending (nighttime) portion of the spacecraft's orbit have several uses, depending on the amount of lunar illumination. When the lunar phase is one-half moon or greater, visual images have the same clarity as images obtained in sunlight. An example of low light HR data over Northern Europe is shown in Figure 4-11. Aurora Borealis can be seen in the upper left of Figure 4-11. Auroral data are extremely valuable in mapping day-to-day variations in the ionospheric morphology. City lights are also visible in the nighttime HR data. The images of city lights have two uses. First, they serve to more accurately locate (or grid) the MI data. Second, when city lights appear diffuse, they give information about the optical thickness and particle sizes in the clouds between the light source and the sensor.

b.   Infrared Data

The two types of infrared data are MI and WHR. As described in Chapter 3, the infrared sensors are co-located with visual sensors. Common optics insure that the visual and infrared scene are viewed simultaneously and in the same perspective. This arrangement allows direct comparison of the visual and infrared data, and permits the meteorologist to envision the three dimensional aspects of the cloud scene generated by atmospheric motions.

The MI and WHR sensors were developed to serve several different purposes for the meteorological analyst. MI data, with its 2.4 nm spatial resolution at subpoint, is used as the primary infrared data for comparison with all visual data. It is also the more accurate infrared data for use in quantitative thermal determinations of cloud top or land/sea surface temperatures. MI data are transmitted to tactical sites on both ascending (day) and descending (night)

Fig 4-8. 19 Apr 1973, 5528/5536, VHR, Norm, Norm, Low/High
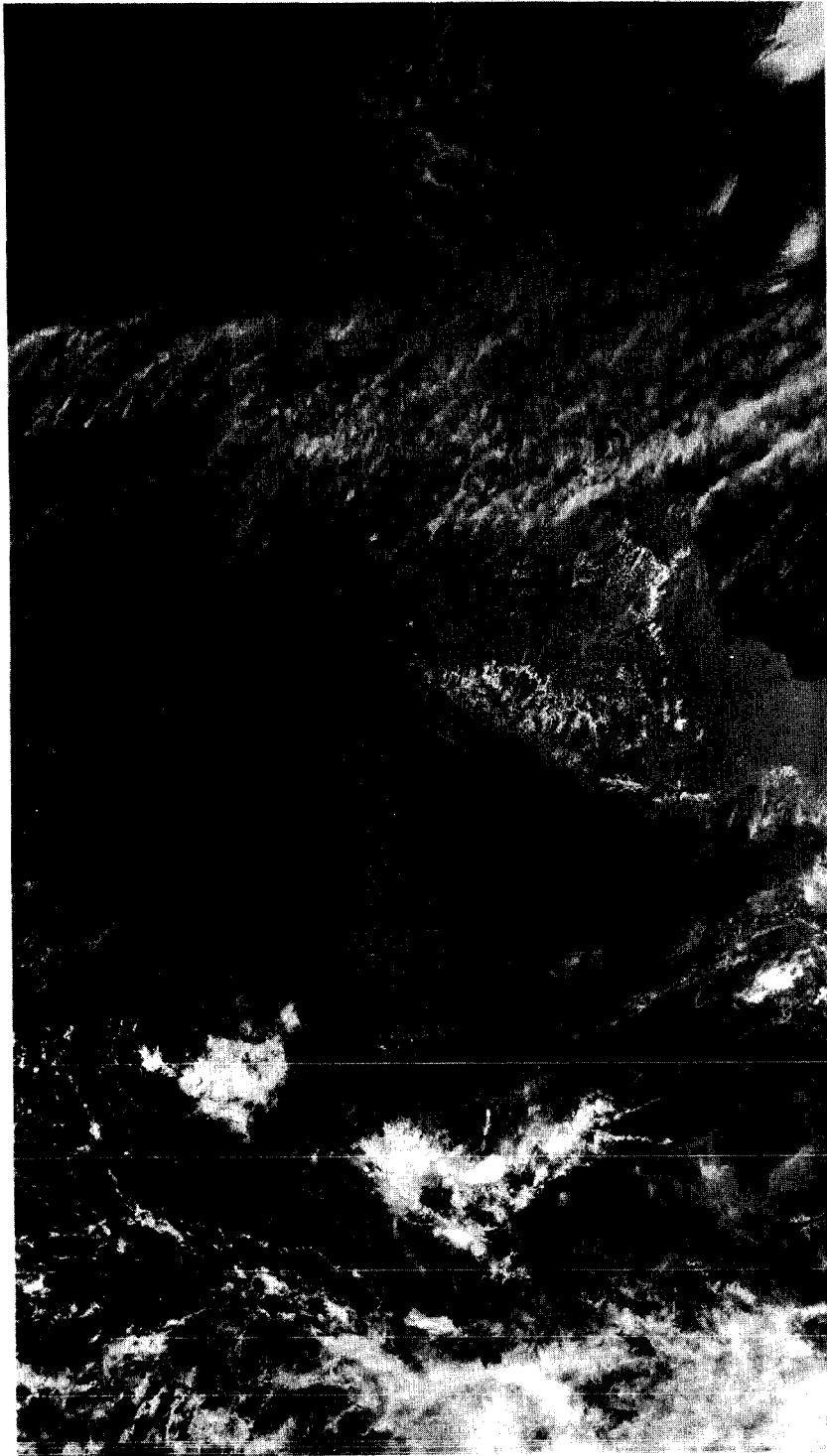
Fig 4-9.   19 Apr 1973, 5528/5536, VHR, Exp C, Norm, Off
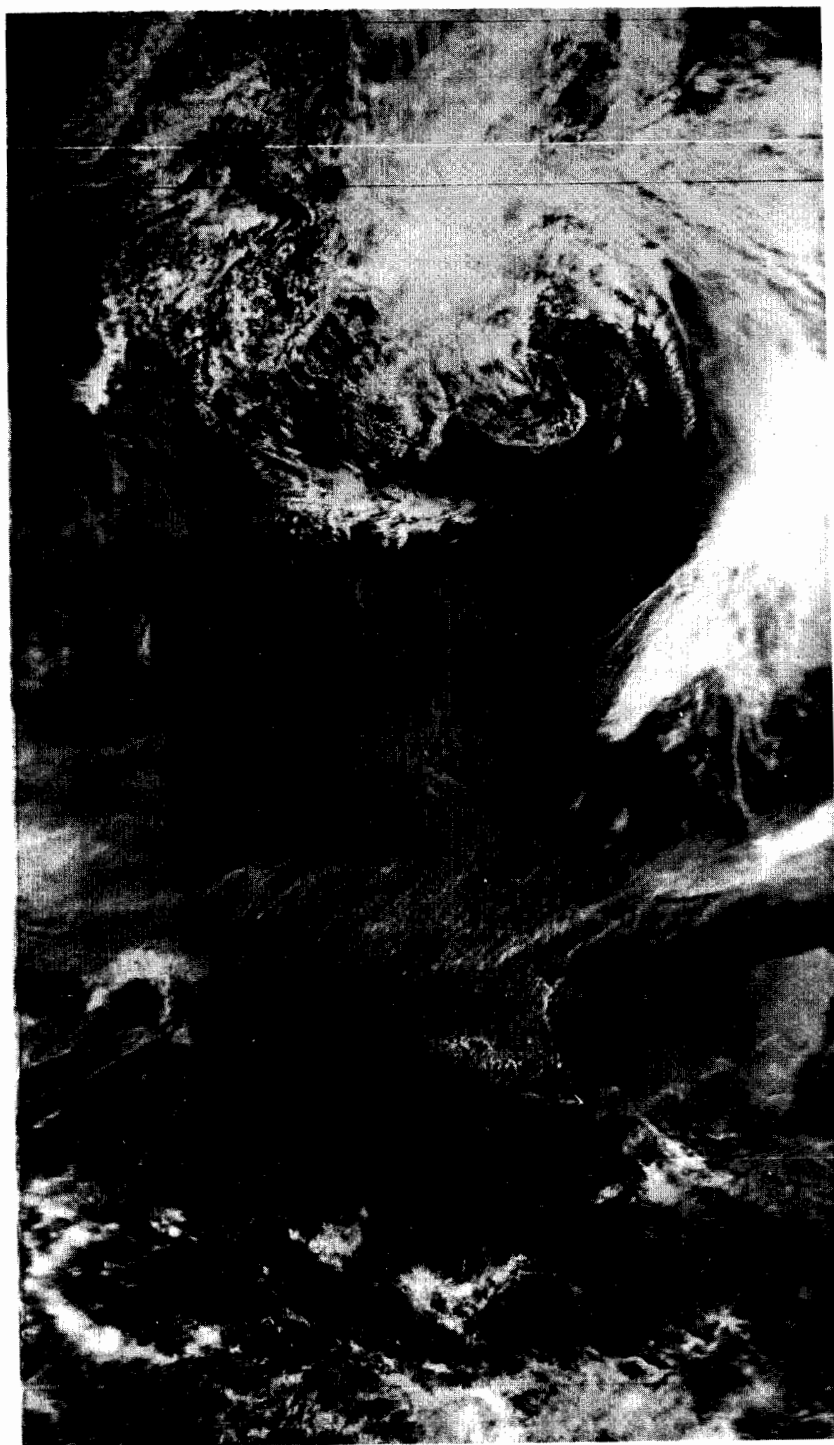
Fig 4-10.   19 Apr 1973, 5528/5536, HR, Norm, Norm, Off
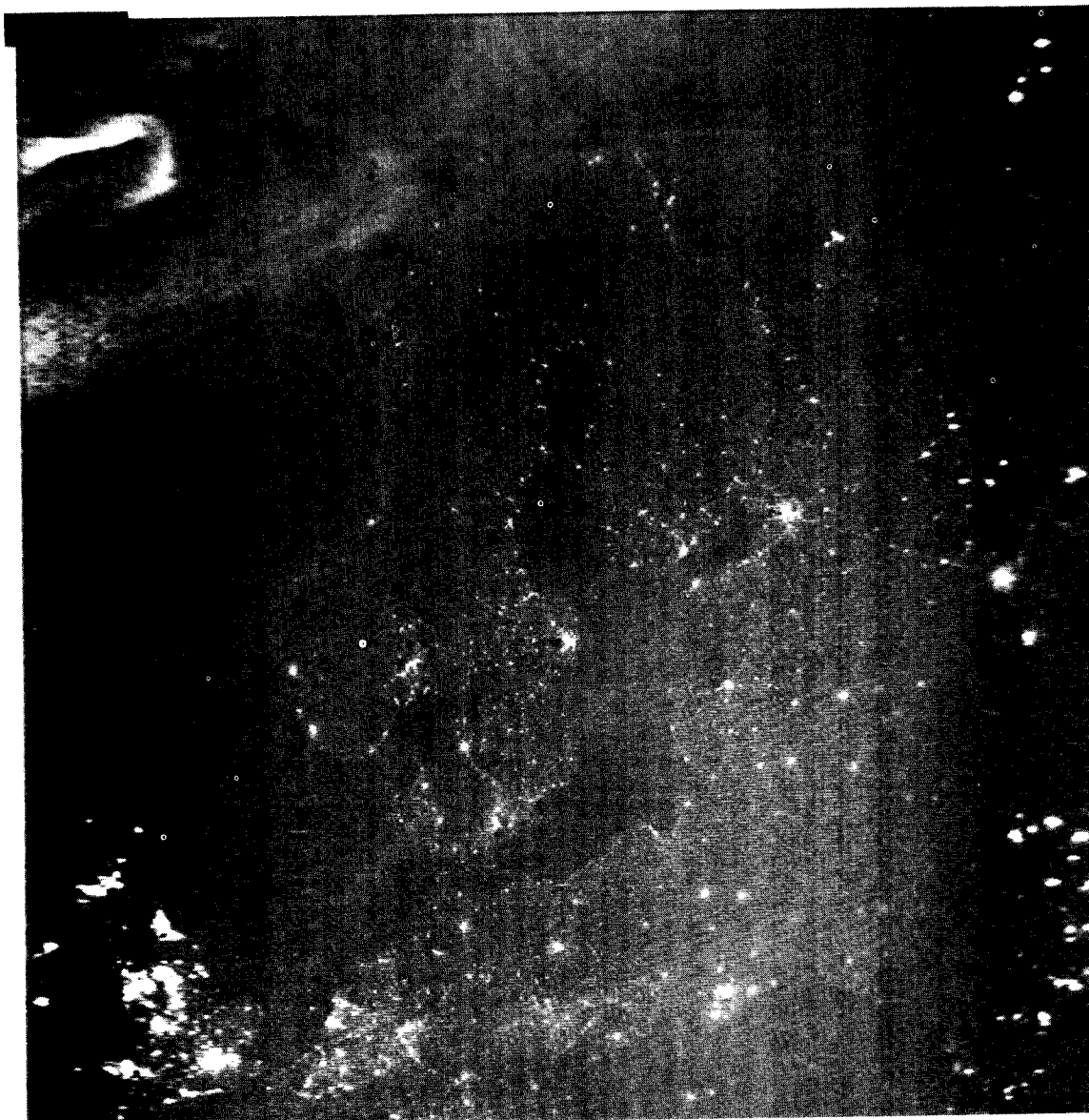
Fig 4-11. 19 Nov 1971, 4527/520, HR, Norm, Norm, Off

orbital passes. Global MI coverage is available to AFGWC from the spacecraft's tape recorders, where it is used for imagery and as input data for a computer produced "Three-Dimensional Nephanalysis" [3]. WHR data has a spatial resolution of one-third nm and is only available when VHR data are not being sensed. Thus, WHR data are the primary very high resolution imagery data available during nighttime orbital passes. It is used much as VHR is; to identify the overall synoptic pattern and observe the details of cloud patterns and structure. For AFGWC, up to 20 minutes of WHR can be stored on a spacecraft tape recorder for any selected areas in the world. The tape recorder collects WHR, VHR, or a combination of both; however, both WHR and VHR cannot be recorded at the same time. The tape recorder is limited to selected strips of WHR or VHR.

Although each type of infrared data was designed for a different purpose, both types may be processed in two modes, each of which has a multitude of variations.

Infrared data may be processed in either the Brilliance Inversion (BI) or Threshold (Thresh) modes. The first is used to show the distribution of cloud top temperatures through the atmosphere and is displayed in up to 64 shades of gray. The second is used for thermal contouring and has not more than four shades of gray. Both modes of infrared processing are normally produced with no image enhancement (the Off position) so that the linear relationship between sensed radiation and gray shades is preserved. The scale expansion to 1:7.5 million may be used with WHR data, but is usually not used with the MI since the result is similar to HR expansion. Since only one line of MI data is produced for every six lines of WHR data, MI data appears streaked when expanded. Both modes of infrared processing may be done with the polarity set to either Norm or Inv. With Inv, cold objects appear light; for Norm, cold objects appear dark. The first mode of infrared processing to be examined will be the Brilliance Inversion.

In the BI mode infrared data are normally produced so that cold objects are displayed lighter

than warm objects. While this is not done for all cases, it is a general convention followed when these data are to be used by or displayed to the non-meteorologist. Historically, visual satellite pictures were available prior to infrared pictures, and the human is used to seeing visual clouds displayed white (or at least light). As a result, most people expect to see clouds displayed in a similar manner in the infrared. This assumes that the cloud is colder than the background region. We know this is not always the case, and a well documented example is in [4], page 6-B-23. In this example warm moist air is advecting northward from the Gulf of Mexico. Fog and stratus forms over the Gulf Coast and is warmer than the surrounding cloud-free terrain. As a result, "black stratus" or "black fog" appears in the infrared. Since most cloud tops are colder than the background region, the assumption that clouds viewed in the infrared should be light is usually accurate. However, this convention is backwards to conventional engineering terminology in which the warmer the radiating object, the more energy it radiates, the more energy the infrared detector receives. Responding to that energy, the detector produces more current, thus showing warm (energetic) objects as white (large voltage). The Inv mode inverts this process so that a large voltage from the detector is displayed as black, and most clouds are lighter than the background.

The MI sensor has a 100 degree detection range from 210K - 310K. Any radiating objects colder than 210K produce a detector voltage which is forced to zero volts; thus, anything colder than 210K is sensed as if it were 210K. 310K is the warmest that can be detected, and this is an eight volt value. The detector output is linear from zero to eight volts (210K - 310K). The thermal accuracy is better than 1°C for the entire 210K - 310K range. The first WHR sensor was slightly different, having a detection range of 217K - 307K and one to three degrees thermal accuracy. Newer WHR sensors have a detection range of 210K - 310K.

The DDS allows us to display the emissions sensed by the infrared detectors in numerous ways. To do this in the BI mode, the

warmest temperature to be displayed
is selected and dialed into the DDS.
This is called the "Base" tempera-
ture. Also selected and dialed into
the DDS is the thermal range over
which the data are to be displayed.
This range is called the "Expand."
The Base temperature may be any whole
degree from 320K to 210K. The
thermal range is selectable to one of
three settings. Expand one (usually
written X1) will cause 64 shades of
gray to be spread over a 100 degree
interval downward from the Base
temperature. Expand two (X2) will
spread the 32 shades of gray over a
50 degree interval. Expand four (X4)
is a 25 degree, 16 shade interval.
In each case a constant thermal inter-
val of 1.5625°K per gray shade is
maintained. The advantage of the X2
and X4 modes lies in making the
thermal detail more discernable to
the human eye. (Normally, the human
eye can "see" up to 14 shades of
gray.) To maintain this exact temper-
ature interval, the enhancement mode
Off is always used. If Hi, Lo, or
Lo/Hi were used, then the linear dis-
tribution of temperature vs gray
shade would be destroyed.

        Both MI and WHR infrared
data can be displayed by the DDS in
the same fashion; however, since MI
data has better thermal accuracy than
WHR data, it is normally the data
used for quantitative work on cloud
top temperatures and equivalent
altitudes. For that reason most of
the infrared pictures shown in this
Technical Report will be MI. The
terminology used will be like this
example: MI INV 310 X1. This BI
product consists of MI data inverted
so that cold objects appear light,
and the 100 degree temperature
interval extends from 210K - 310K.
This is a typical setting for MI
pictures. No image enhancement is
used so that the 64 gray shades are
linearly distributed over the 100
degree range producing a thermal
interval of 1.5625 degrees per shade
of gray. Figure 4-12 is such an
example and it is coincident data
with the VHR examples shown earlier.
Compare it with Figure 4-5. The
complementarity of coincident visual
and infrared imagery is depicted well
by these two examples. The cirrus
associated with a subtropical jet-
stream crossing Mexico stands out in
the infrared. The clouds associated

with a frontal system near the Texas
Gulf coast appear well developed and
extend southward along the Mexican
East Cost in the VHR data. The MI
data shows that almost all of the
southern extension is comprised of
low lying clouds, quite inactive
when compared with those further north.
The low lying stratocumulus west of
Mexico are nearly invisible in the
infrared. Cumulonimbus clouds, with
their cold tops, literally bloom in
the infrared.

        If greater discernability
is needed than exists in Figure 4-12,
then a different Expand mode can be
selected. For example, if the interest
were in clouds extending above the
freezing level, then an MI INV 273 X2
could be chosen to give 32 shades of
gray for the temperature interval
from 223K - 273K. In Figure 4-13 we
show a slightly different example,
an MI INV 260 X2. Note that all
radiating surfaces warmer than 260K
are displayed as black. The thermal
detail of the layered clouds associ-
ated with the storm over the southern
U S is considerably enhanced. Some
people prefer not to Inv this type
of picture, and display it in Norm.
Most people's eyes can discern dif-
ferences between dark gray shades
better than between light gray shades.
Dark clouds can be discriminated
better this way; however, it does
take a while to get used to working
with dark clouds when one is accus-
tomed to light ones.

        If still more detail in
the cold cloud tops is desired, then
an MI INV 235 X4 can be made, which
distributes the 16 shades of gray
over a 25 degree interval. Figure
4-14 shows this. As expected, good
detail appears in the cold clouds,
with all else warmer than 235K appear-
ing black.

        Sometimes detail is want-
ed for warm radiating objects. These
might include the ground, warm ocean
currents (Gulf Stream), low level
clouds, and warm water formation areas
for tropical cyclones. Figure 4-15
is an MI INV 310 X4. Note the thermal
mapping of Mexico. Several small
variations in water temperature are
visible off the southwest Mexican
Coast. Care must be taken, however,
to compare this type of product with
VHR data to ensure that small cumulus

Fig 4-12.   19 Apr 1973, 5528/5536, MI, Norm, Inv 310 X1, Off

Fig 4-13. 19 Apr 1973, 5528/5536, MI, Norm, Inv 260 X2, Off

Fig 4-14. 19 Apr 1973, 5528/5536, MI, Norm, Inv 235 X4, Off

DOCUMENT UNCLASSIFIED JCP-I,DPG
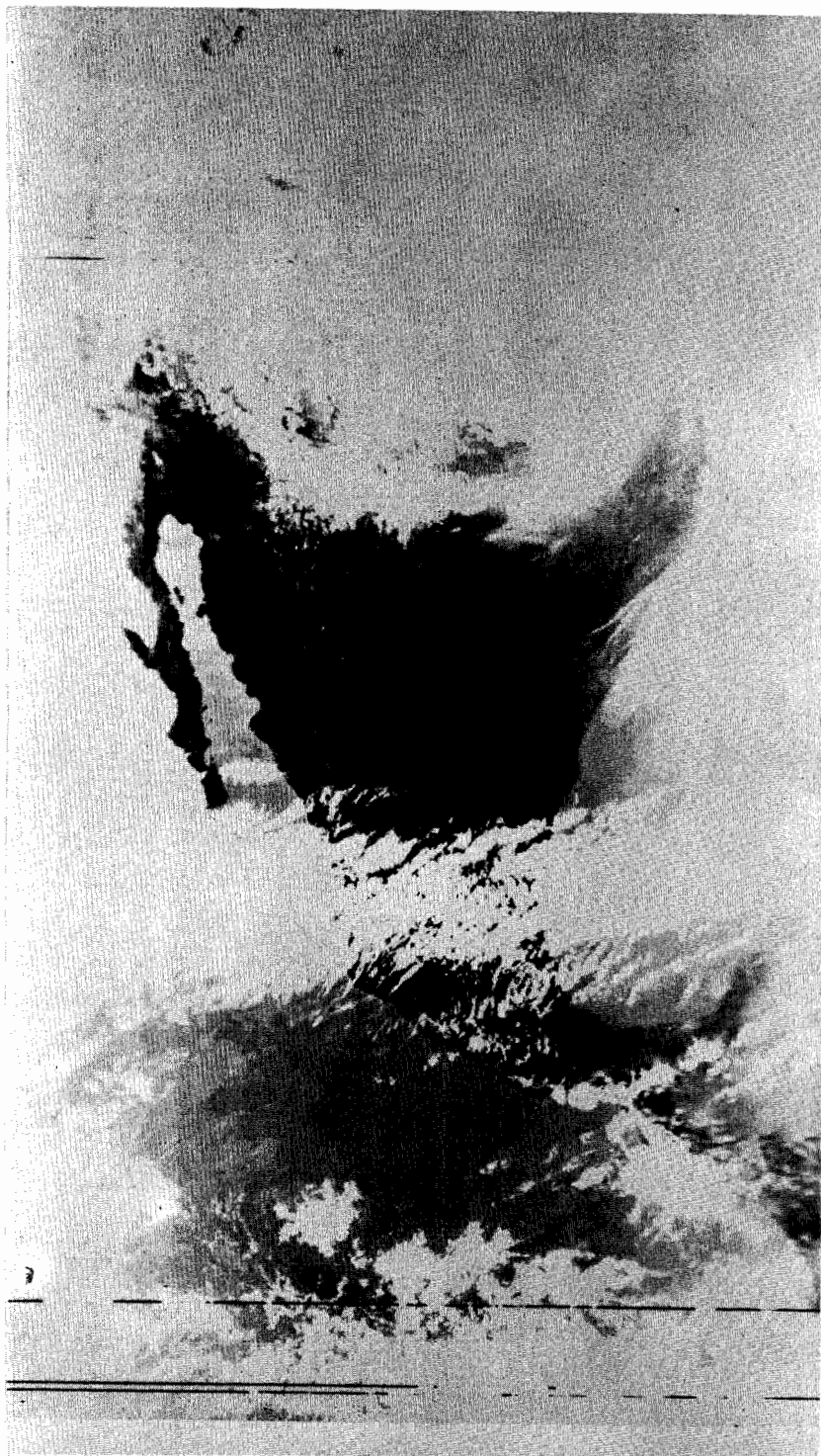
Fig 4-15.   19 Apr 1973, 5528/5536, MI, Norm, Inv 310 X4, Off

cloud elements or very thin higher clouds are not causing false temperature gradients in what appears to be clear air on the MI product. The ability of the 1/3 nm VHR visible data to see most of the smaller cloud elements will help avoid this problem. The MI 2.4 nm resolution sensor simply cannot discriminate the smaller clouds. The thermal emissions of these small clouds will be averaged with the background emission, causing a "false" temperature indication.

By using the X4 expansion it is possible to divide the atmospheric and surface emissions from 210K to 310K into 64 discernable shades of gray. This can be done by making four BI products with the Base temperature settings at 310K, 285K, 260K, and 235K.

In an MI INV 310 X1, the first level on the gray scale (black on Figure 4-4 Off Enhancement) represents all emissions from objects between 303.75K and 310K. If a smaller temperature interval is desired at the dark (warm) end of the gray scale, a Base temperature warmer than 310K can be set into the DDS. For example, if MI INV 320 X1 is set, the darkest shade of the gray scale will extend from 320K to 308.4375K (in reality 310K to 308.4375K), the lightest shade (white) would be missing, and the second lightest shade would extend from 220K to 220.9375K. The portion of emissions below 220K would be lost.

If a Base temperature is set colder than 310K, shades of gray may also be lost. For example, if MI INV 285 X1 is set, then only 48 gray shades are displayed. The 16 darkest shades (>285K) would be lost and the lightest shade (white) would include all emissions between 211.5625K and 185K (in reality 211.5625K and 210K).

Considerable flexibility has been built into the BI mode of operation; however, there are times when the meteorologist desires to know what cloud tops extend above a critical altitude (below a fixed temperature), or lie within an altitude zone (between temperatures). There may be times when one degree differences are important. To pro-

duce imagery displays which can show the above, the thresholding mode of operation may be selected.

The Threshold (or Thresh) mode of the DDS produces imagery which contains not more than four shades of gray. The number of gray shades and the threshold or contour intervals are determined by selecting temperature values called Y values. The Y value temperatures can only be set so that the first Y value, Y1, is greater than or equal to the second, Y2, which is greater than or equal to the third, Y3. Thresh imagery may be produced in either an invert (Inv) mode or normal (Norm). A Thresh Inv with three different Y1, Y2, Y3 settings will have all emissions warmer than Y1 displayed black; those emissions between Y1 and Y2 will be dark gray; those emissions between Y2 and Y3 will be light gray; and everything colder than Y3 will be white. A Thresh Inv example with Y1 = 285K, Y2 = 275K, and Y3 - 266K is shown in Figure 4-16. This is the same orbit of data that most of the visual and infrared examples used earlier in this chapter have been taken from. As can be seen in Figure 4-16, the Thresh Inv mode displays the infrared data in the same sense that an MI Inv does; cold emissions are light shades of gray, and warm emissions are dark shades of gray.

Figure 4-17 is an example where Thresh Norm is used with Y1 = 258K, Y2 = 246K, and Y3 = 234K. In this case the black clouds are those colder than 234K. The Y-values selected for Figures 4-16 and 4-17 were derived from radiosonde observations along the U S - Mexican border. Those observations showed that 285K, 275K, and 266K corresponded to altitudes of 10, 15, and 20 thousand feet. Similarly, 258K, 246K, and 234K corresponded to altitudes of 25, 30, and 35 thousand feet. If there were no horizontal temperature gradients in the atmosphere, then Figure 4-16 and 4-17 would depict the entire area for seven altitude intervals; 0-10, 10-15, 15-20, 20-25, 25-30, 30-35, and greater than 35 thousand feet. In reality there are horizontal temperature gradients, so the two figures only approximate those altitude intervals over the entire imagery area. What is really shown are seven emissive intervals.

DOCUMENT UNCLASSIFIED JCP-I,DPG

Fig 4-16.   19 Apr 1973, 5528/5526, MI, Norm, Thresh, Inv, 285-275-266

DOCUMENT UNCLASSIFIED JCP-I,DPG

Fig 4-17.   19 Apr 1973, 5528/5536, MI, Norm, Thresh Norm, 258-246-234

An effective display method sometimes used is to make an ozalid copy of VHR visual data to use as an opaque background for MI Thresh colored transparencies. For the examples used in this Technical Report, make an ozalid copy of Figure 4-5, make a red diazo copy of Figure 4-16, and make a blue diazo copy of Figure 4-17. Overlay the three copies and the following is achieved: Warm terrain and cloud tops less than 10 thousand feet show dark red, 10-15 thousand feet cloud tops are red, 15-20 thousand feet cloud tops are pink, 20-25 thousand feet are white (the VHR clouds showing through transparent diazo), 25-30 thousand feet are light blue, 30-35 thousand feet are blue, above 35 thousand feet are dark blue. The colored sequence of dark red for warmest to dark blue for coldest presents an excellent three-dimensional depiction of cloud layers to the viewer. An example cannot be shown in this Technical Report. One is available in [5] and described in [6].

Figures 4-16 and 4-17 are examples of three different Y values. If only two levels of contouring are desired, then two of the Y values may be set equal. In this manner only three shades of gray will be produced. The middle shade of gray will be either light or dark depending on three possible settings: $Y1 = Y2$, $Y2 = Y3$, and the Norm/Inv selection. Figure 4-18 has $Y1 = Y2 = 275K$, $Y3 = 258K$, and Inv polarity. Therefore black indicates warmer than 275K (below 15 thousand feet), light gray between 258K - 275K (between 15-25 thousand feet), and white is colder

than 258K (above 25 thousand feet).

If contouring of one level is desired then all three Y values are set equal. The imagery is white and black with no shades of gray. If white is to indicate "colder than," the polarity should be set to Inv. Figure 4-19 is an example with $Y1 = Y2 = Y3 = 273K$. These settings result in a demarcation between those clouds/surface features which are above or below the freezing level.

The Thresh mode may be used with the temperature settings equally spaced, equal, staggered for large intervals, or staggered for narrow temperature intervals. The range of Y numbers that can be set into the DDS is 198K - 319K; however, only 210K - 310K will produce meaningful data. The calibration range for the DDS Y numbers is 210K - 310K. If desired, the Thresh mode can be used to contour selected emissive layers only one degree apart. One could, with multiple reruns of these data, produce imagery showing the earth and clouds in one degree intervals from 210K - 310K.

All the BI and Thresh examples shown in this chapter used data from the MI sensor. All the BI and Thresh techniques can be applied to WHR data equally as well as for MI data. The only reason no WHR data were used here for examples is that VHR data were used to illustrate the enhancement and expand mode of visual operations. When VHR data are produced by the spacecraft, WHR data cannot be obtained.

Fig 4-18. 19 Apr 1973, 5528/5536, MI, Norm, Thresh Inv, 275-275-258

DOCUMENT UNCLASSIFIED JCP-I,DPG

Fig 4-19. 19 Apr 1973, 5528/5536, MI, Norm, Thresh Inv, 273-273-273

DOCUMENT UNCLASSIFIED JCP-I,DPG

Chapter 5 - Data Accuracy

A. General

The DMSP sensors and DDS were designed to provide high quality meteorological data and have it in the hands of the forecaster within five minutes after data transmission terminates. The system approach was taken to ensure that the resolution inherent in the basic sensor electronic signal would be faithfully preserved through amplification, recording, transmission, and eventual display on the ground. Following deployment of both the ground equipment and the spacecraft, an evaluation was performed to see if, indeed, the imagery available to the forecaster met the engineering specifications. The results of those evaluations plus operational experience provide the basis for the sections to follow.

B. Resolution

The spatial resolution of each sensor was discussed in Chapter 3. The sensors were engineered to provide subpoint spatial resolution of 1/3 NM for VHR and WHR data, 2 NM for HR data, and 2.4 NM for MI data. However, the resolution which is apparent in the film available to the forecaster is a function of:

a. Sensor lens/mirror aberrations.

b. Detector (bolometer) characteristics.

c. Frequency response of sensor electronics.

d. Smear due to image motion.

e. Tape recorder characteristics (if not direct readout).

f. Communications.

g. Ground station's characteristics/maintenance.

h. Height of satellite.

i. Relative contrast between object and the background.

j. Alignment of object to the scan line.

k. Others.

All these data are rectified by the Signal Processor No 1 and Basic Display portions of the DDS, but the rectification process does not improve spatial resolution.

The spatial resolution and thermal accuracy of the DMSP system were evaluated by means of two projects, Cold Flight I and Cold Flight II. These evaluations showed that the sensor design resolution and achieved film imagery resolution were nearly equal. In Cold Flight I, geographical features apparent in VHR imagery were examined and compared with their known sizes indicated on aeronautical charts. Selected features as small as one-half NM were visible. Smaller geographical features were not available for analysis. HR data were examined, but not in as great a detail as VHR data. For HR it was found that two NM features were visible in the data at subpoint. Due to foreshortening the 2 NM resolution degraded to approximately 12-14 NM at data edge. The variability was due to changing spacecraft altitudes, and the rectification of the imagery by the DDS to a constant scale, equal area projection, 450 NM nominal altitude. The spatial resolution does not degrade to less than 12-14 NM at data edge because the full scanning radiometer line sweep is truncated before the line reaches the "edge of the earth." Generally, for 1:15 million scale HR data, the spatial resolution averages 8-10 NM in the extreme right- and left-hand inch of data.

Nighttime HR data spatial resolution is much more dependent on light level and contrast than daytime HR data. It was not examined in great detail; however, Cold Flight I plus operational experience has shown that nighttime HR imagery has the same spatial resolution as daytime data for high contrast targets during a five night period centered on full-moon. Slow degradation of resolution

progresses to the half-moon illumina-
tion point, thereafter rapidly dete-
riorating to the quarter-moon point
where objects lighted by moonlight
are, for the most part, nonresolvable.
The spatial resolution for light
emitting objects (e.g., cities) re-
mains the nominal resolution for any
phase of moonlight.

Cold Flight II was a much more
exhaustive effort to determine
resolution. High altitude aircraft
photographed clouds in the vicinity
of the Hawaiian Islands. The
dimensions of low clouds and land
features from known altitudes were
compared with VHR imagery from
satellite passes within 15 minutes of
the aircraft photographs. The re-
sults are shown in Table 5-1.

Object Size (NM)	Percent of cases visible in VHR	Cases
0.2	39%	23
0.3	40%	20
0.4	55%	18
0.5	71%	24
0.6	92%	12
0.7	93%	14

Table 5-1. Percentage of objects
visible in VHR data from different
size groups.

It is interesting to note that a
significant percentage of objects
only 0.2 NM in size were detected by
the VHR system; however, not all
objects as large as 0.7 NM were
detected. There are at least two
important factors bearing on these
results:

1. The land and cloud feature
cases selected from the aircraft
photographs were not restricted to
the satellite subpoint region. The
cases were distributed throughout
the area viewed by the satellite;
therefore, foreshortening effects
would limit the number of small
objects detectable by the VHR sensor.

2. The spectral range of the
photographic film was different from
the VHR sensor's. The photographic
film was a conventional Kodak black
and white emulsion which responds
primarily to visual wavelengths.
Very little blue and near-infrared
response was present. Since the VHR

sensor responds to considerable
quantities of reflected near-infrared
radiation, the VHR sensor pictures and
aircraft photographs are not directly
comparable. This is the probable
reason why several bright clouds,
clearly visible in the aircraft photo-
graphs, were unexpectedly missing in
VHR imagery.

As a general rule of thumb, VHR
imagery displayed in a 1:15 million
scale has a spatial resolution of one-
third to one-half nm within the first
inch of data either side of subpoint.
From one inch to two and one-half
inches either side of the subpoint the
spatial resolution degrades from one-
half to one nm. From the two and one-
half inch point to data edge the
spatial resolution further degrades to
two nm. These degradations are due to
foreshortening.

Spatial resolution is more dif-
ficult to quantitatively determine for
infrared sensors than it is for visual
sensors. In the infrared the spatial
resolving power of the sensor can be
masked by the thermal accuracy of the
sensing system. A target within view
of an infrared sensor may have sufficient
size to be detected by the sensor; how-
ever, if that target does not thermally
contrast with the background by at least
one shade of gray thermal difference,
the target is not identifiable. Opera-
tional experience has shown that if an
infrared target is at least 8°C differ-
ent from its background, then the
spatial resolution for MI data is 2.4 nm
at subpoint degrading to 14-17 nm at
data edge. WHR data has the same
spatial resolution as VHR data; 1/3 nm
at subpoint degrading to 2 nm at the
data edge. For a nominal orbit the
data edge is 803 nm away from the
subpoint.

C. Thermal Accuracy

The thermal accuracy of the MI
sensor is better than 1°C for the
temperature range from 210K-310K.
Current WHR sensors have the same range,
but the accuracy degrades from 1°C at
310K to 3°C at 210K. These are engi-
neering values for the sensors derived
from tests in a thermal vacuum chamber.
The determination of absolute emission
temperatures of the surface and clouds
is further degraded due to contamination
by atmospheric ozone, carbon dioxide,
and water vapor. All of these major

contaminants (there are some minor ones also) tend to decrease the emission received by the sensor when compared to the original target emission.

the atmosphere is difficult to measure, particularly on a synoptic basis. Their quasi-constant effect is treated as an add-on to water vapor absorption. The largest effect on the abso-
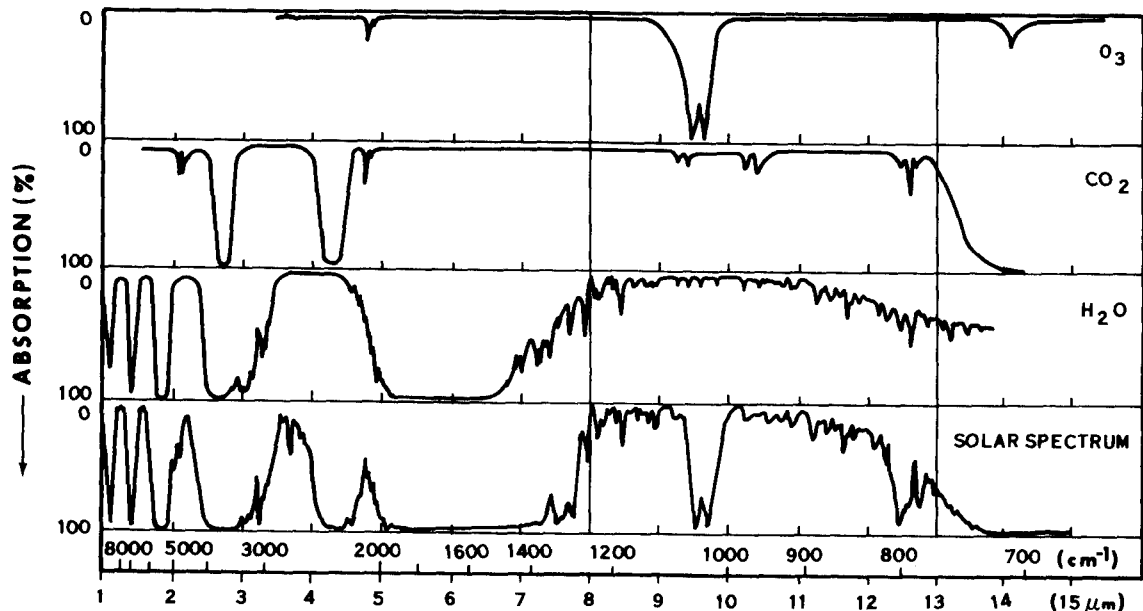
Fig 5-1.   Comparison of near-infrared solar spectrum with laboratory spectra of various atmospheric gases.   [7]

Figure 5-1 shows the absorption spectra for ozone, carbon dioxide, water vapor, and the solar spectrum. The interval from 8-13 µm is outlined to indicate the spectral range for the MI and WHR sensors. Nowhere within this interval is the atmosphere totally transparent to infrared radiation. Carbon dioxide is considered to be a well mixed component of the atmosphere, and its absorption between 8-13 µm is small. Ozone, except for the peak near 9.6 µm, has relatively small absorption. Even though ozone is known to undergo variations in concentration within the troposphere, it is usually treated as a constant. The distribution of both ozone and carbon dioxide concentrations within

lute thermal accuracy of infrared sensors comes from water vapor absorption. The quantity of water vapor varies horizontally, vertically, and with time. It has the least amount of absorption between 9.5 µm and 10.5 µm, and progressively increases in other intervals within the sensor range. The solar spectrum curve shows the total effect of all major and minor absorbers within the sensor range. It is clear that the atmospheric window is not clean. Even without the ozone absorption spike the atmospheric window is considerably smudged at the edges by other absorbers, primarily water vapor. The net attenuation effect must be considered when seeking absolute temperature values from infrared sensors.

Preliminary examinations from Cold Flight I showed that the MI sensor detected the sea surface temperature in cloudless and relatively dry areas of subtropical highs 1-2°C too cold (e.g., actual sea surface temperature shown by ship synoptic data would be 1-2°C warmer than MI data showed). For colder water off the Norwegian coast near 70N the sea surface temperature was sensed 3°C too cold.

Cold Flight II and later "Data Application Reports" from the Hawaiian tactical site examined the attenuation problem in considerably greater detail. It was shown that a moist tropical oceanic atmosphere has a considerably larger effect on the absolute thermal accuracy of the MI sensor. Sixty cirrus-free MI sensor readings of sea surface temperature were taken and compared with ship synoptic reports. Linear multiple correlation coefficients were calculated for three classes of data. See Table 5-2.

Distance from Nadir in Inches on Picture	Sea Surface Temperature Minus MI Sensed Temperature (°C)
0-1	7
1-2	9
>2	12

Table 5-2. Difference between sea surface temperature and MI sensed temperature for three regions on MI picture.

The intervals on the MI picture, 0-1, 1-2, and >2 inches, correspond to sensor scan angles (β) measured from nadir (Figure 5-2) of, 0°-15.2°, 15.2°-31.1°, and >31.1°. It was also found that as the sensor aged in space, further degradation occurred. Over a year's time the values indicated in Table 5-2 would increase 1-2°C.

The radiating temperature of low cloud tops was investigated in detail on 25 March 1970 during Cold Flight II. Aircraft were flown to within 1000 feet horizontally of cloud tops. If the cloud was near a Hawaiian radiosonde observation both in time and space, then that sounding was used to determine the atmospheric temperature and moisture structure. If no radiosonde stations met the criteria, then a dropsonde was released to provide timely information for that cloud or group of clouds if closely spaced. The cloud or cloud family had to be at least two nm in size and observed within 15 minutes of a satellite pass. The meteorological observers on the aircraft recorded the aircraft altitude (cloud top altitude) and Rosemont probe temperature of the air for that altitude. All clouds observed that day had their tops between 8,000 ft and 10,200 ft, were within 20 degrees of the satellite nadir; and their tops registered 2°C to 6°C on the Rosemont probe. Generally, the cloud top temperatures were detected too cold by the MI sensor, thus overestimating the cloud top altitude by 3000 - 5000 feet.

On 17 March 1970 a thick cirrus shield near Midway Is was investigated. Its top was measured at 30,000 feet by the aircraft with a Rosemont probe temperature of -43°C. MI thresholding was used and indicated a temperature between -48°C and -51°C. The observation occurred with a sensor scan angle of $\beta=45°$. The result was that the cirrus cloud top temperature, when compared to the aircraft recorded and Midway Is radiosonde temperatures, indicated the cloud was detected 4000 feet too high by the sensor.

A linear regression equation was constructed from Cold Flight II data. It is:

$$Ta - 13.16 + 0.482ERT \qquad \text{(Eq 5-1)}$$
$$+ 0.013\beta + 0.1167\overline{\overline{W}}$$

where: Ta = actual temperature

ERT = effective radiating temperature determined from MI data.

β = sensor scan angle.

$\overline{\overline{W}}$ = mean mixing ratio determined in 100 mb layers from 200 mb to the radiating surface, and then each layer summed.

Figure 5-3 shows a plot of effective radiating temperature vs actual temperature for the idealized transparent

β = SCAN ANGLE

Z = ZENITH ANGLE

Y = INCREASED ATMOSPHERIC DEPTH

X = ATMOSPHERIC DEPTH
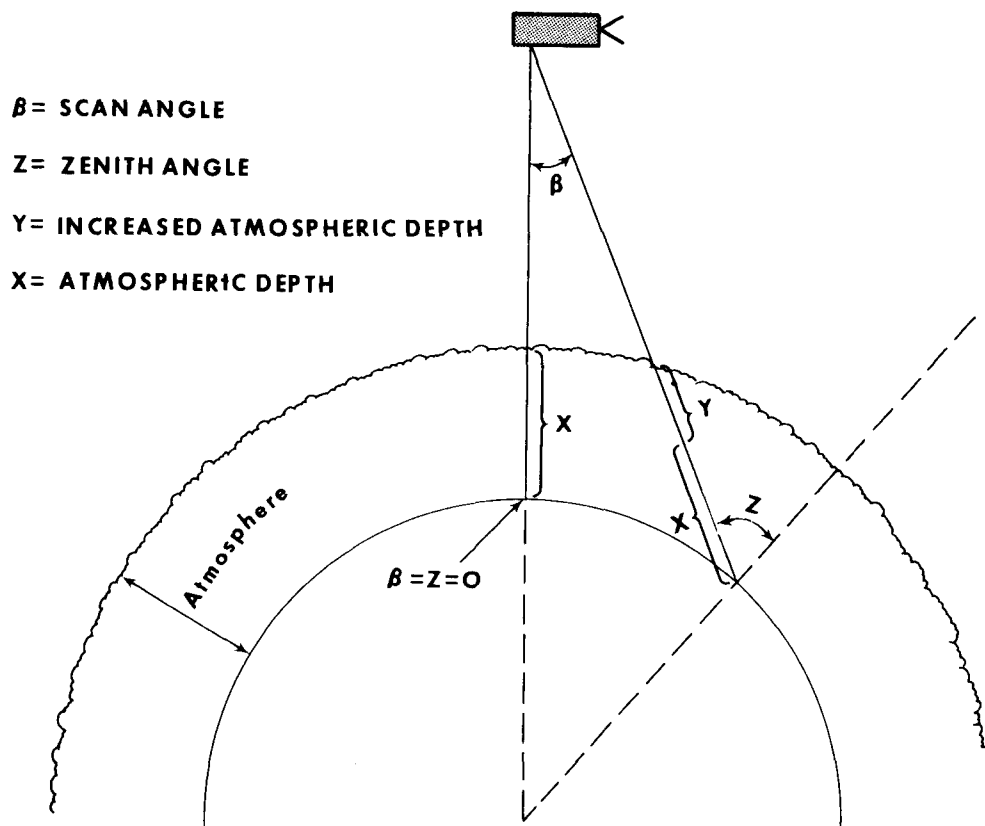
Fig 5-2.   Attenuation geometry.

atmosphere, and examples of an Hawaiian tropical moist atmosphere observed through three ranges of sensor scan angle.

The error between actual temperature and effective radiating temperature was observed to be related to the moisture distribution. The regression equation describing it is:

(Eq 5-2)

Error $(T_a - ERT) = -35.97$ (Eq 5-2)
           $+ 30.98 \ Log(\bar{\bar{w}}/Cos \ \beta)$

where: $\bar{\bar{w}}/Cos \ \beta$ represents a line of sight measurement through the moisture layers. Eq 5-2 is plotted in Figure 5-4.

The Hawaiian site performed another study on absolute thermal accuracy using 25 Sep 1970 MI data. Radiosonde data was used from within six hours of a satellite pass. A correlation was derived between radiosonde "observed" cloud top temperatures and the effective radiating temperature indicated by MI data. It was assumed that the atmospheric thermal structure did not

ERT (DEGREES C)

T_a (DEGREES C)
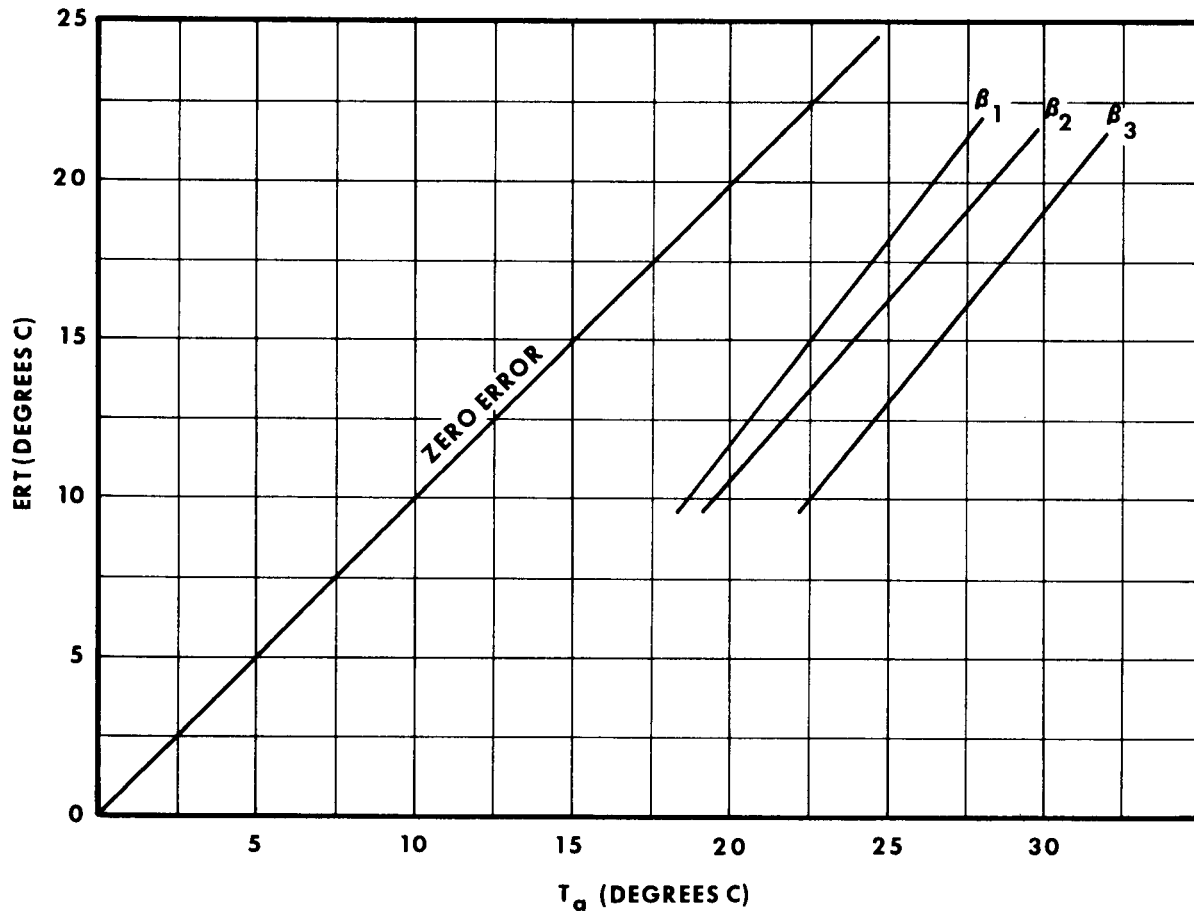
β_1 = ANGLES 0° -15.2°

β_2 = ANGLES 15.2° - 31.1°

β_3 = ANGLES > 31.1°

Fig 5-3. Effective radiating temperature vs actual temperature

change in the time period between radiosonde observation and the satellite passes. Further, it was assumed that the radiosonde observation was representative for the area covered by layered frontal clouds, and that the weather system was in steady state. These assumptions cannot be totally accurate because there was convective heating during the day and the frontal system was undergoing frontolysis. Low and middle altitude cloud top temperatures were determined by using techniques described in AWS Manual 105-24 [8]. Cirrus cloud tops were calculated to be near the 200 mb level where, if a parcel had been lifted moist adiabatically, it would have intersected the temperature sounding. This level also closely approximated the level of maximum winds, a reasonably good indicator of cirrus.
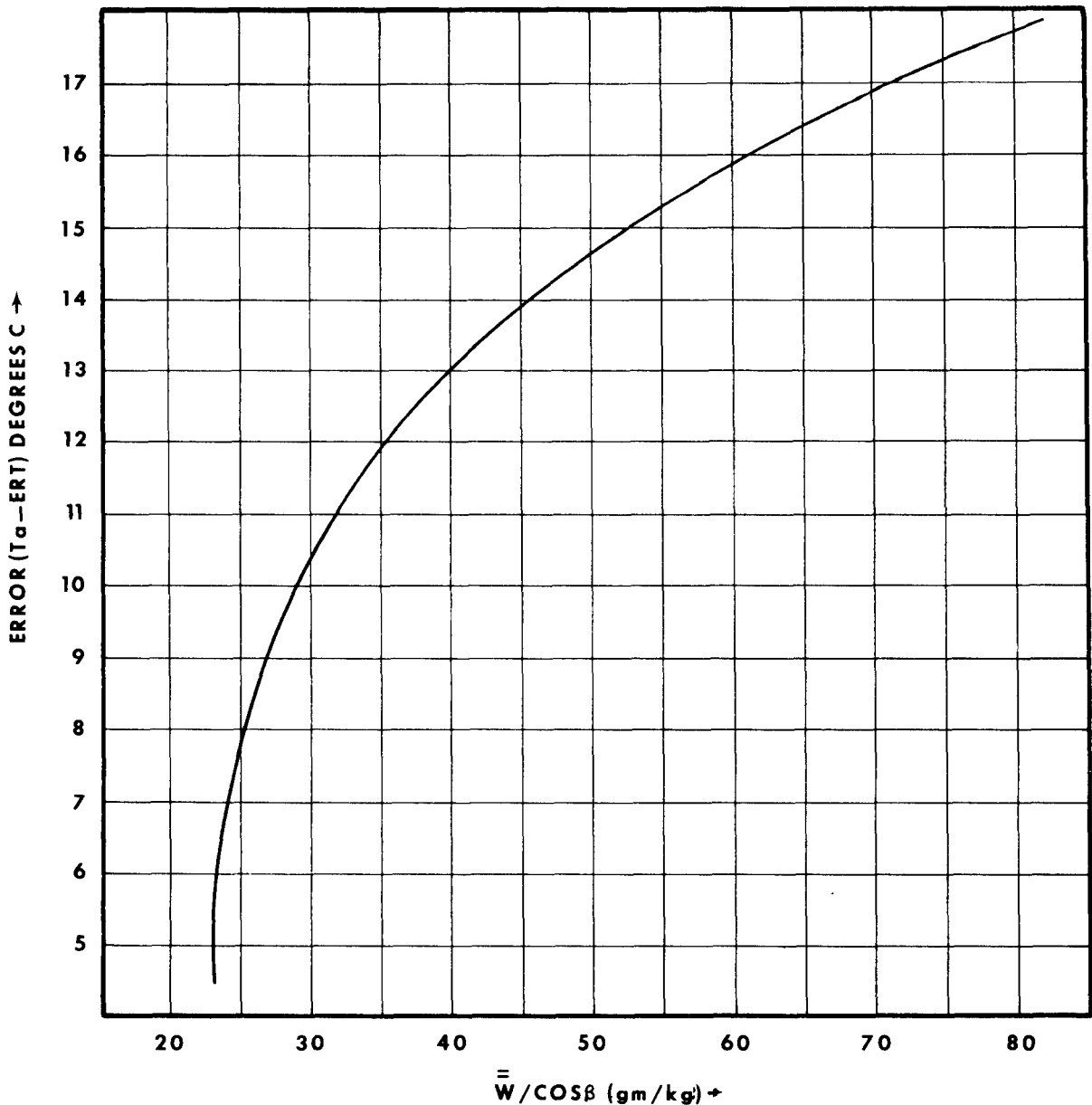
Fig 5-4.   Temperature error vs moisture.

Effective radiating temperatures were determined by matching various combinations of Brilliance Inversion and Threshold MI products. Through careful examination, the cloud top ERT interval can be narrowed to about 2°C. The results of the study were considerably different from Cold Flight II. For this mid-latitude situation it was found that satellite observed ERT's were warmer than the cloud top temperatures observed by radiosonde. The reason for the difference from Cold Flight II results was felt to lie in the assumptions used for determining "observed" cloud top temperatures, and the difficulties encountered in selecting suitably opaque clouds. The MI sensor indicated cloud top ERT's warmer than the cloud top, but colder

than the underlying surface. This indicates that warmer emissions from within the cloud were penetrating through the cloud top, thus giving a false reading. It also indicates that clouds should not be assumed to radiate as perfect black bodies.

The first WHR sensor was not flown until November 1972. An evaluation was performed on its response characteristics using AFGWC data, (9). The result is shown in Figure 5-5. In general, the evaluation showed that cold objects were being detected 20 °C too cold, and that warm objects were being detected 15°C too cold. Coincident MI data was much more accurate, showing the emitted temperature to be 5°C colder than the observed temperature over a range from 230K to 300K. As the WHR sensor ages in space and contamination collects on the radiative cooler, its thermal response degrades further. For these reasons WHR data are used for imagery rather than quantitative temperature determination. The MI sensor is much better suited to determine accurate emissive temperatures.

D. Theoretical Attenuation Corrections

It is apparent that atmospheric attenuation factors are different for each site depending on its location and season. Many sites have a continuing evaluation program so that accurate temperatures (cloud heights) can be obtained for mission support. To assist those who do not have access to site peculiar calibration data, theoretical atmospheric attenuation curves for a standard atmosphere were developed for the MI sensor. Figure 5-2 shows the geometry of the attenuation problem and contains the symbols used in the theoretical correction factors. The first step is to determine the effective radiating temperature (ERT) of the target from the MI data. This can be done by visually matching gray shades or using a densitometer. Next, determine the zenith angle (θ) for the target. This can be done by producing a transparency copy of Figure 5-6 with 6.3 inches between β = 50° and θ = 60°. Figure 5-6 is for 1:15 million scale data. Data subpoint is determined by techniques described in Chapter 6. The Y-value (increased atmospheric depth) correction is determined by using

Figure 5-7. Enter Figure 5-7 with the ERT and zenith angle. The resulting correction can be read as either temperature or the approximate height error if the radiating target is a cloud. The X-value (atmospheric depth) correction is determined by using Figure 5-8. This figure provides an ERT correction due to the moisture present in a standard atmosphere. As in Figure 5-7, the correction can be read as either temperature or approximate cloud height error. Figure 5-7 is derived from the following equation:

$$ERT_{(corr)} = ERT + 0.0125 \ (ERT-220)$$
$$+ \ 0.00156 \ (ERT-220)^2 \quad (Eq \ 5\text{-}3)$$

For both Fig 5-7 and Fig 5-8, the temperature corrections are added to the ERT, and the cloud height corrections are subtracted from the cloud height determined by using the ERT and radiosonde temperature vs altitude information.

E. VHR Inv Mode Processing

The bit-frame structure is similar for both VHR and WHR data. Because of this it is possible to process VHR data as if it were WHR. In this manner all of the enhancement choices available to WHR (brilliance inversion and thresholding) are also available for VHR data. In the normal VHR display solar energy incident on the earth scene is reflected to the sensor and displayed as a positive image (dark objects appear dark, light objects appear light). When using the VHR Inv mode the image is inverted (dark objects appear light, light objects appear dark). Since visual data are processed as if they were infrared, and the infrared processing controls are labeled in terms of temperature, then it is necessary to determine the correspondence between albedo and temperature.

In order to convert from temperature to albedo the calibration of the VHR sensor must be known. This sensor is calibrated to give a fixed voltage when viewing a 100% albedo target at subpoint. The full range response of the VHR sensor is 0 - 4.0 volts. On spacecraft FTV 1524 and FTV 2525 the calibration voltage was 2.3 volts.

Fig 5-5. WHR temperature response to known radiating bodies.
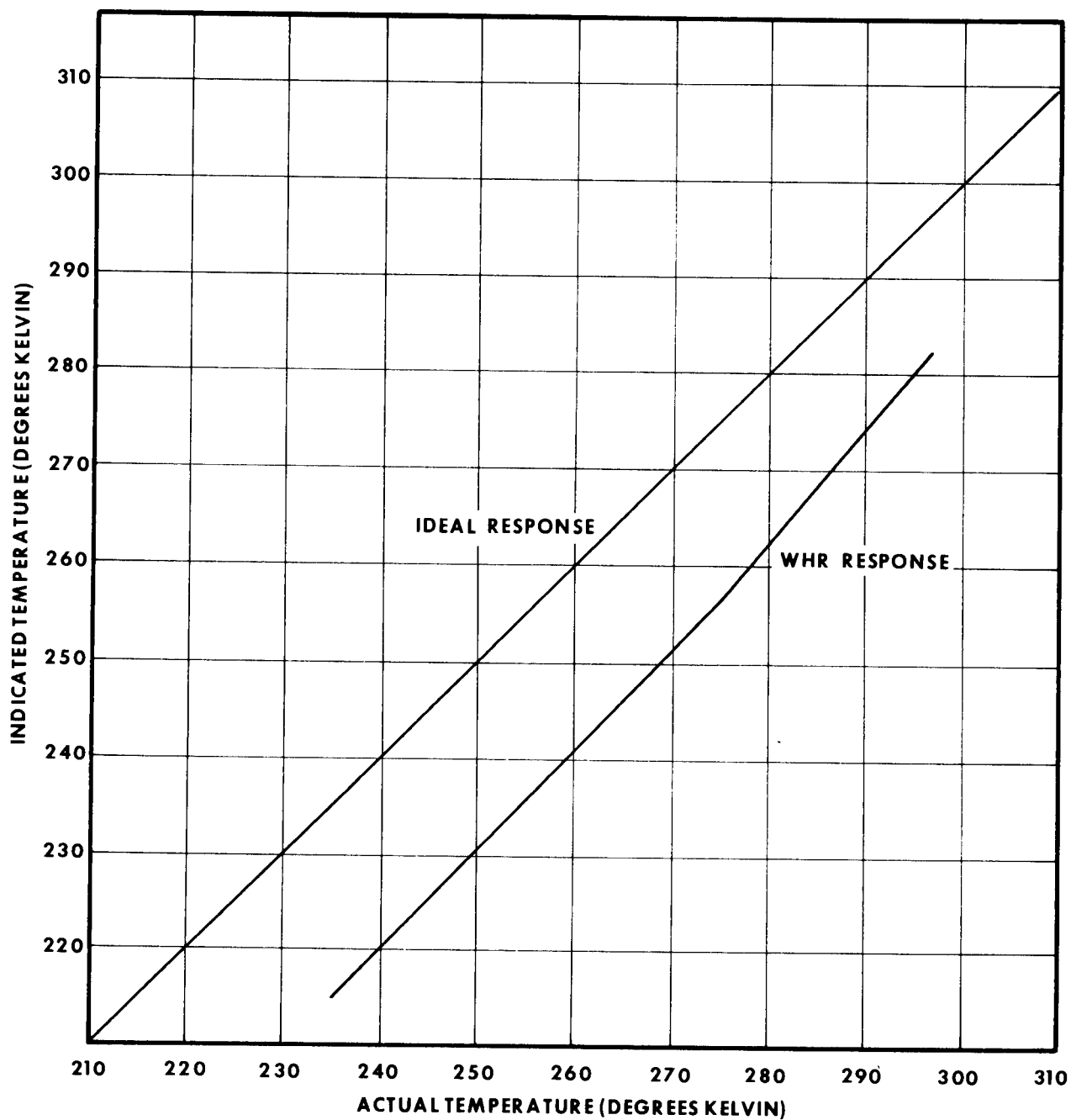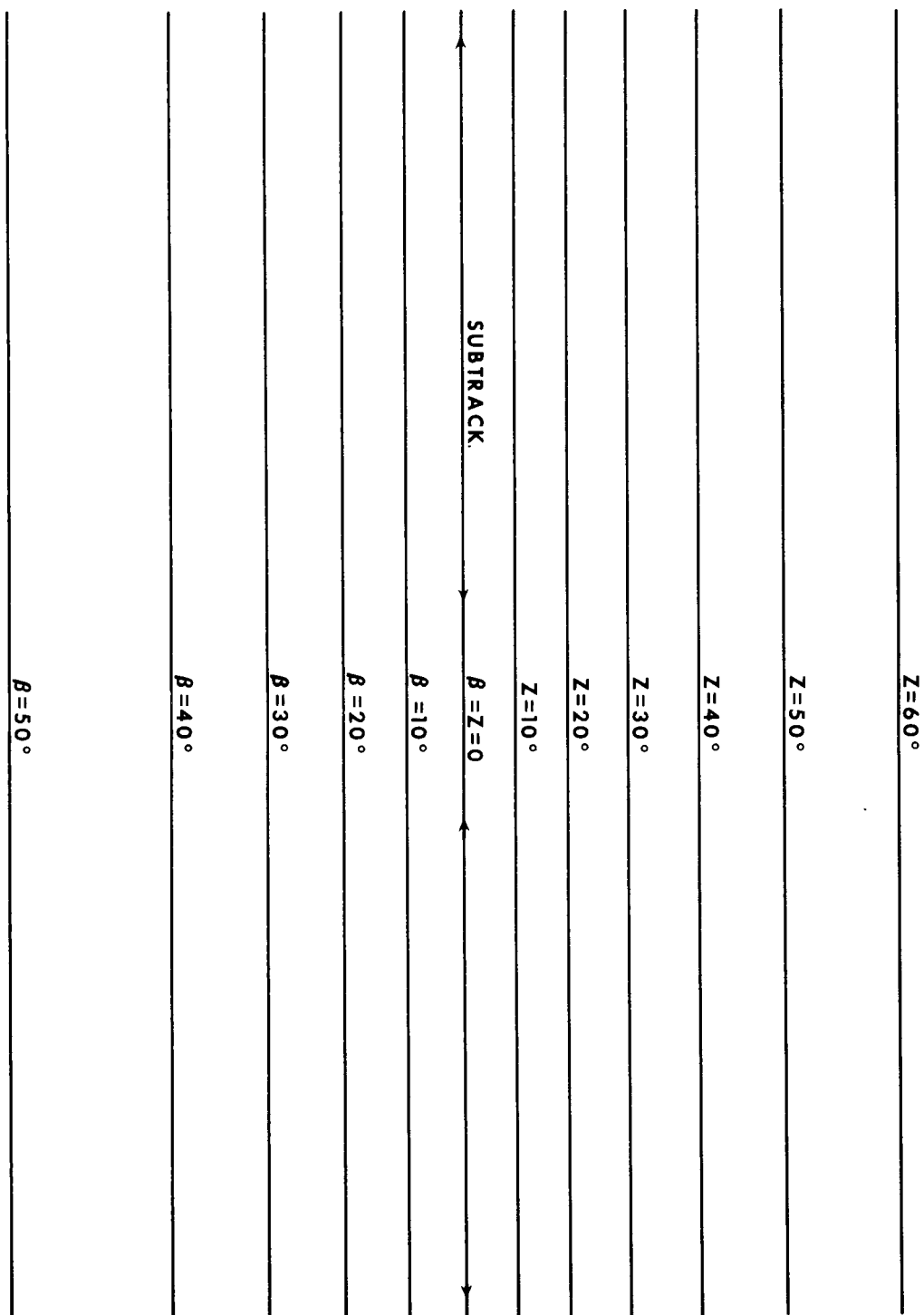
Fig 5-6.   Zenith (Z) and scan (β) angle overlay.
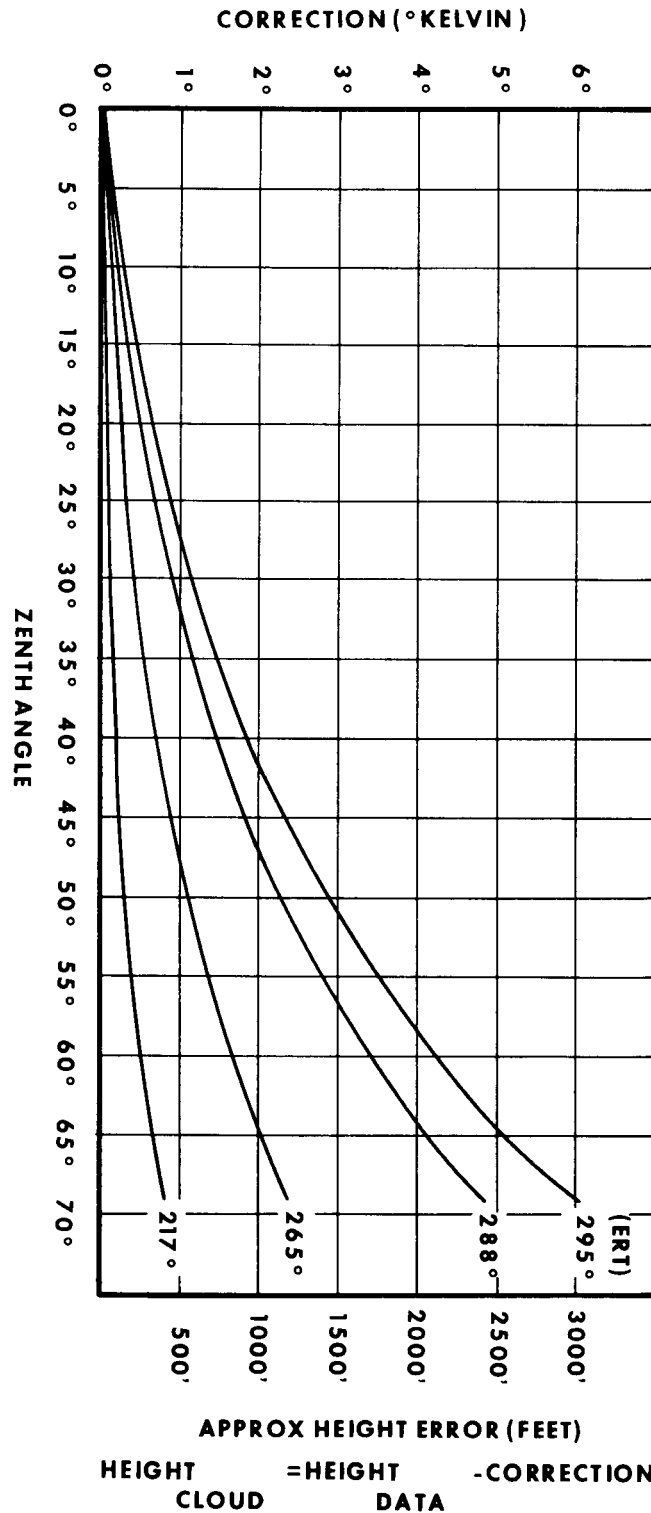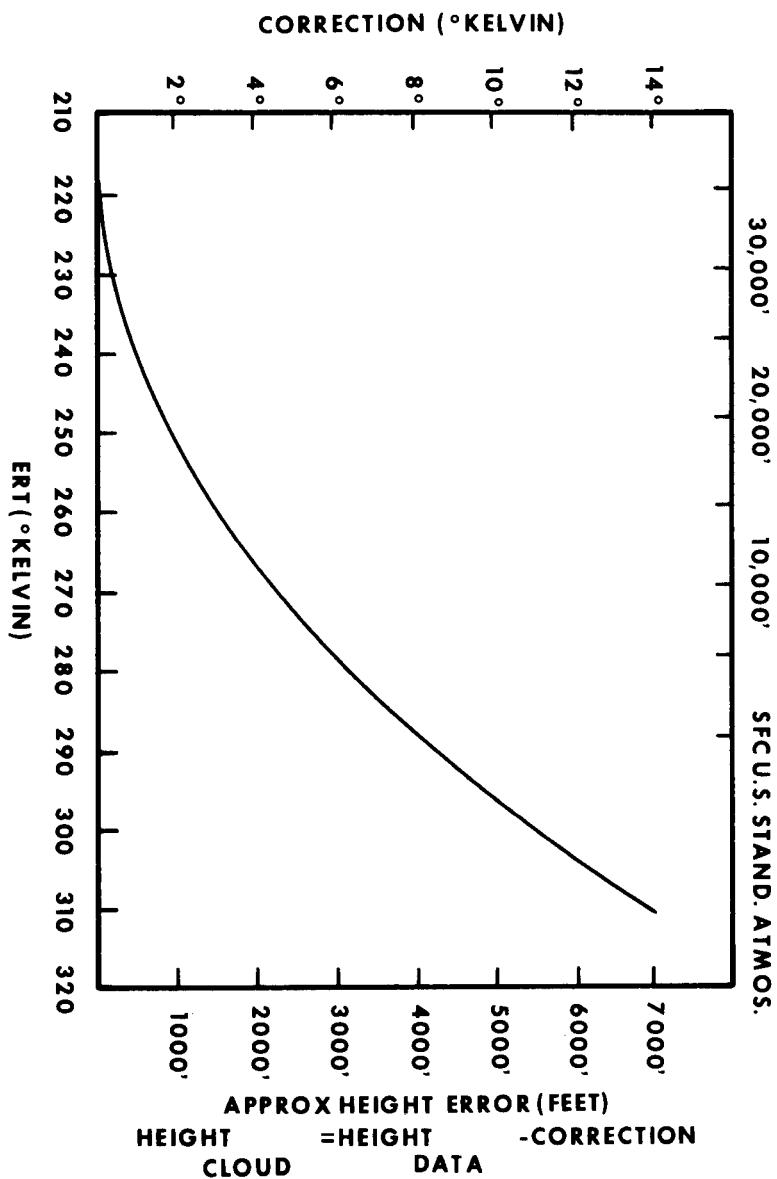
Fig 5-7. Y-value (increased atmospheric depth) attenuation correction.

Fig 5-8.   X-value (atmospheric depth) attenuation correction.

For FTV 3526 it was 2.39 volts. Holding the calibration voltage at these low levels permitted the sensor to respond to higher illumination values from targets well removed from the subpoint. However, experience showed that this condition seldom occurred near noon. Therefore, on later spacecraft the calibration has been different for morning and noon satellites. Morning satellites (e.g. FTV 7529) have the calibration voltage set at 2.5 volts. Noon satellites (e.g. FTV 5528) have the calibration voltage set at 4.375 volts. This means that a 100% albedo subpoint target will oversaturate the sensor; however, this rarely occurs and it proved advantageous to expand the dynamic range of the sensor over a slightly smaller range of albedos.

It is possible to represent albedo values as equivalent temperature settings (ETS) if two assumptions are reasonably valid. (1) Assume the illumination field is uniform throughout the scan of the earth scene. This is a good approximation for a spacecraft near a noon orbit. It is not as good for a morning orbit, so VHR INV is seldom used for a morning orbit satellite. (2) Assume the sensor control of along-track gain settings maintains a constant voltage output as a function of albedo input (e.g. at both 20°N and 60°N a 100% albedo target would show the same voltage). Barring a sensor malfunction, this is a good assumption. Table 5-3 lists the conversions between albedo and ETS for FTV 5528.

The earth-scene albedo for any given ETS may be determined by Equation 5-4.

$$\text{Albedo} = \frac{\text{ETS} - 210}{1.094} \qquad \text{(Eq 5-4)}$$

For example, an ETS of 250K corresponds to an albedo of 36.6%.

Producing VHR Inv mode data is similar to the brilliance inversion (BI) or the threshold (Thres) types; however, there is one important exception. With infrared data a Base temperature is selected and the shades of gray are distributed over a temperature range colder than the Base temperature. For example, a BI of 310 X1 distributes the 64 shades of gray from 310K - 210K. For VHR Inv the selected Base ETS represents the lowest albedo to be displayed, and the shades of gray are distributed over an albedo range toward higher albedo values. For example, a VHR Inv 310 X1 distributes the 64 shades of gray from 91.4% - 0 albedo. The range in this case is not 100% because of the 4.0 volt limit on the output of the VHR sensor. Due to this voltage limit albedos higher than 91.4% cannot be displayed. The albedo ranges are 91.4% for X1, 45.7% for X2, and 22.85% for X4.

VHR Inv products may be produced in Thresh Norm or Thresh Inv; however, BI can only be obtained in the Inv mode. As a result high albedo objects will appear dark. Enhancements and expand scales may also be selected for VHR Inv products.

Earth-Scene Albedo(%)	Output Voltage	Percent of 4.0 Calibration Voltage	Equivalent Temperature Setting (ETS)
100%	4.375	109.4%	319.4
90	3.9375	98.4	308.4
80	3.5	87.5	297.5
70	3.0625	76.6	286.6
60	2.625	65.6	275.6
50	2.1875	54.7	264.7
40	1.75	43.8	253.8
30	1.3125	32.8	242.8
20	0.875	21.9	231.9
10	0.4375	10.9	220.9
0	0	0	210

Table 5-3. Conversion of earth-scene albedo to voltage, calibration, and ETS for a noon satellite.

Many uses can be made of VHR Inv products. Some of them are: cloud albedo studies; terrain enhancements; precipitation intensity/quantity vs cloud albedo determination; albedo of river flood plains for river/flood forecasting; large scale land use study and changes in land use. Figure 5-9 is an example of VHR Inv 235 X4 data used for terrain enhancement. It is from the same data series used to depict DDS capabilities in Chapter 4. Where not cloud covered (black), subtle albedo differences in the terrain become apparent. Reservoirs stand out light against a darker background. South of Mexico, contoured in dark shades against a lighter ocean surface, is a trail of sun glint. Information about surface, wind speed, ridgelines, and sea state can be gleaned from sun glints (AWS TR 212, pp 3-H-15 to 3-H-17 and 3-I-8(4)). The albedo ranges in Figure 5-9 extend from 22.8% for the darkest shade of gray to 0% for the lightest shade. Comparison of Figure 5-9 with Figures 4-5 through 4-9 shows how the VHR Inv X4 mode increases a viewer's capability to identify objects in VHR imagery.

Compare Figure 5-10 with Figure 5-9. Figure 5-10 has been processed to show cloud detail for very bright clouds only. The albedos displayed range from 82.3% to 59.5%. Other high albedo examples will be shown in Chapter 7.

Fig 5-9. 19 Apr 1973, 5528/5536, VHR, Norm, Inv 235 X4, Off.

Fig 5-10. 19 Apr 1973, 5528/5536, VHR, Norm, Inv 300 X4, Off.

Chapter 6 - Data Location

A. Orbit Characteristics.

The ability to use DMSP data for mesoscale and synoptic applications is greatly enhanced by unique data location procedures. Data location, or gridding of data, is the physical process of placing longitude and latitude lines on the DDS-produced positive transparency or reproduced copy (hard copy). Being able to perform these procedures rapidly and accurately is an important asset of the DMSP system.

At the very best, accurate gridding is a complex science. An understanding is necessary of the sensing mechanism, spacecraft orbit, and display equipment. The sensing mechanism, already discussed in Chapter 3, employs fixed-speed scanning radiometers which measure reflected or emitted radiation amounts along a line perpendicular to the spacecraft's direction of motion. The scanners, as indicated in Figure 6-1, are essentially looking at a curved surface from a fixed point in space. The resulting effect is termed foreshortening. Not only are these data foreshortened because of "looking" over the curvature of the earth, but the spacecraft travels in an orbit

such that the longitude and latitude lines are curved and their orientation changes depending on the subpoint latitude.

The nominal orbit for the DMSP spacecraft is a 450 nm circular orbit with an inclination angle of 98.7° (exactly 98.747°). This means the orbital plane is inclined 98.7° to the equatorial plane where the spacecraft crosses the equator northbound (ascending node). Figure 6-2 shows the relationship between the orbital and equatorial planes. The 98.7° inclination angle was selected to insure that the nominal 450 nm circular orbit is sun-synchronous (maintains a relatively constant relationship to the sun so that the ascending node remains at a constant solar time). The combination of a 450 nm circular orbit and 98.7° inclination angle means that the satellite's orbital plane rotates slowly around the earth at the same rate and direction that the earth rotates around the sun. This precession rate of 360° per year (0.98563°/day) is, by definition, that of a sun-synchronous orbit (see Figure 6-3).

The 98.7° inclination angle also specifies the subpoint latitude limits

DIRECTION OF
SPACECRAFT MOTION

TRACK SUBPOINT
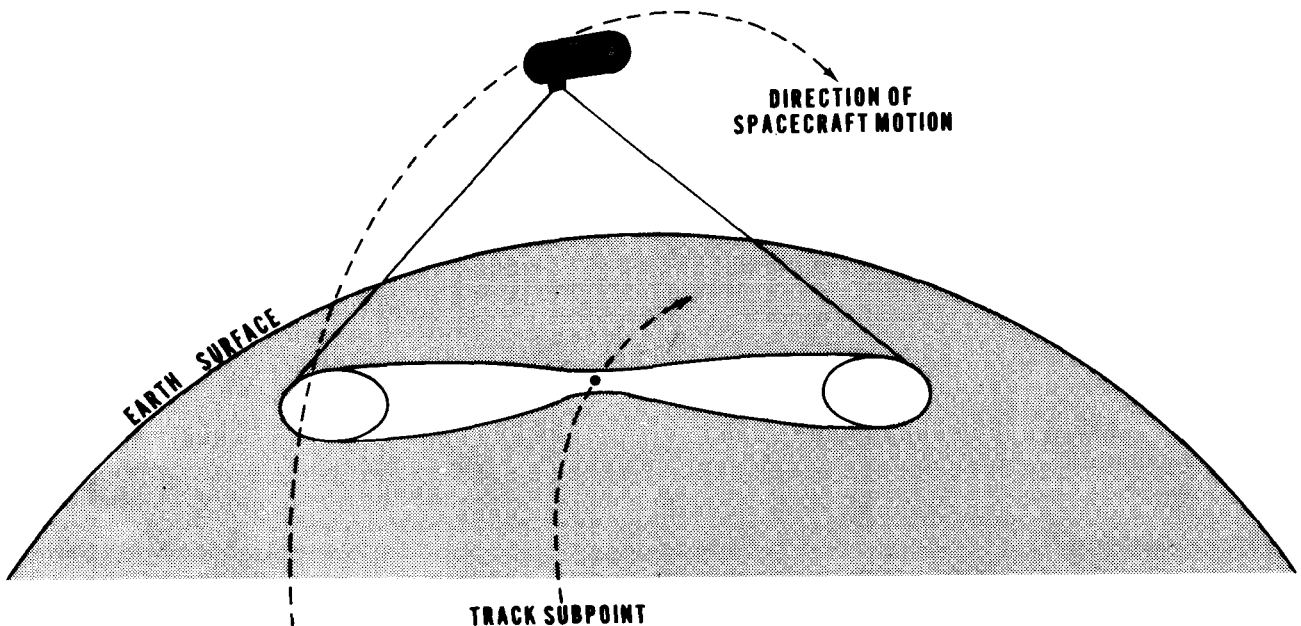
Fig 6-1.   Geometry of a scan line (not drawn to scale).
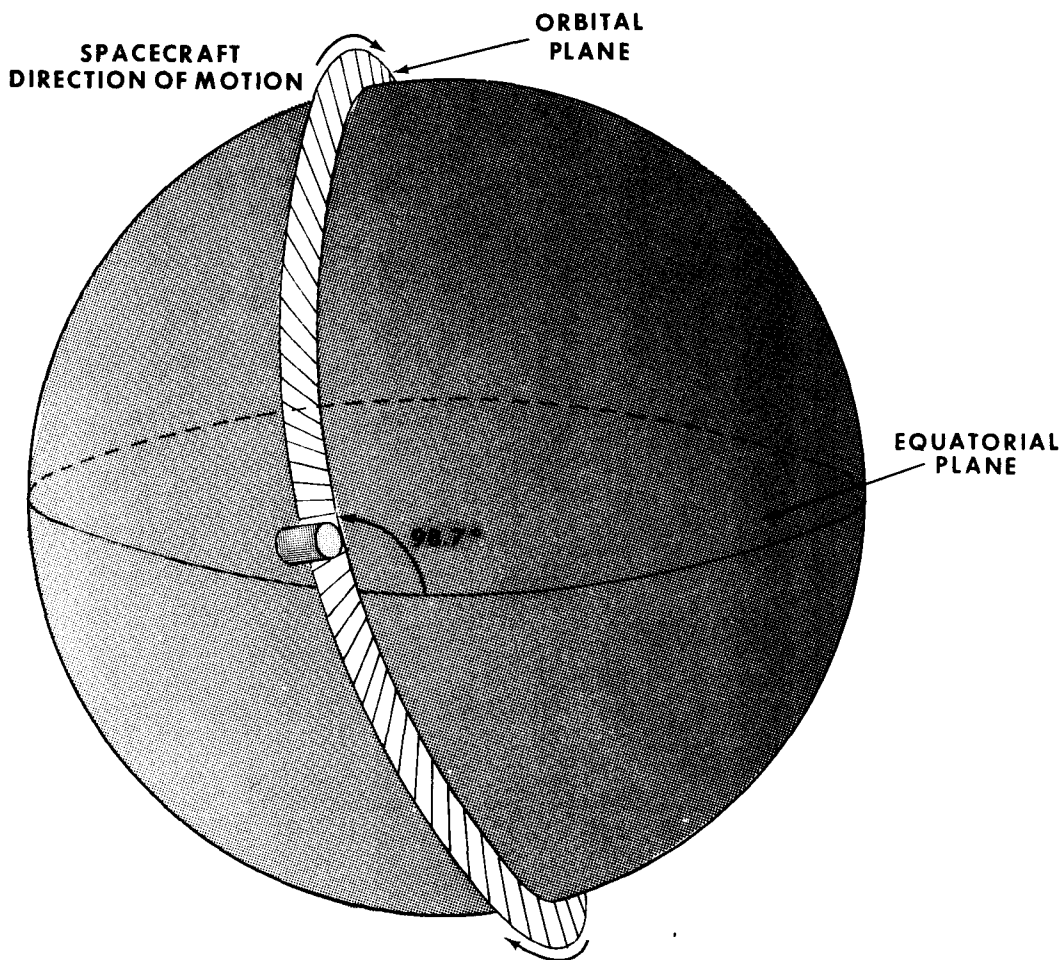
Fig 6-2. Nominal DMSP orbital inclination (not drawn to scale).

for the spacecraft. The spacecraft subpoint reaches 81.3°N and 81.3°S latitude each orbit. The sensor scans 13.3 degrees of latitude each side of the subtrack; therefore, at 81.3°N or S the imagery extends past the poles. At the most poleward positions of the spacecraft its motion is tangent to the parallels of latitude, adding to the complexity of a grid's latitude/longitude configuration.

The nodal period of this sun-synchronous orbit is 101.56 minutes. During the time of one revolution, the earth revolves under the orbit to the east and the orbital plane precesses slightly to the east. The result is that each nodal crossing is approximately 25.4 degrees west

of the previous crossing. As already indicated, with 13.3 degrees of longitude/latitude scanned either side of subtrack, imagery data are contiguous at the equator. During 24 hours, however, there is not an even number of revolutions. With a 101.56 minute period, 14 revolutions will occur in just under 1422 minutes and 15 revolutions take slightly more than 1523 minutes. Since a day contains 1440 minutes, every day has at least 14 revolutions. Each day's set of 14 revolutions occurs 4.54° farther east than the previous day's, and since the orbit is sun-synchronous, the fourteenth revolution occurs approximately 18 minutes (local time) earlier each day.

We define the first revolution
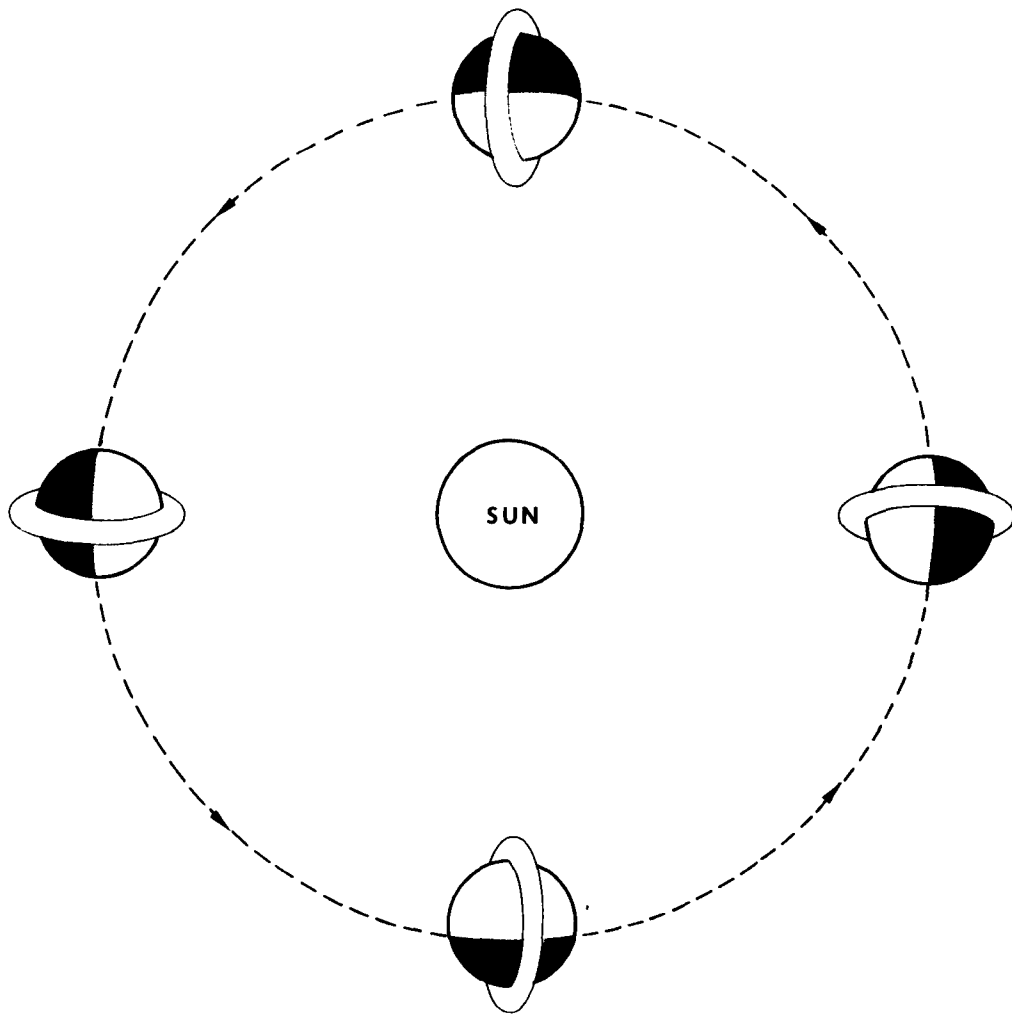
Fig 6-3.   View of a sun-synchronous, local noon, near polar orbit
           from Polaris. Note precession of the orbital plane
           through 360° during the year (not drawn to scale).

each day to have an ascending node
greater than or equal to 68°W as the
reference revolution, and call it
N=0 for that day. Each successive
revolution is N=1, 2, etc., up to
N=13 for an average 14 revolution day.
Due to the nodal crossing increment
near 25.4 degrees, N=0 occurs between
68°W and 93.4°W. Each 14 revolution
day's N=0 occurs 4.54° further west
than the previous day's N=0. Approx-
imately every five days there is a
15 revolution day; therefore, a space-
craft peculiar cycle is established
which causes both daily data coverage
and local time of data variations.

Table 6-1 shows the possible nodal
crossing longitudes during a day for
a nominal orbit. The further east
within a nodal crossing zone a revolu-
tion occurs, the earlier (local time)
it begins.

B.   Gridding Technique.

Once DMSP data are acquired, only
the longitude of nodal crossing and
the elapsed time since the nodal
crossing are needed in order to
accurately locate these data. The
grids (longitude/latitude lined
acetate strips) consist of either

Revolution	Longitude (AN)	Longitude (DN)
0	68.0 - 93.4W	99.3 - 73.9E
1	93.4 - 118.8W	73.9 - 48.5E
2	118.8 - 144.2W	48.5 - 23.1E
3	144.2 - 169.6W	23.1E - 2.3W
4	169.6W - 165.0E	2.3 - 27.7W
5	165.0 - 139.6E	27.7 - 53.1W
6	139.6 - 114.2E	53.1 - 78.5W
7	114.2 - 88.8E	78.5 - 103.9W
8	88.8 - 63.4E	103.9 - 129.3W
9	63.4 - 38.0E	129.3 - 154.7W
10	38.0 - 12.6E	154.7W - 179.9E
11	12.6E - 12.8W	179.9 - 154.5E
12	12.8 - 38.2W	154.5 - 129.1E
13	38.2 - 63.6W	129.1 - 103.7E
14	63.6 - 68.0W	103.7 - 99.3E

Table 6-1. Nominal ascending and descending nodal crossing longitudes for a 25.4° longitudinal drift rate.

1:15 million or 1:7.5 million map scale overlays, and are constructed to match the sensor view from a nominal 450 nm orbit. Meridians are not labeled so that the grids are universal. The data display segment (DDS), previously shown in Figure 4-1, electronically shapes the sensor signal and displays it to fit one of the grids. The DDS produces a strip chart, rectifies the imagery by re-moving foreshortening, and compensates for deviations from the nominal space-craft altitude and attitude. Thus, while accurate gridding is complex in principle, the actual mechanical process is greatly simplified for DMSP data by the DDS.

There are some slight differences in the DDS equipment used at AFGWC when compared to those at the tactical sites. The differences were described in Chapter 4. One of those differ-ences is in the compensation for space-craft altitude. At AFGWC a continuous sinusodial correction is applied to the imagery. A tactical site usually sets one altitude setting into the DDS which is assumed to be valid for the few minutes the spacecraft is within readout range of the site. In this section we shall describe tactical

site gridding procedures since they may be applied to imagery sections from both tactical sites and AFGWC.

Since the grids are longitude independent, an individual revolution is gridded with reference to the longitude of nodal crossing, either ascending or descending. The grid is aligned with respect to a line on the right side of the grid which is parallel to the dashed data center line, and fiducials which appear on the right-hand side of the picture. These fiducials are generated by the DDS. If the equipment is proper-ly maintained, the fiducials will always be 4.225 inches from the data subpoint on 1:15 million scale data; and center expand, 1:7.5 million data. Careful gridding also involves proper along-track alignment of the grid. An example of a section of DMSP imagery with a grid properly aligned on it is shown in Figure 6-4.

A computer product is available at all site locations which provides the user information for data loca-tion. Besides providing the satellite altitude at any latitude, it provides the time it takes the spacecraft and the imagery sub-point to reach any
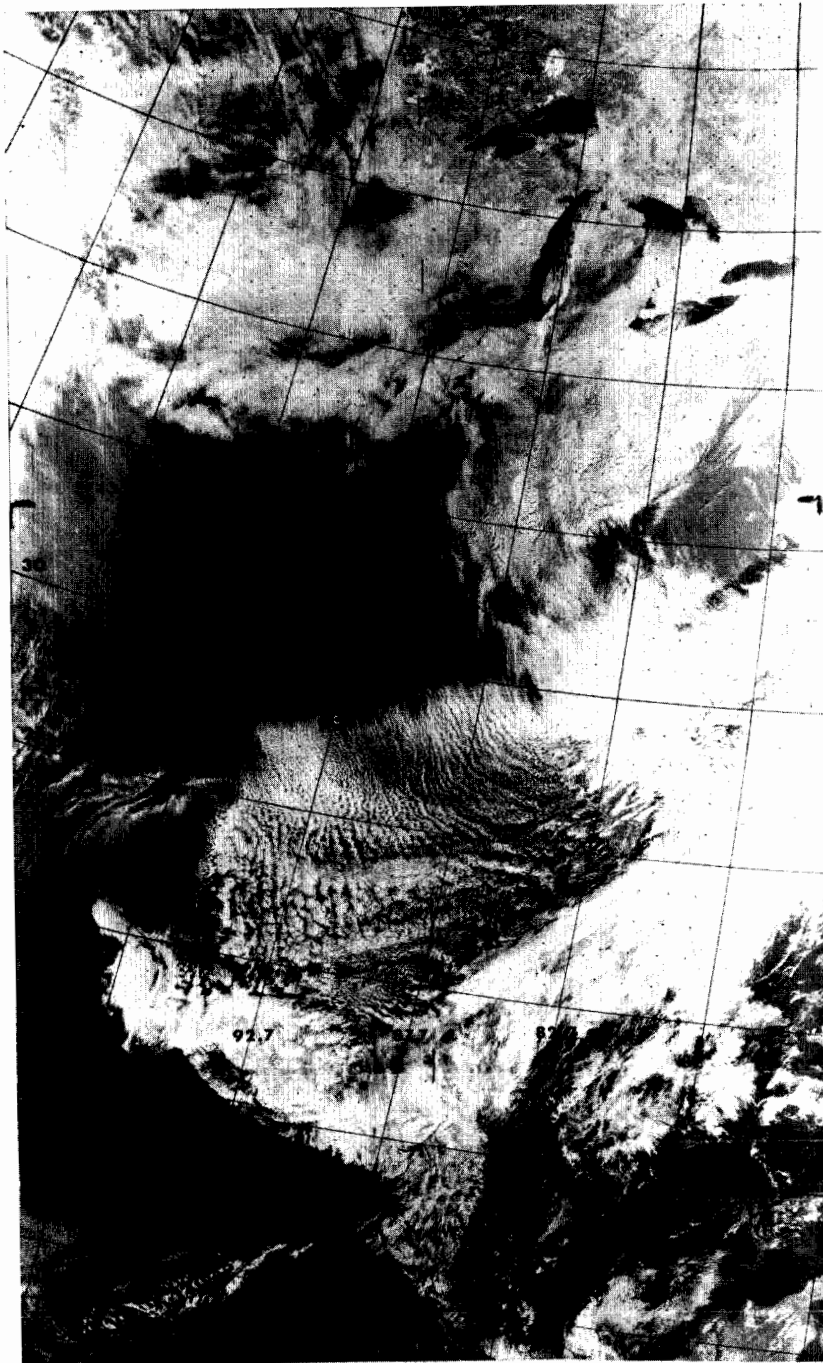
Fig 6-4. Gridded data example, 29 Jan 1973, 5528/4404,
VHR, Norm, Norm Off.

latitude. The time it takes the
spacecraft to reach a latitude,
either prior to or after equator
crossing, is delta time (Δt). The
data-subpoint may precede or lag
the spacecraft subpoint due to
slight spacecraft pitch error, or
ellipticity of the actual orbit.
The time for the data-subpoint
to reach a latitude is given in
elapsed seconds. For example, the
elapsed time to reach 30°N for a
nominal orbit is 508 seconds. Tech-
nicians operating the display equip-
ment manually initiate the Orbit
Time generator in the display equip-
ment (Chapter 4) normally using the
convention that at the time the
data-subpoint crosses the equator
northbound, the Orbit Time generator
will read 00000 (overflow). At that
point a fiducial and time tag of
00000 are printed in the right-hand
margin of the film. Every two minutes
thereafter another fiducial and time
tag (e.g., 00120, 00240, etc.) are
printed. (See Figures 6-4 and 6-5).
In Figure 6-4 the time tag is so
lightly printed that the reader may
not be able to see it. Between
fiducial/time tag pairs are repeated
"data cards" upon which can be dis-
played the type of data and enhance-
ment, scale, or threshold modes used.
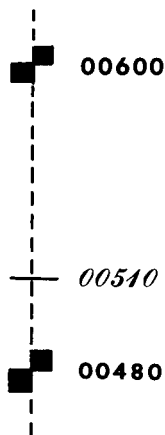
Fig 6-5. Interpolating for latitude
of interest.

Once the Orbit Time generator is
initiated, the along-track placement
of the grid involves choosing a
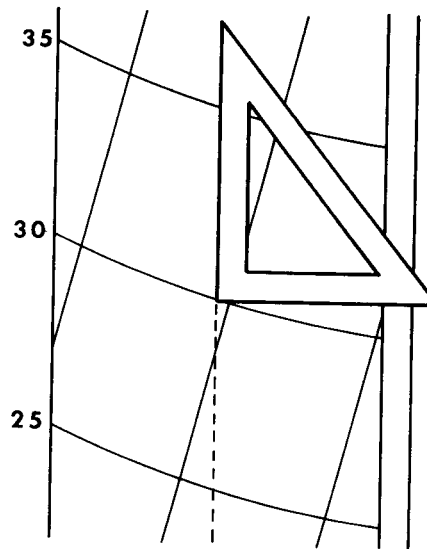
Fig 6-6. Aligning right triangle to
subpoint latitude of
interest.

latitude. For example, if 30°N is the
latitude of interest, and 00510 is the
data-subpoint orbit time for that
latitude, then one has to interpolate
between the fiducials in order to grid
the imagery. If the time tags read
00480, 00600, etc., 00510 seconds is
one-fourth the distance between the
centers of the two fiducials (Figure
6-5).

This point coincides with the
location of 30°N at subpoint. Unless
a grid is available with offset lines
indicating the latitude of the sub-
point at the proper relative position
along the edge of the grid (AFGWC has
some of these grids), the following
method is used. A right triangle is
aligned with one side along the dashed
data center on the grid. The right
angle corner is placed at 30°N (Figure
6-6). The line formed by the triangle
should then be matched to the inter-
polated orbit time for 30°N on the
imagery.

The gridding procedure is accom-
plished by placing the grid and
triangle on the imagery such that a
line drawn on the grid 4.225 inches
to the right of the dashed data-sub-
point line falls along an imaginary
line through the center of the
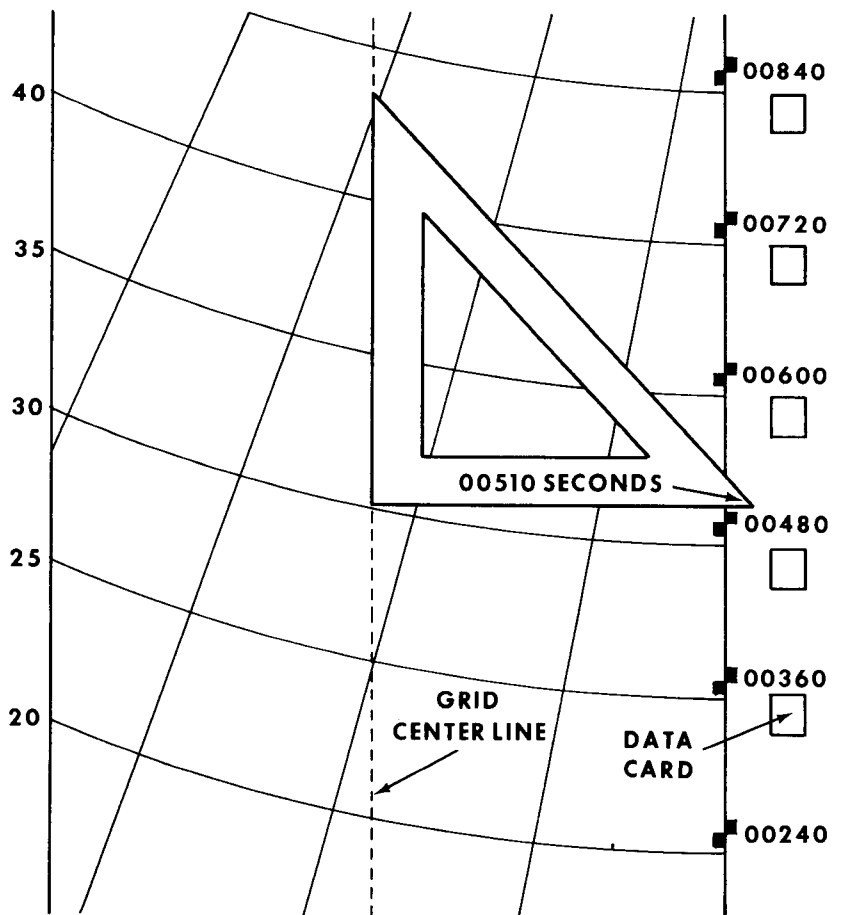
Fig 6-7.   Gridded data schematic.

fiducials. The grid is shifted up or down on the imagery until the base of the right triangle and the interpolated orbit time coincide (Figure 6-7). If the DDS equipment has been properly maintained and the proper setting placed into it, then the grid should be accurate at 30°N. Quick check of geography in the vicinity of 30°N should verify the grid placement, or at worst, cause a slight grid adjustment. The entire length of data will not be precisely gridded since the DDS settings are exact for only one latitude. Increasing along track distance from the

latitude of interest will show larger error.

Meridians are labeled according to ascending (descending) node values. Each grid is drawn so that a meridian line crosses the equator at the ascending node. It is labeled to nearest tenth degree, and there are printed meridians every five degrees. By following the data location procedures on properly maintained readout equipment, land or cloud features can be located within 1.5 nm across track and 3.0 nm along track on the center line. This error may grow

toward the edges of the imagery where it may be as much as 8 nm across track and 13 nm along track.

C. Object Altitude Data Location Error

Cross track data location errors can result from cloud height. This is because the DDS rectification function, based on a spherical earth model, positions data on the film as a function of sensor scan angle, for a particular satellite altitude, irrespective of the height of that data above the surface of the earth. As a result, as the sensor scans outward from the nadir, it views cloud sides, rather than just cloud tops, and the DDS projects these data as if it were directly on the earth's surface. This presents an apparent scale expansion, such that clouds are "painted" on the film farther from the center line than they should be.

A correction can be applied for this cross track error if the cloud height (h) is known. Once h is established from aircraft observations, MI-data, or soundings, a position error (Δ) in inches on the picture is obtained from one of the charts in Figure 6-8. The charts are drawn for various satellite altitudes (H). Figure 6-8 can be used by entering the appropriate chart at the value of (S) (distance of the cloud from the centerline of an expand left/right in inches) and read the correction Δ in inches for the cloud altitude h. Subtract Δ from S to determine the correct location (S') of the cloud from the picture's centerline. Figure 6-8's charts are configured for the expand mode (1:7.5 million) scale, which is the scale most likely to be used in situations where cloud location accuracy is vital. The charts may be applied to the normal mode (1:15 million) scale simply by halving the value of S.

D. Fictitious Display Settings to Acquire Additional Data.

There are occasions when a user needs to see DMSP imagery that is close to, but beyond the edge of the scan line displayed in the picture. This particular problem was investigated by Boselly, Burgmann, and Waltman [10]. They considered how a grid was constructed and based their calculations on the distance from the grid center line to the edge of the grid (half data width-DW), which is 799 nm across track distance. From a 450 nm altitude, DW of 799 nm and assuming a spherical earth, the resulting scan angle (B) necessary for imagery to be properly displayed to match the grid is 55.61°. However, the DMSP sensors are designed for a half scan of 56.25° (B'). As a result, the spacecraft sensor's "see" an additional 0.64° of scan beyond that which is displayed. This overscan amounts to 31 nm on the earth's surface (Figure 6-9).

There are two ways to display the overscan area seen by the sensors, but truncated by the DDS to match the imagery to the grid scale. One is to use a fictitious roll setting. If a one degree roll correction is used, this changes the apparent angle B from 55.61° on both sides of the imagery to 54.61° and 56.61° respectively. This means that an added 50 nm would be available along one edge of the imagery, and slightly less than 50 nm would be missing from the other edge. This non-symmetrical view is considered inferior to the view generated by the other overscan area technique, the fictitious altitude setting. The objective in using a fictitious altitude setting is to make the DDS "think" the spacecraft is viewing the earth from a lower altitude than it really is. Figure 6-10 shows the effect on scan line sweep length for a spacecraft at an altitude less than 450 nm. With equal scan angles, data are lost at the edges in order to maintain a fixed grid scale (DW=799 nm). By using an altitude setting lower than the real altitude, the scan angle to be displayed can be increased from 55.61° to 56.25°, thus giving more scan line display on both edges. If the spacecraft is at an altitude greater than 450 nm then considerably longer scan lines are sensed and truncated by the DDS to match the grid scale. A fictitious lower altitude will allow more, if not all, of the scan line to be displayed. Table 6-2 gives data half width as a function of spacecraft height for B=55.61° and B'=56.25°. For altitudes greater than 450 nm the scan length sensed but not displayed is determined by subtracting 799 nm from the values
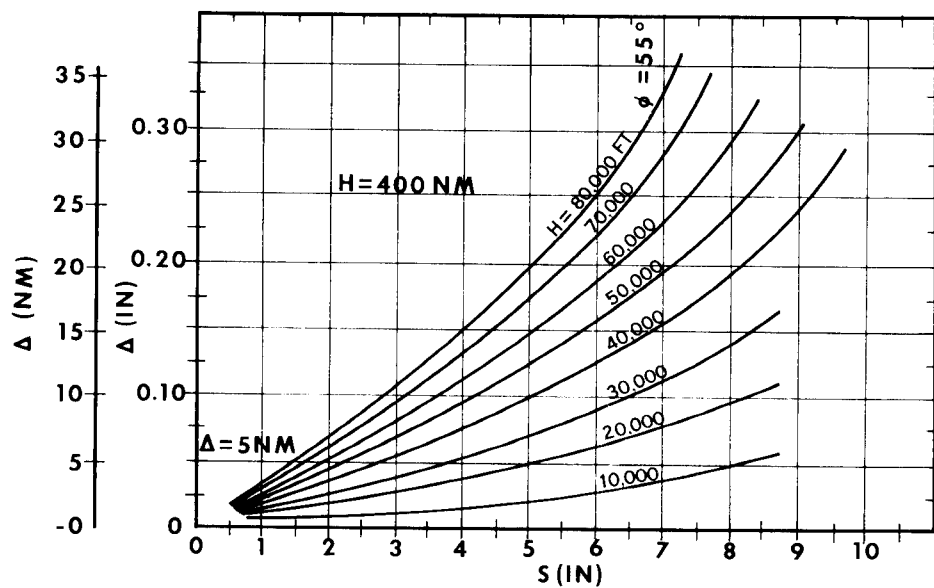
DATA LOCATION ERROR Δ AS A
FUNCTION OF DISTANCE FROM SUBTRACKS
ON EXPAND MODE DATA FOR VARIOUS CLOUD HEIGHTS h
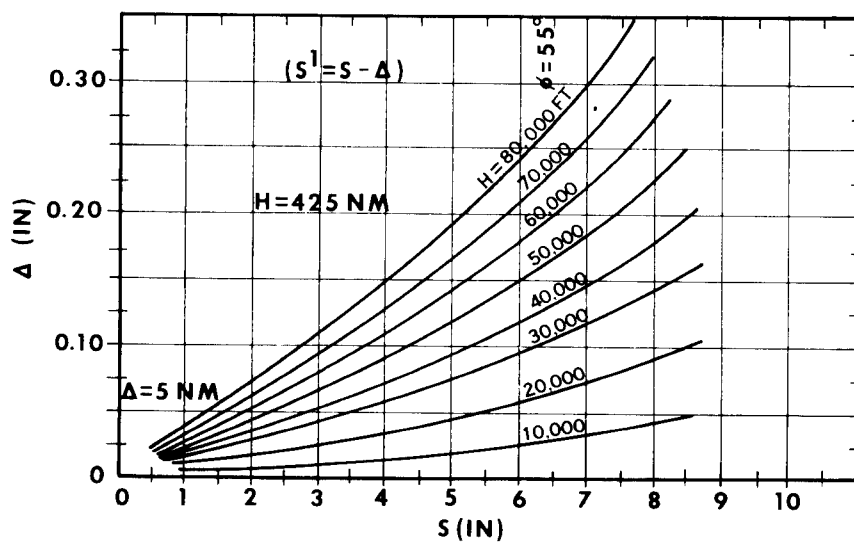
Fig 6-8.   Data location error.
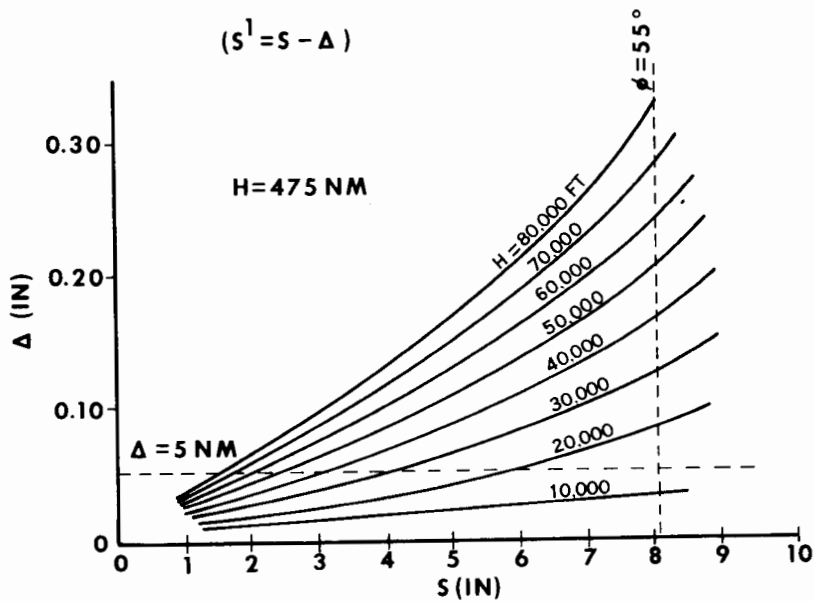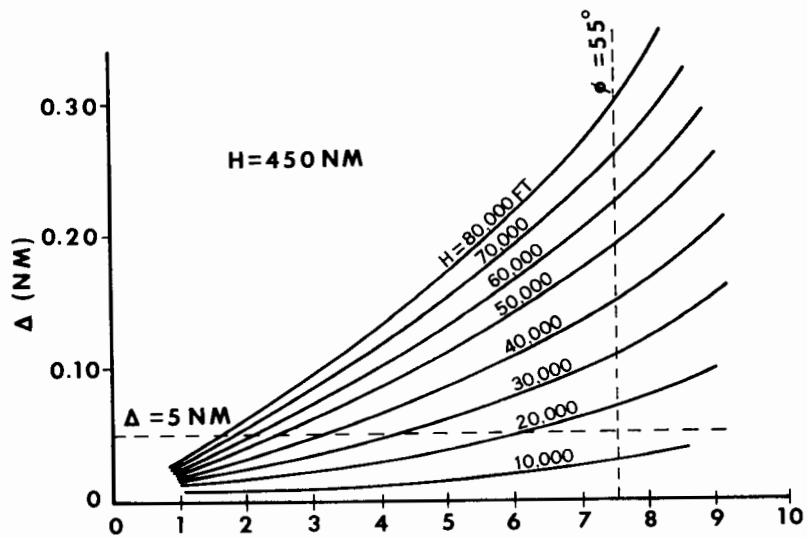
Fig 6-8. Data location error
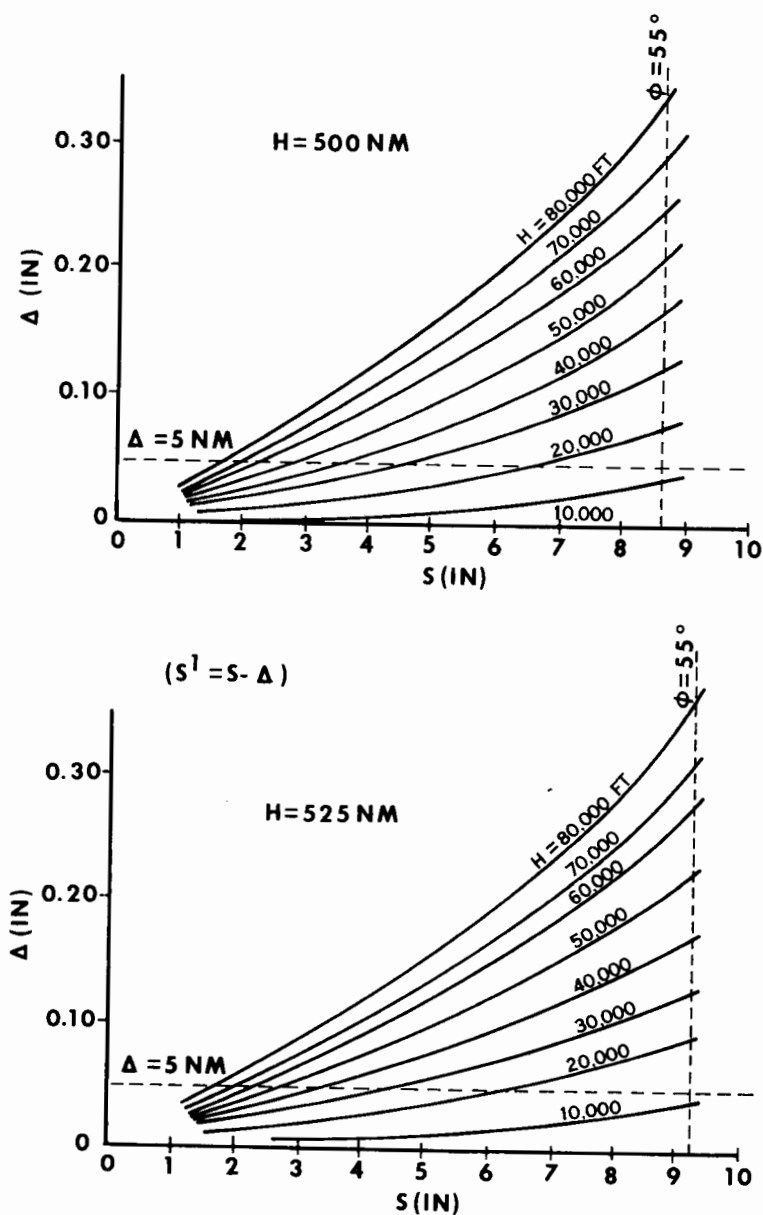
Fig 6-8.   Data location error
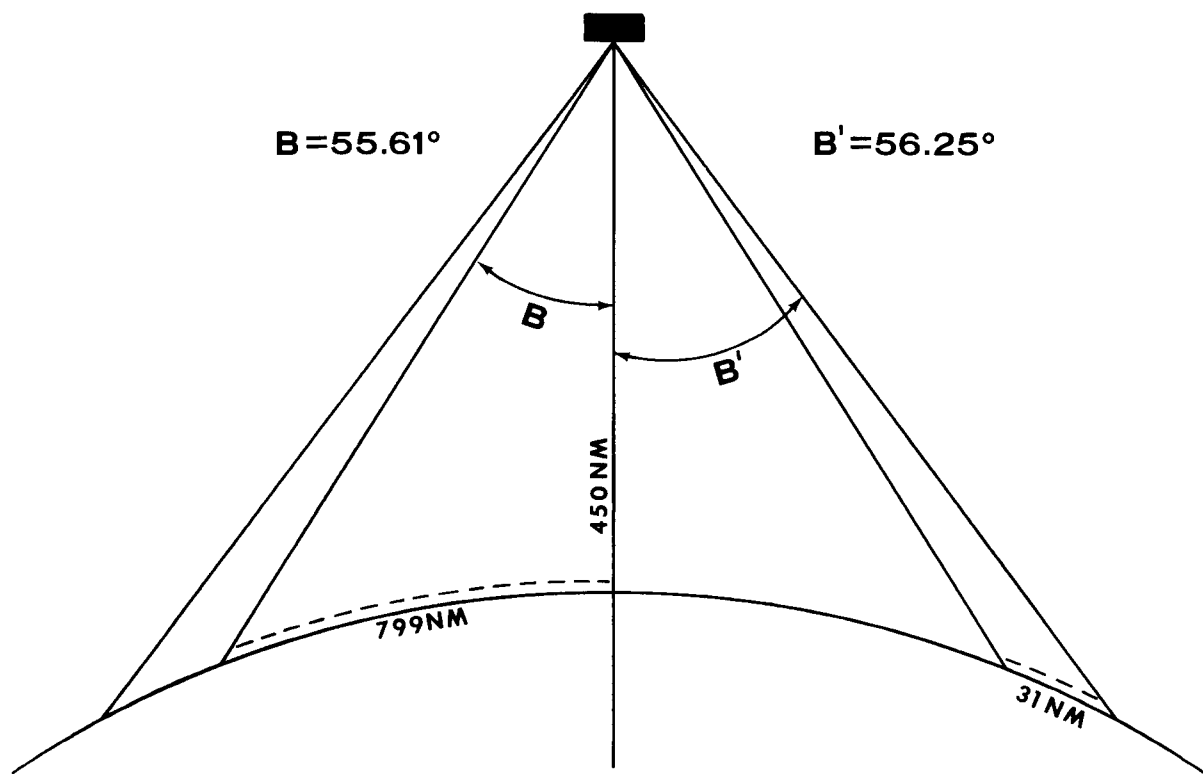
Fig 6-9. Sensor view and overscan (not drawn to scale).

h (nm)	DW, B=55.7°	55.61°	DW, B'=56.3°	56.25°
430	757	754	784	782
435	768	765	796	794
440	780	776	808	806
445	791	788	820	818
450	803	799	832	830
455	814	811	844	842
460	826	822	857	855
465	838	834	869	867
470	850	846	882	880
475	862	858	895	893
480	874	870	908	906

Table 6-2. Data half width as a function of height and angle.

December 1974   Technical Report 74-250
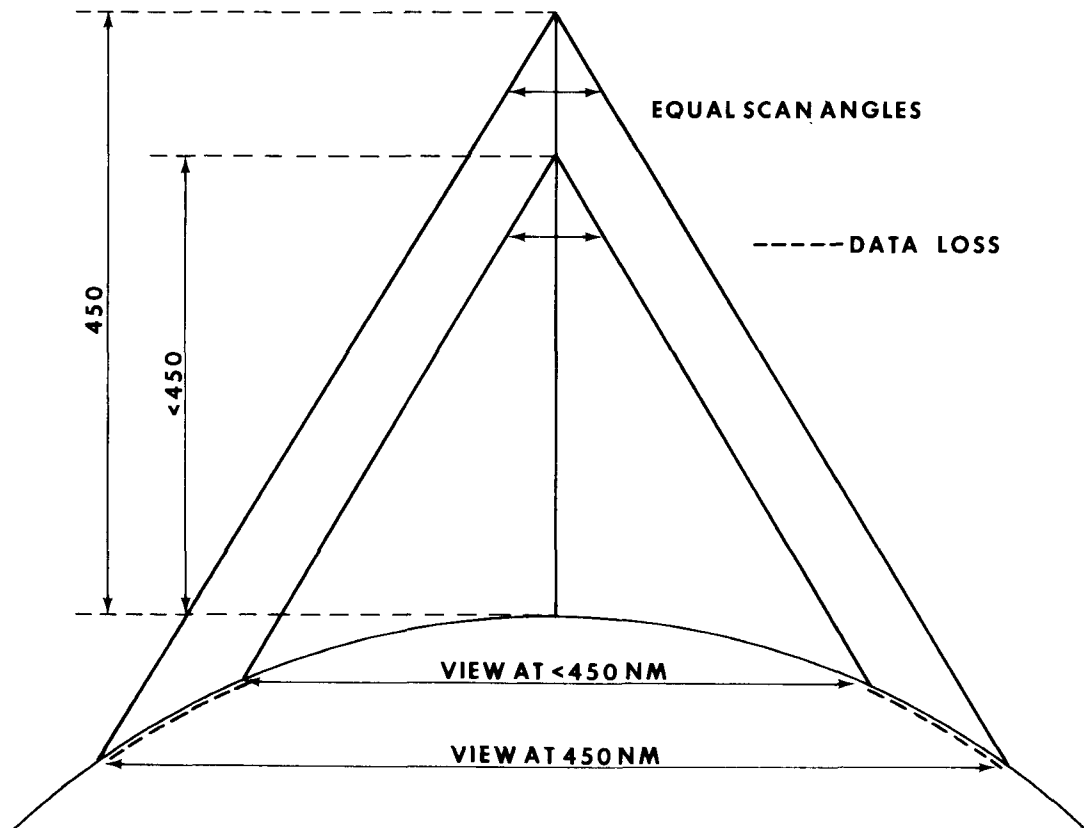
Fig 6-10.   Sensor view from spacecraft at different altitudes.

given in the 56.25° column. The table can be used to see if a particular interest area lies within the oversweep portion of the scan line, therefore having a possibility of being displayed with a fictitious lower altitude setting.

When fictitious altitude settings are used, accurate gridding using the existing grid is not possible since extra data have been squeezed into the 7.78 inches of displayed scan line length, and the along track length of data has been stretched by the DDS to compensate for the supposedly lower and faster moving satellite. Data in the overscan region have the poorest spatial resolution of any portion along the scan line.

Chapter 7 - DMSP Data Application Techniques

A. General.

This chapter will show how select-
ed meteorological cloud patterns
appear in DMSP imagery, describe
several applications that have been
found by AWS DMSP personnel, and show
some non-meteorological features that
appear in the imagery. No attempt
will be made to provide a complete
text on meteorological satellite data
interpretation. Good texts already
exist for this purpose. They are:
Anderson et al [11], with two supple-
ments; Anderson and Smith [4], also
Skidmore and Purdom [12]; Anderson et
al with Anderson and Veltishchev,
editors [13]; and a publication by
Bittner and Ruggles [14] which con-
centrates on satellite infrared
imagery. These texts should be con-
sulted in order to derive a basic
understanding of satellite data
interpretation. This chapter assumes
the reader already has knowledge of
basic meteorological satellite
imagery interpretation techniques.

Figures 4-5 through 4-19 all show
visual and infrared imagery (different
processing modes) for Mexico and the
western half of the United States on
19 April 1973. Figure 7-1 is a copy
of the Daily Weather Maps [15] surface
chart at 0700 E.S.T for that date.
The noon local solar time line nearby
bisects the satellite imagery examples
from top to bottom; thus, the Chapter
4 figures are approximately seven
hours later than Figure 7-1. The
satellite pictures provide a different
view of the weather situation than the
surface chart does. Obviously, the
satellite views the tops of the clouds
associated with the weather systems;
also, being later in time, the
satellite view allows the meteorologist
to observe the motion of the weather
systems. However, the most important
differences are that the satellite
"sees" both the big (synoptic) and
little (mesoscale) features at the
same time, and provides excellent
clues on the intensity of the weather
systems. The surface chart is
limited by station density and the
observer's viewing range. Upper air
charts are further limited by the
lack of adequate data to define

weather features in the mesoscale.
The point being made is that meteor-
ological satellite pictures and con-
ventional meteorological data are
complementary and should be used to-
gether in order to adequately define
the state of the atmosphere.

The figures in Chapter 4 show
that the occlusion, which the surface
chart shows across California, is
very weak. Few clouds can be assoc-
iated with it over land, and none
over the waters adjacent to California.
Using the visual and infrared imagery
together allows us to confirm that
the occlusion brought moist air aloft
into Nevada, Arizona, and Utah, where
thunderstorms are building near the
mountains. The satellite pictures
confirm the judgement which went into
labeling the cold front in New Mexico
as undergoing frontolysis. It is
obvious that the cold front from
Nebraska through Texas into Mexico
is the major front associated with
the low. The satellite pictures
graphically show the cirrus associated
with thunderstorms along the front
which has moved eastward from the
surface chart position. As mentioned
in Chapter 4, the use of the infra-
red with the visual data shows that
the portion of the front along the
Mexican Gulf Coast is far less active
than farther north. Few clouds of
any sort extend into Mexico from the
front. The imagery shows several
lines of thunderstorms associated
with the complex frontal structure
near the low. An upper air ridge
line is depicted in the infrared by
the cirrus clouds north of the vortex.
In the northwestern part of the
pictures, open cellular stratocumulus
is apparent off shore from Oregon, and
a greater density of cumulus and strato-
cumulus on shore. The surface chart
confirms that precipitation is in
those areas.

The use of Figures 4-5 through
4-19 along with Figure 7-1 makes an-
other point clear in addition to the
complementarity of satellite and
conventional meteorological data; that
is, the enhancement modes and data
formats of the DMSP system allow
greater flexibility and precision in

7-1
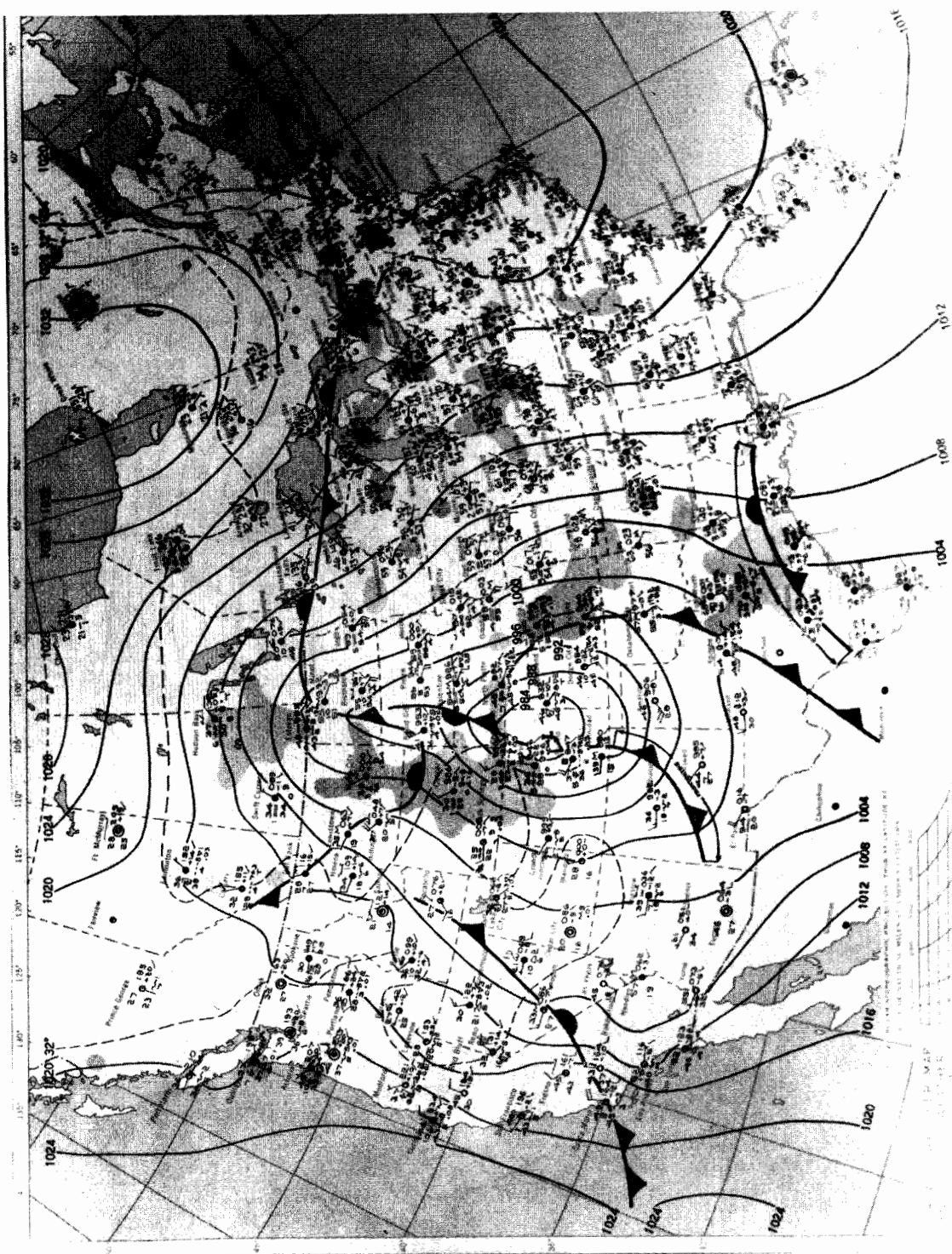
Fig 7-1.   Surface weather map for 0700 EST (1200%), 19 Apr 1973.

determining the state of the atmosphere. This is why Dr. John L. McLucas, Secretary of the Air Force, stated in the public announcement of DMSP (then DAPP) [16], that it "forms the most responsive operational data system of its kind."

stratocumulus west of Baja California, and for the most part it did not contrast well with the land, so remained invisible over most of Mexico. Where it was visible, one could not be sure what cloud type it was or at what level it existed. This example

Fig 7-2. Cirrus detection. 23 May 1973, 5528/6017, VHR, Norm, Norm, Off.

Figures 7-2 and 7-3 show the area in Mexico and southwestern U S that is common with Figures 4-5 and 4-19. In the visual data of Figure 7-2 there are faint signs of cirrus clouds arching nearly all the way across the picture. This cirrus is associated with a subtropical jet stream. The cirrus clearly shows in the infrared data of Figure 7-3. This situation is a common occurrence where the cirrus is optically thin in the visual wave lengths, but is emissively much colder than the background. In the visual data the cirrus was nearly invisible against the

demonstrates the meteorological value of having both visual and infrared data available, in the same scale. Caution is in order, however, about trying to use the infrared expand and invert to determine precisely what the emissive temperature is at the top of the cirrus. Because the cirrus is thin, warmer emissions from below penetrate the cirrus and contaminate the cloud top's emissive temperature. As a result, the integrated emissive temperature detected by the sensor is too warm, indicating the cloud tops several thousand feet too low. There is no easy correction for this phenomenon.

In Chapter 5 the thermal accuracy of the MI and WHR sensors was discussed. It was shown that the MI sensor is thermally more accurate than the WHR sensor, and in Figure 3-7 a portion of WHR imagery was shown.

integration to a single gray shade of a field of small cumulus elements. The other minor effect is that of the difference in thermal accuracy between the two sensors and is in favor of the MI sensor. The more eye-pleasing

Fig 7-3. Cirrus detection. 23 May 1973, 5528/6017, MI
Norm, Inv 310 Xl, Off.

Figures 7-4 and 7-5 are coincident WHR and MI data in the vicinity of the Himalaya Mountains. They are processed with the same thermal expand settings in the DDS. Note that the WHR example has sharp, crisp infrared features while the MI example appears fuzzy in comparison. Since the spectral and thermal ranges are the same for the two sensors, the apparent difference is caused by two additional effects. The major effect is that of spatial resolution. Resolution of 2.4 nm instead of 1/3 nm causes a smearing effect along cloud edges or an

appearance of WHR data is due to the improved resolution. It was mentioned in Chapter 5 that MI data should be used in preference to WHR data if quantitative thermal determination is desired.

B. Synoptic Patterns.

Fronts are very commonly observed in DMSP imagery. Frontal cloud characteristics are well described in [11]. The important advantages of DMSP data are the frequency of observations (four times per day) and the ability to use complementary visual

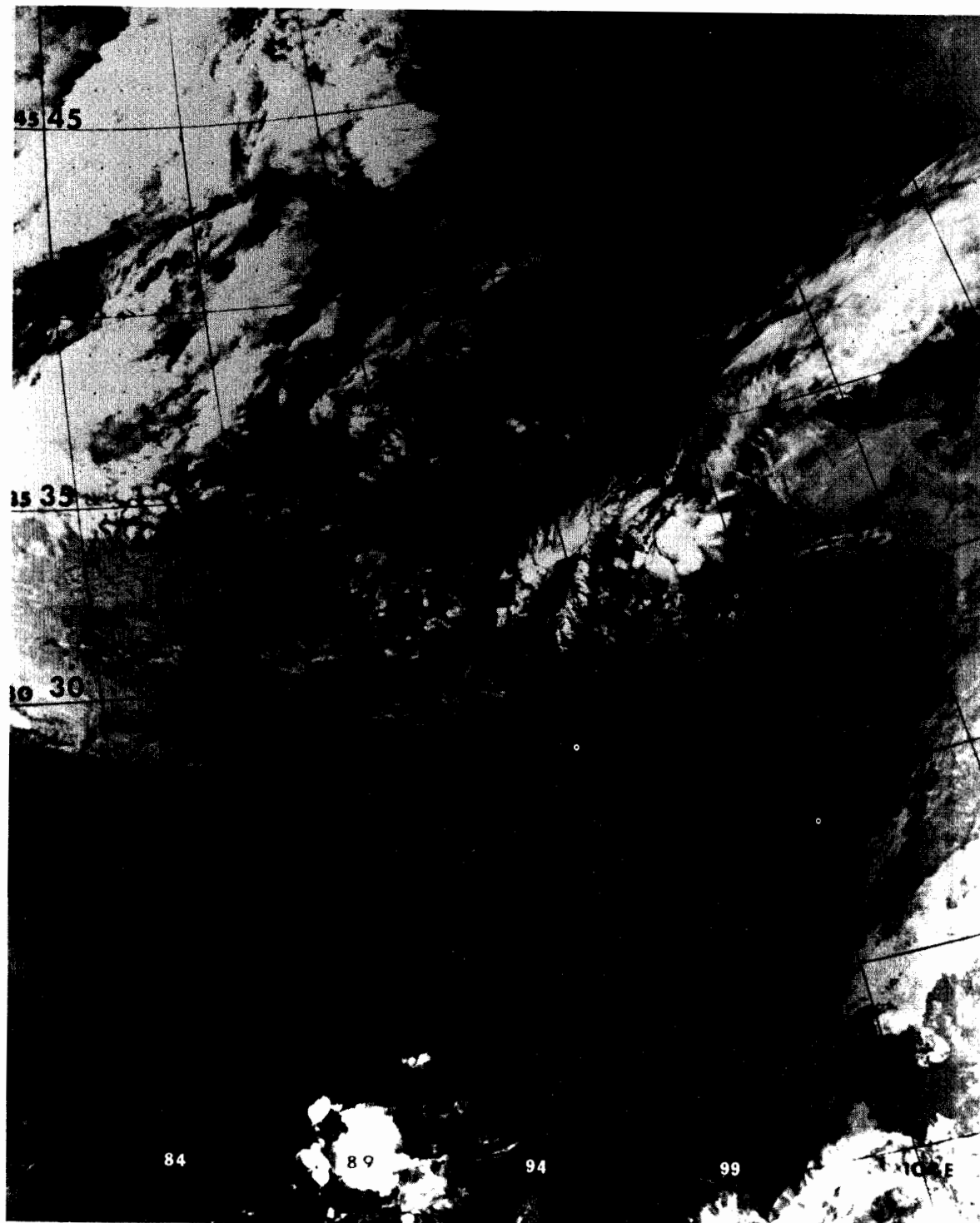Technical Report 74-250   December 1974

Fig 7-4.   WHR/MI comparison.   12 Nov 1972, 6530/490, WHR, Norm, Inv,
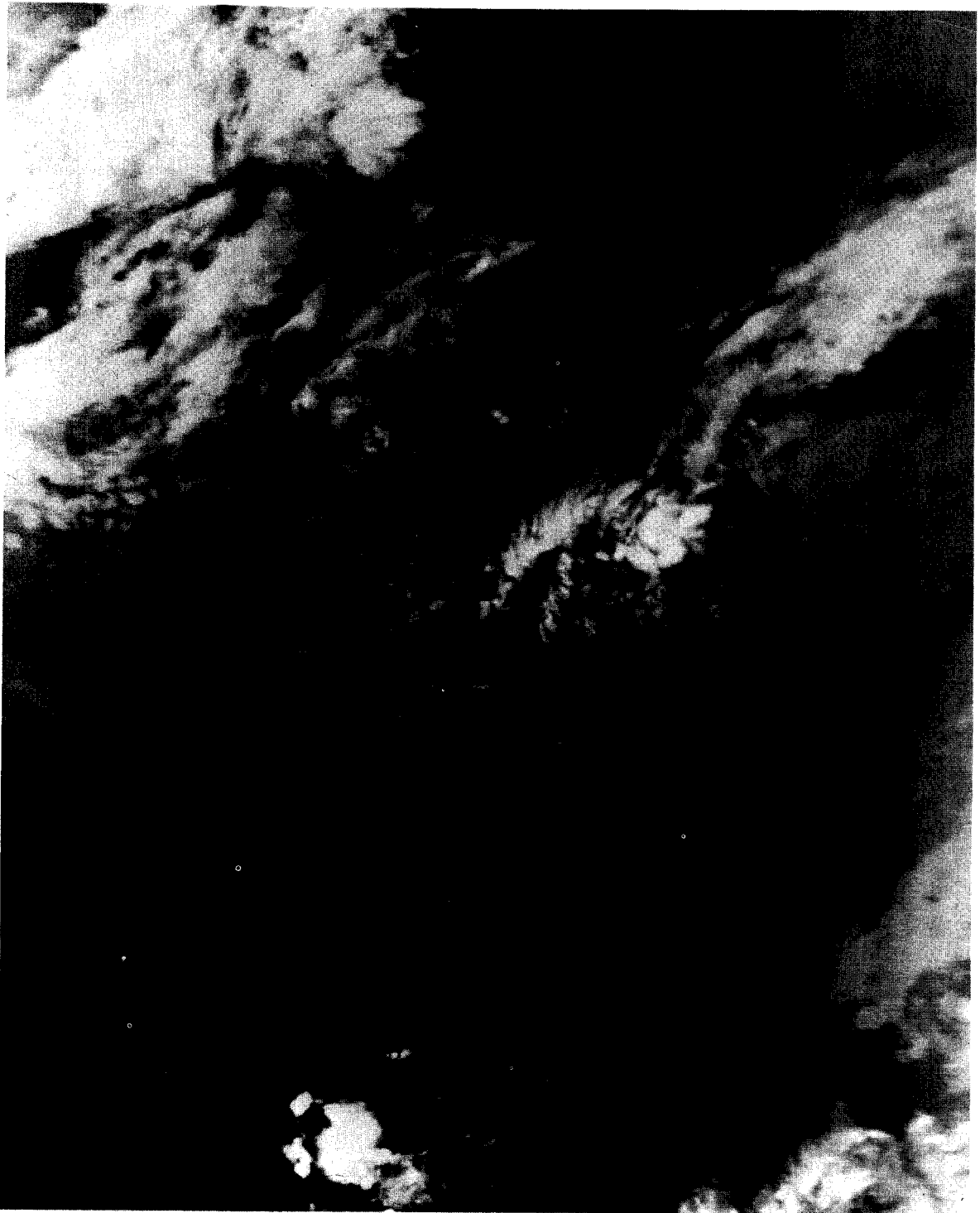310 X1, Off

Fig 7-5.   WHR/MI comparison.   12 Nov 1972, 6530/490, MI, Norm, Inv,
           310 X1, Off

and infrared imagery to determine the intensity of frontal weather. With very high resolution data, mesoscale cloud details within the frontal zone can be used as a basis for short term forecasting. Examples of frontal cloud patterns are shown in Figures 4-5 through 4-19, 7-11 through 7-14, and 7-25.

Fog and stratus are well described in [12]. On page 5-B-1 of that document it states that "it is impossible to distinguish fog from stratus in satellite photographs." This statement remains true for the DMSP system also. Even use of all the enhancements, thermal ranges, and thresholds fails to solve the problem, since the visual appearance of fog and stratus from above is the same, and the effective radiating temperature differences are nil. Frequently we find for fog or stratus over water surfaces that the cloud top temperature is indistinguishable from the water surface temperature in adjacent clear areas. Figures 7-14 through 7-16 contain areas of fog and stratus.

Many types of wave phenomena have been observed and studied within the tropical regions. They are described in the literature as easterly waves, equatorial waves, inverted "V" pattern, and others. The personnel of the Hickam AFB, Hawaii DMSP site have observed a cloud pattern in the trade winds which they have nicknamed a "screaming eagle." (Figure 7-6). They normally observe screaming eagles between 140°W and the date line, and from 10°N to 25°N. This pattern produces widespread cloudiness and precipitation over the Hawaiian Island area. By using thermal ranges and thresholds, the site personnel have discovered that the screaming eagle is similar to a positive vorticity advection (PVA) area, only it exists at a lower altitude (700 mb) than PVAs do in the mid-latitudes. These perturbations are observed to form in the easterly flow north of the intertropical convergence zone, usually between 140°W and the date line. It is rare for an existing screaming eagle to advect into the region. Formation west of 140°W is the usual event.

The composition of a screaming

eagle is a function of latitude. It is made up of cumuli or stratocumuli, having tops less than 8000 feet, and towering cumuli that vary in height with latitude. From 10°N to 15°N the towering cumuli grow up to 20,000 feet or more; from 15°N to 20°N tops reach 15,000 to 20,000 feet. North of 20°N the tops will usually be below 15,000 feet. The screaming eagle resembles a weak easterly wave, usually four degrees of latitude in N-S extent, moving from east to west at the speed and direction of the mean wind between 5000 and 10,000 feet. This is usually near five degrees of longitude per day (13 knots). When the disturbance moves into the Hawaiian Islands, widespread rainshowers occur with cloud bases near 1500 feet. The screaming eagle usually breaks up and does not retain its distinctive appearance after passing through the Islands; however, if it survives passing over the Islands, it will continue westward and not dissipate until near the date line.

Figures 7-7 and 7-8 show a screaming eagle. It can be located in the visual data (Figure 7-7) between 11°N and 15°N and near 150°W (right-hand side of the picture). The screaming eagle pattern shows up better in the coincident infrared data of Figure 7-8, where cirrus blowing off from the tops of the matured cumuli shows the classic shape depicted in Figure 7-6. The Hawaiian Island chain is northwest of this particular screaming eagle, extending from 22°N,160°W to 19°N,155°W.

C. Tropical Cyclones

The DMSP site on Guam has been making operational use of the imagery in supporting the Joint Typhoon Warning Center (JTWC). For several years the JTWC had been making use of Automatic Picture Transmission (APT), Direct Readout Infrared (DRIR), or Direct Readout Scanning Radiometer (DRSR) imagery from NOAA satellites to locate tropical cyclones for aircraft reconnaissance. In 1971 Guam obtained a DMSP readout site and the number of Air Force weather reconnaissance airplanes was significantly reduced in the Pacific. As a result of these actions, much greater use had to be made of meteorological satellite imagery than to just classify the storms according to the rules set down by Fritz, Hubert, and Timchalk [17].
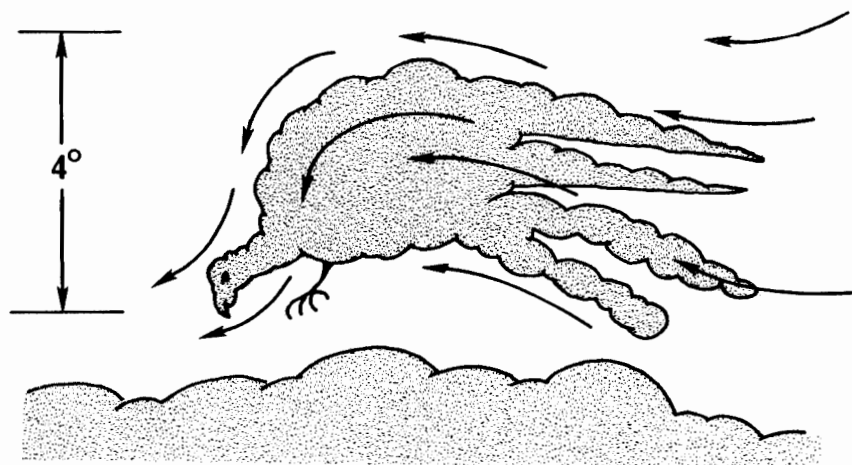
Fig 7-6.   Schematic of screaming eagle.
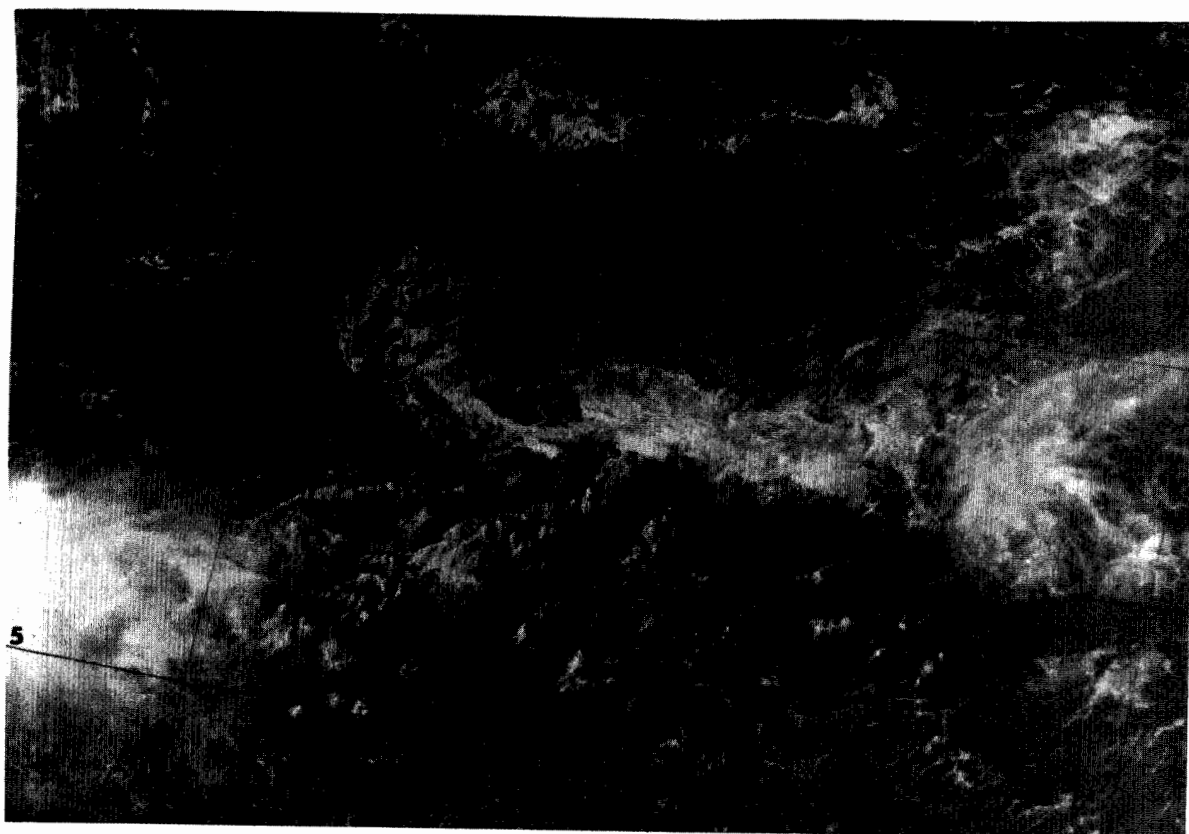
Fig 7-7.   Screaming eagle.   23 Sep 1970, 2525/293, VHR, Norm, Norm, Off.
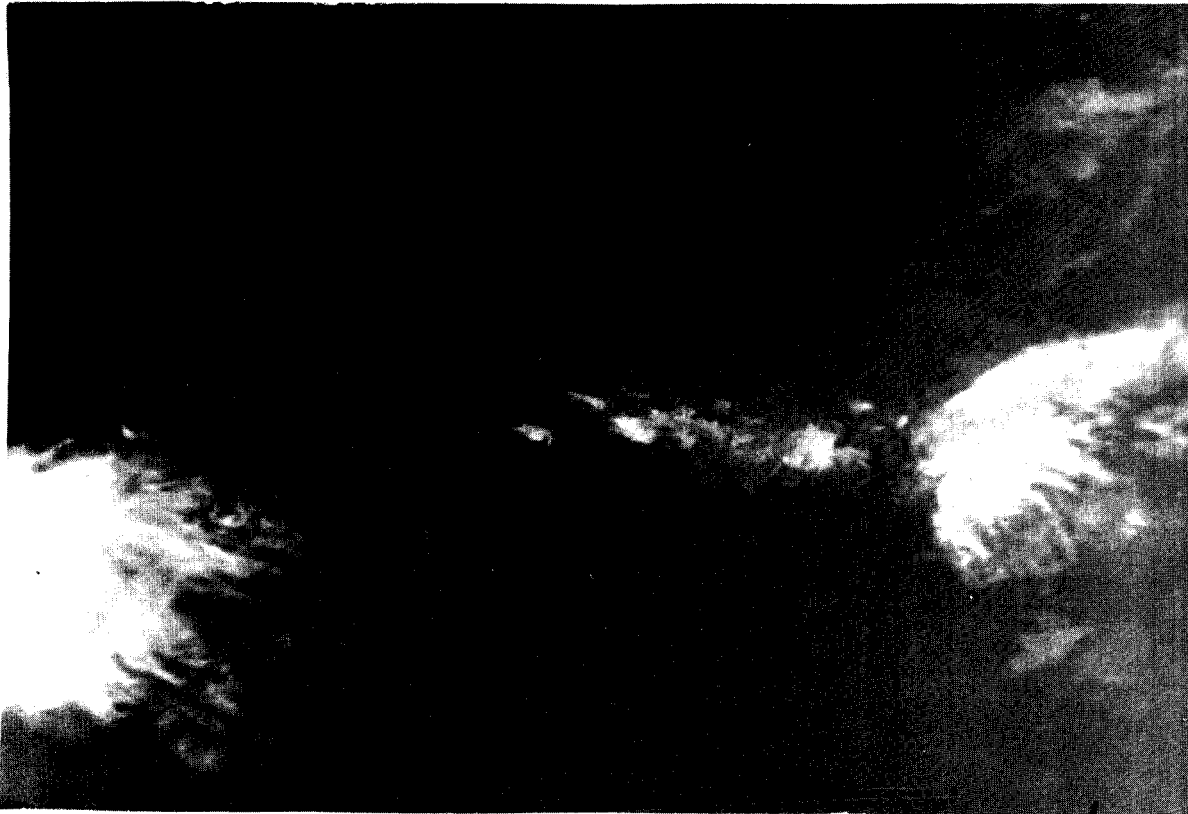
Fig 7-8.   Screaming eagle.   23 Sep 1970, 2525/293, MI, Norm, Inv 310
           X1, Off

        In 1971 the 1 Weather Wing of the
AWS (headquartered at Hickam AFB,
Hawaii and in command of all Central
and Western Pacific AWS units) develop-
ed a new program called the Selective
Reconnaissance Program (SRP). It is
designed to make maximum use of
satellite, radar, and conventional
data to position and determine the
intensity of tropical cyclones.
After testing in 1971, the program
was revised and has been used opera-
tionally since then. In the satellite
portion of SRP, tropical cyclones are
grouped into three main categories:
storms with a visible eye; storms
without an eye, but with a well
defined circulation center; storms
without an eye, but with a poorly
defined circulation center. For a
while the three categories were

further subdivided according to
whether or not suitable geography
for gridding the picture was
visible. This further subdivision
was eliminated when it was found
that the verification statistics
were nearly the same for both
categories. The DMSP imagery is
corrected for cloud height per-
spective error, and gridded as
precisely as possible. If a
center of circulation is apparent
from low clouds within the center
of an open eye, this center is
used to position the storm. A
post analysis of each storm is
performed and the position error
is computed for the best satellite
fix vs the "best track" fix. The
best track positions are computer
calculated using satellite,

December 1974   Technical Report 74-250

aircraft, radar, and synoptic data reports with appropriate weighting factors determined from previous storm seasons. The results of the 1972 Western Pacific tropical cyclone seasons are listed in Table 7-1.

During the spring of 1972, Mr. Vernon F. Dvorak of the National Environmental Satellite Service was invited to spend two weeks at the JTWC, Guam. He was devising a new technique for classifying tropical cyclones based on their appearance in satellite pictures. He worked with

	Mean Deviation (NM)	Sample Size
Visible eye	14.7	157
Well defined circulation center	21.0	139
Poorly defined circulation center	30.2	294
Average	23.9	590

Table 7-1.   1972 Guam DMSP SRP Summary

Guam's SRP efforts plus a few DMSP observations from other Pacific sites were used to cancel weather reconnaissance flights into the storms if the satellite pass was within 1.5 to 3.0 hours prior to the warning time for a descending node, 1.75 to 3.0 hours prior to the warning time for an ascending node, and met the visible eye or well defined circulation center criteria. During 1972 100 of 647 total tropical cyclone fixes were accomplished by satellite fixes (15%). The SRP program, using satellite, radar, and synoptic data, actually accounted for more than that, with 109 center fix flights saved with SRP, and 48 investigative flights saved; a total of 157 aircraft sorties saved. This represented about 20% of the total aircraft levy for the 1972 season. In addition to these levies saved, other SRP fixes (not meeting the three criteria stated above) were used to fill in for inadvertent missed or late aircraft fixes.

The final statistics for the 1973 storm season were not complete at the press time of this Technical Report. However, partial statistics for the first eleven months of 1973 were available. DMSP satellite fixes accounted for 42 of 272 total fixes, or 15% of the total - the same as 1972. The smaller quantity of fixes indicates that the 1973 Pacific storm season was much less active than in 1972. The verification statistics for center fix accuracy compared to best track were nearly the same as 1972.

the originators of the SRP program, and a continuous flow of information and new techniques have continued between Mr. Dvorak and the Guam DMSP personnel. His technique [18] is vital to the SRP program. In 1972, using the Dvorak technique, tropical cyclone wind speeds at the storm center were estimated with an average deviation from best track values of only eight knots. This was the same deviation that aircraft fixes had from best track values. Using the Dvorak technique for making a 24-hour forecast of the intensity of the storm yielded an average 13-knot deviation from verifying best track values. A 10 Jan 1974 message from 1 WW indicated that 1973 verification "results will be very similar to those of 1972."

The details of the SRP and how the Dvorak technique is used in SRP are contained in Arnold [19].

Figures 7-9 and 7-10 show hurricane Agnes as she moved onto the Gulf Coast during 19 June 1972. An earlier view of Agnes in the formative stage can be found in Figures 7-17 and 7-18 for 14 June 1972. The imagery for Figures 7-9 and 7-10 were received by the tactical site located at Keesler AFB, Mississippi. The site was experiencing the storm at the time of data receipt. Reconnaissance reports indicated that Agnes had 75 knots on 18 June, and experienced her lowest pressure on the morning of the 19th with 978 mb. Maximum winds of

Technical Report 74-250   December 1974
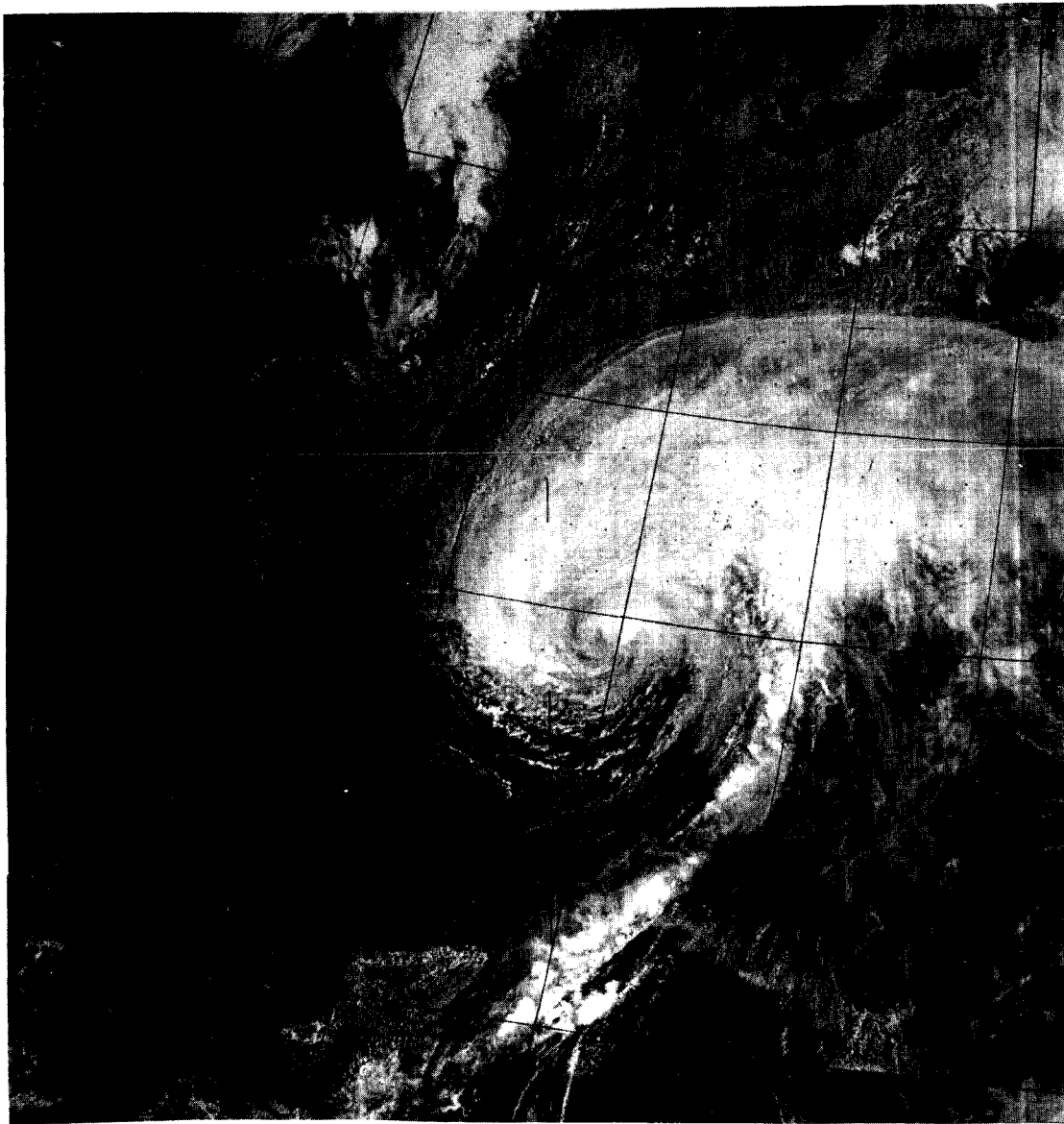
Fig 7-9.   Tropical cyclone Agnes.   19 Jun 1972, 5528/1236, VHR, Norm,
           Norm, Low

65 knots were reported just prior to
land fall. The DMSP imagery was
sensed near noon.

    Two motions are apparent in the
visual imagery of Figure 7-9. The
lines of small cumulus cells over
both water and land indicate the low
level, cyclonic inflow to the storm.
Cirrus plumes, particularly along

the northern edge of the storm, indicate
the upper level, anticyclonic outflow
from the storm. Also apparent are the
quantity of active cumulonimbi along
the feeder band extending southward
from Agnes towards Yucatan, and the
central dense overcast (CDO according
to Dvorak) near the storm center. A
look at the infrared of Figure 7-10
shows considerable difference between
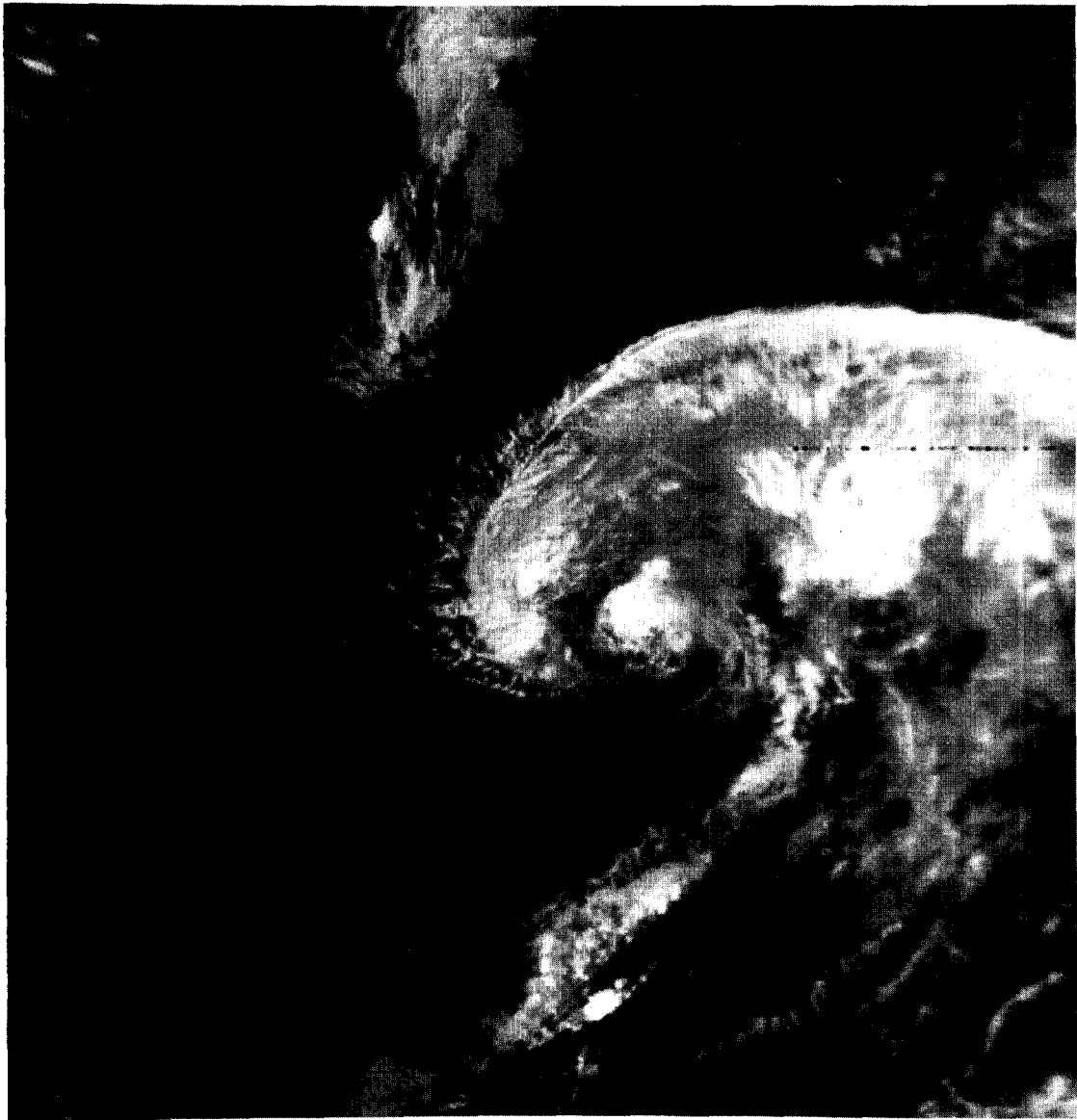
Fig 7-10. Tropical cyclone Agnes. 19 Jun 1972, 5528/1236, MI, Norm, Inv
           310 X1, Off

the details apparent in it when
compared with the visual storm. It
is much more difficult to identify
the apparent center of circulation.
Low level flow as indicated by
cumulus lines virtually disappears.
There appear to be massive quantities
of cirrus, some of which obscure the
low cloud details that could be seen

through patches of thin cirrus in the
visual picture. The combination of
MI sensor spectral interval and 2.4
nm resolution results in the apparent
blooming and fuzzing of infrared
imagery. These figures show why the
SRP program uses visual imagery,
day or night, as the prime data
choice from DMSP imagery. Work

has started in using WHR imagery at night for SRP.

During the summer of 1973 the 53rd Weather Reconnaissance Squadron (Hurricane Hunters) moved to Keesler AFB from Puerto Rico. Even though the Keesler AFB DMSP site is used primarily for maintenance technician and forecaster training, DMSP data are now being used to support the Hurricane Hunter crews in their missions into the storms. Tropical cyclone positions and intensities in the Atlantic Ocean are also being provided to the National Hurricane Forecast Center in Miami by SRP trained forecasters using DMSP data at the AFGWC, Offutt AFB, Nebraska.

D. Mesoscale Patterns Near the Surface

Cumulus streets over land and water clearly showed the low level wind flow into Agnes in Figure 7-9. The same type of cumulus street patterns are present during periods of no tropical cyclone activity. Figure 7-11 shows many small cumulus cloud elements aligned with the low level flow pattern around the western edge of the Bermuda High. The lines are present over both land and ocean. Some enhancement and distortion of the cumulus lines are evident where topographic barriers disturb the wind flow. This is particularly evident over Hispaniola, with downstream effects in the cumulus pattern noticeable south of Cuba. It is also very apparent that the waters of Lake Okeechobee in Florida are cooler than the land. Cumulus cloud lines end abruptly at the south shore of Lake Okeechobee, and do not reform until well down-stream from the Lake's north shore. Similar statements about cumulus lines are made by Oliver and Purdom which reads, "high resolution observa-tions of convective cloud patterns in the tropics reveal that trade wind cumulus and cumulus congestus clouds are not distributed in a random fashion, but occur in well organized, long, and narrow lines." [20]

Maj H. W. Brandli, while assigned to the DMSP site at Hickam AFB, Hawaii, investigated and wrote a paper on "Cumulus Cloud Lines or Streets near the Equator" [21]. During the two year study, nearly 100 cases of

cumulus streets were investigated in the vicinity of Christmas Island (2°N,157.5°W). The weather observing site on Christmas Island is on the upwind side of the Island during tradewind conditions. These conditions prevail most of the year, and there are no topographic features to disturb the trades in the short distance they travel from the sea to the observing site. The study showed that when cumulus streets were present: 1) 100% of the time the wind speed was between 5 and 18 knots. 2) 100% of the time the tradewinds were occurring (e. g., the wind directions were between 050° and 160°. 3) 80% of the wind directions favored the zone between 090° and 110°. 4) The wind directions maintained the same angular direction as the cumulus streets. 5) 100% of the time the wind directions were within 20° of the cloud streets. 6) 20% of the time the wind direction paralleled the cloud street. 7) The average wind direction was 10° more northerly of the cumulus street orientation (e. g., a cumulus street oriented east to west would have a corresponding surface wind from 080°. Only the small cumuli elements were used in this study. Coincident infrared data showed that the tops of the cumuli were below 8000 feet.

A later, but similar, study was performed by Capt Wells at the Guam DMSP site [22]. He concluded that the small cumulus tracer clouds possessed a directional orientation representative of the gradient-level flow. Radiosonde winds from Western Pacific Island stations were used to specify the low level winds, and he found that the cloud tracers appear to be embedded in the layer from 2000 to 4000 feet. The layer demonstrated little or no directional shear; however, vertical speed shear was present. He hypothesized that vertical speed shear is the mechanism for the elongation of the small cumuli patterns. The only cumulus clouds considered representative of the flow pattern were those just visible in the 1/3 nm visual imagery.

Gust fronts and frontal ropes are shown in Figures 7-12 and 7-13. Examples of gust fronts are located near 13°N,105°W from three cumulo-nimbus clusters, 20°N,94°W from three more cumulonimbus clusters, and 12°N,
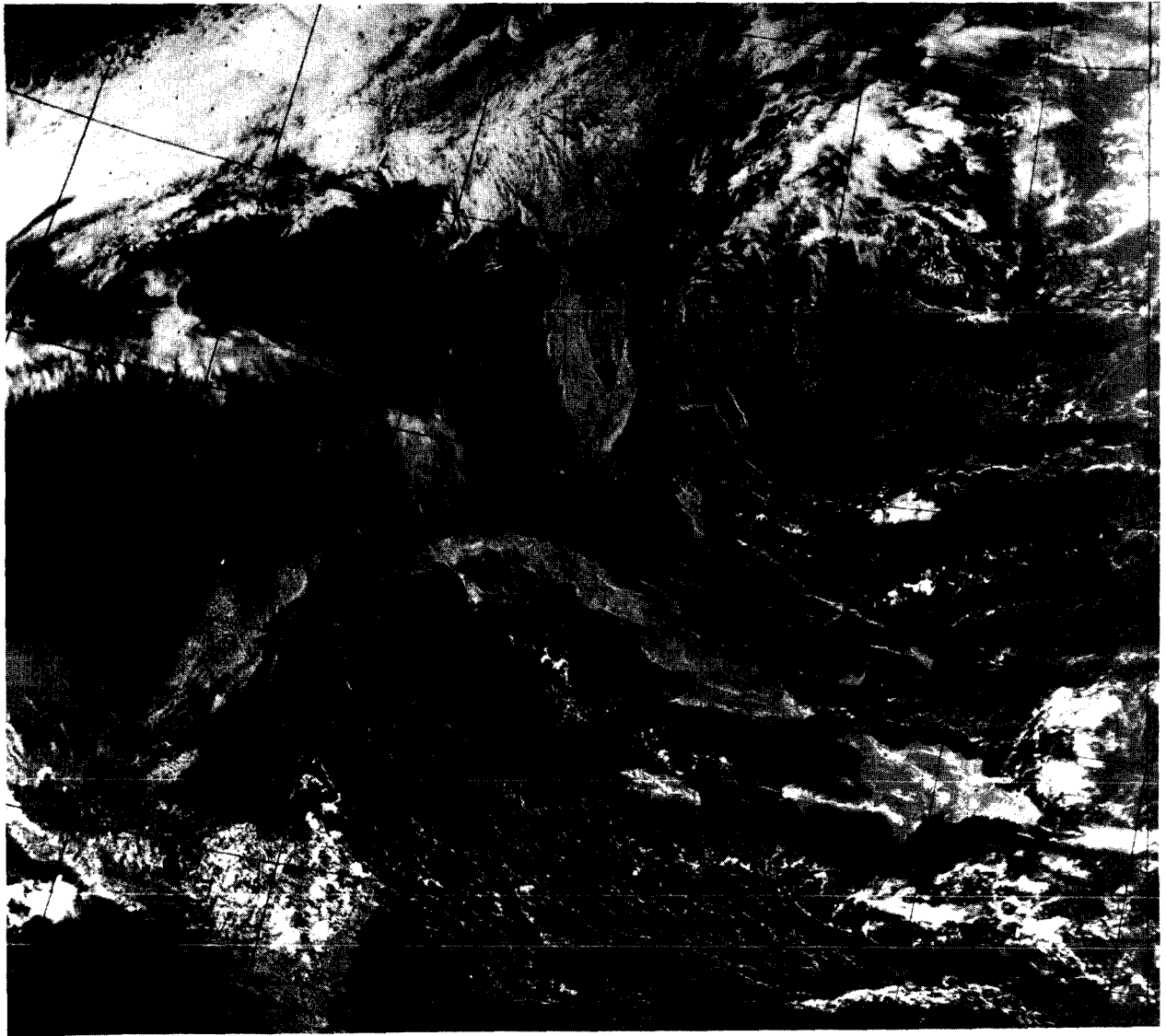
Fig 7-11. Cumulus Streets. 14 Jun 1973, 5528/5026, VHR, Norm, Norm, Off.

91°W from the cumulonimbus clusters. A glance at the infrared data of Figure 7-13 shows that the gust front cloud areas do not have great vertical development. Oliver and Purdom [20] describe these cloud features as arc-shaped lines of cumulus and cumulus congestus clouds found along the leading edge of a thunderstorm's rain-cooled air. Purdom [23] goes into further detail on the gust fronts, and describes them as the boundaries of mesoscale high pressure systems (bubble highs). He further shows that most new thunderstorms will form along the meso-high boundary.

In Figure 7-12 a frontal rope is visible from near 22°N, 95°W northeastward to 29°N, 88°W. Oliver and
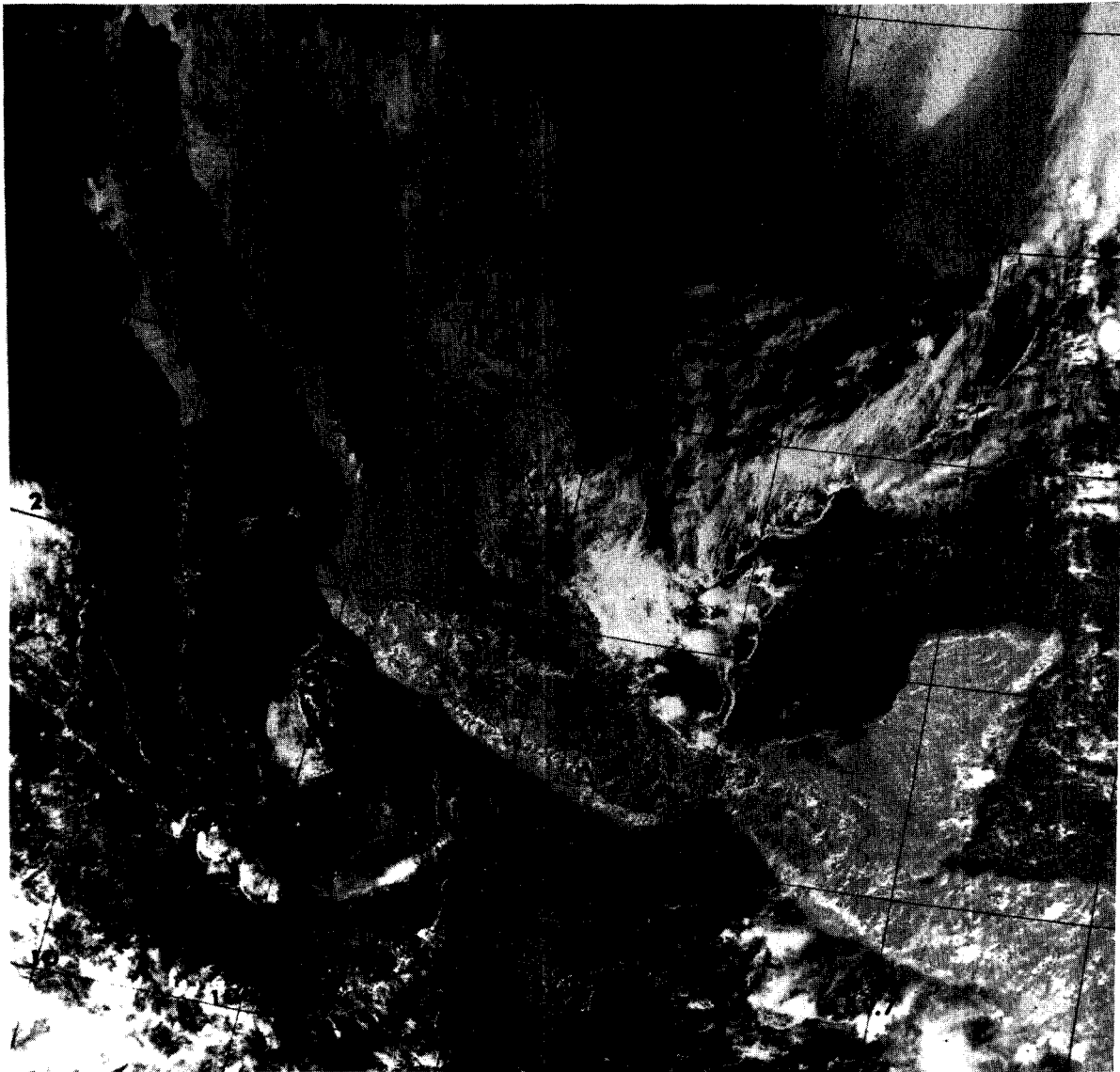
Fig 7-12. Gust fronts and frontal ropes. 9 Oct 1970, 2525/518, VHR,
           Norm, Norm, Low

Purdom [20] imply that a frontal rope is made up of many gust fronts, intersecting each other, and that the small arcs of the frontal rope are along the leading edge of rain-cooled air produced by showers. The existence of gust fronts and frontal ropes has been seen occasionally in satellite imagery for years; however, with the advent of very high resolution data, their existence has been found much more frequently and their role in thunderstorm generation has become apparent.

Cloud lines predominate in the Gulf of Mexico in Figure 7-14 (This figure is a photographic enlargement
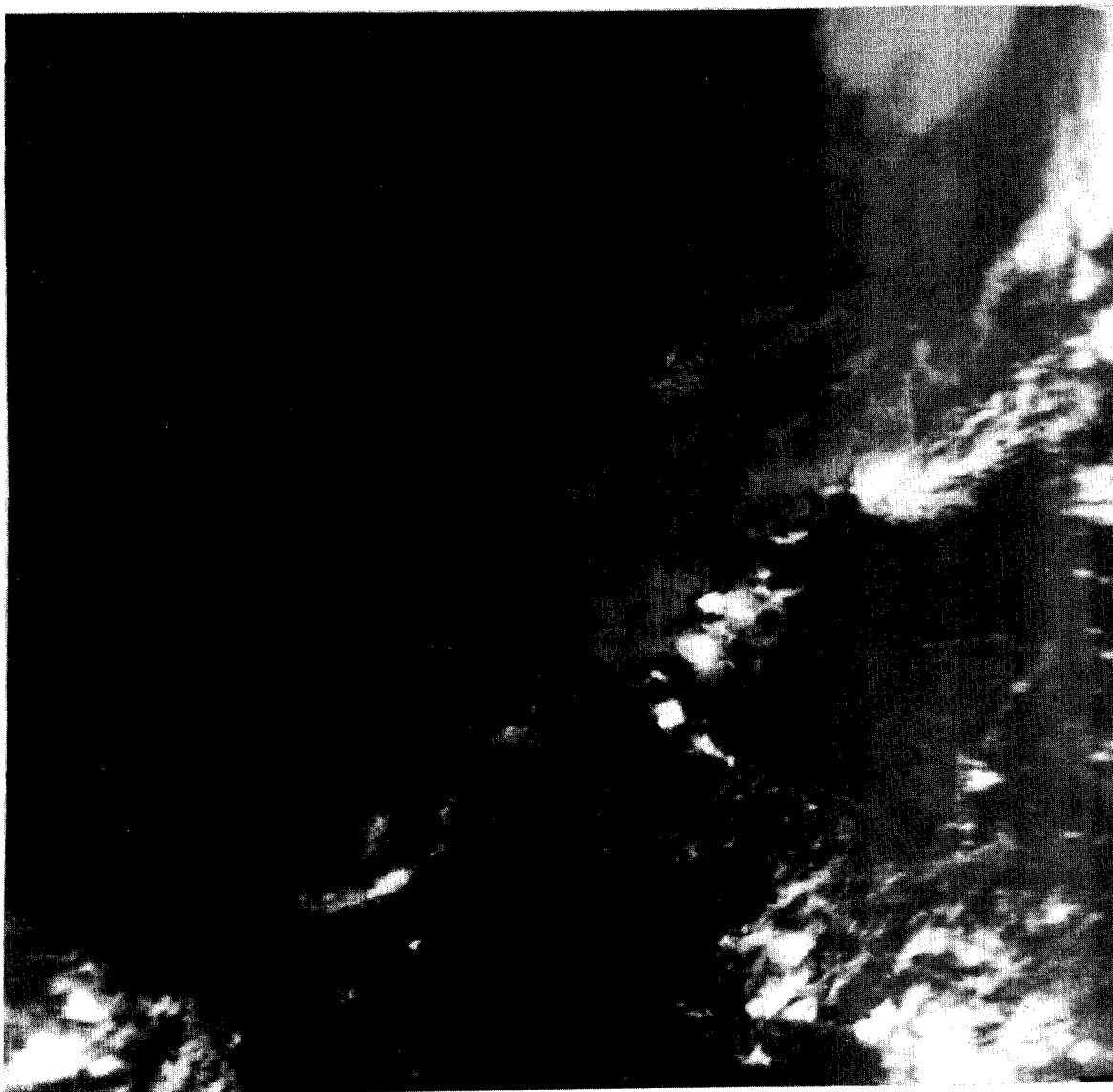
Fig 7-13. Gust fronts and frontal ropes. 9 Oct 1970, 2525/518, Norm,
Inv 310 Xl, Off.

of a portion of Figure 6-4 that was
used to illustrate proper gridding).
The synoptic process causing this
cloud pattern is the advection of
cool, dry air from land over the
Gulf following a cold front. The
frontal cloud band is in the south-
eastern portion of Figure 7-14. There
exists a considerable temperature and

moisture gradient between the water
surface and the lower layers of the
atmosphere. Large quantitites of
heat and moisture are transferred
from the water to the air as the air
flows equatorward. When adequate
amounts have been transferred, con-
densation occurs in the shallow, un-
stable layer of air. Small cumuli
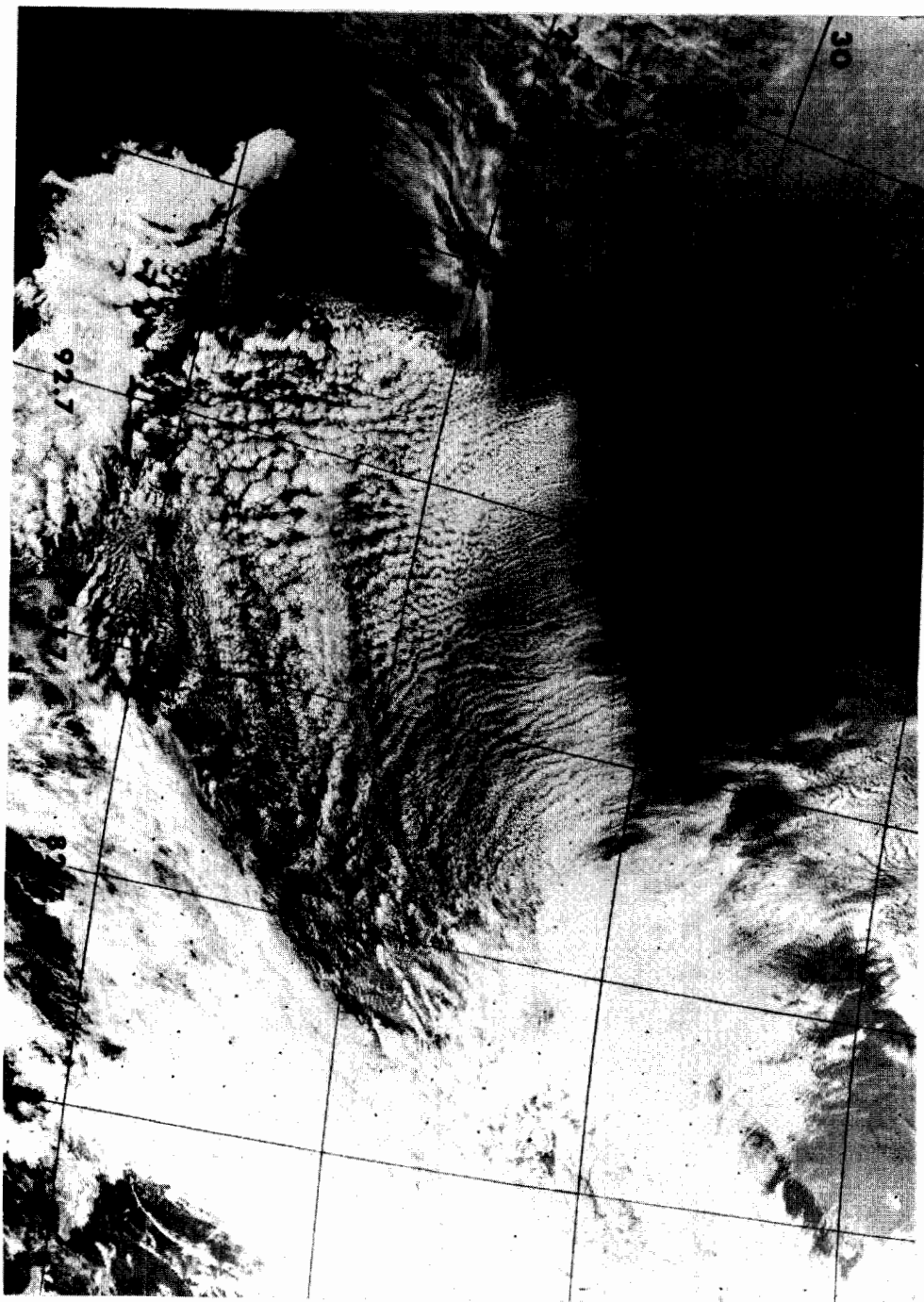
Fig 7-14. Cloud lines. 29 Jan 1973, 5528/4404, VHR, Norm, Norm, Off.

December 1974   Technical Report 74-250

form, continue to grow downstream as more heat and moisture are added to the air, and the distinctive cloud line pattern develops. AWS Technical Report 212 [11] defines a cloud line as "a line composed of a series of clouds nearly all of which are connected and which is less than 1 degree latitude in width." Parmenter [24] comments that the downwind cloud edge basically conforms to the shape of the exit land mass except for lines formed due to heating by upwind cities and advection over warmer bay or lake waters.

A glance at Figure 7-14 shows that the small cumulus elements grow to larger elements, predominantly stratocumulus. Where advected over Mexico, a sheet of stratus and strato-cumuli covers the terrain up to a certain altitude. The western and southern edge of the clouds in Mexico are terrain contoured. The use of

very high resolution imagery allows the forecaster improved accuracy in observing the formation point of the small cumulus elements, and patterns which sometimes occur within the mass of cloud lines.

Another line of clouds found in satellite imagery is the anomalous line. An example is shown in Figure 7-15 which contains numerous lines off shore from California. Conover [25] published the first accounts of satellite observed anomalous lines. He described them as occurring most often in the summer months, and always over water. The lines are always low level and usually are found in the eastern and southern sides of highs. Exceptions have been found behind cold fronts and in the subsiding sectors of a vortex. Surface wind speeds range from calm to 10m/sec. Five possible causes of anomalous lines were listed: a) aircraft condensation

Fig 7-15.   Anomalous lines.   4 Aug 1971, 3526/2404, HR, Norm, Norm, Low

Fig 7-16.   Actiniform clouds. 29 May 73; 5528/6102,
            VHR, Norm, Norm, Off

trails, b) missile trails, c) smoke screens from ships, d) convection induced by certain temperature patterns in the sea, and e) the effluents from ships. In a later publication, Conover [26] reports an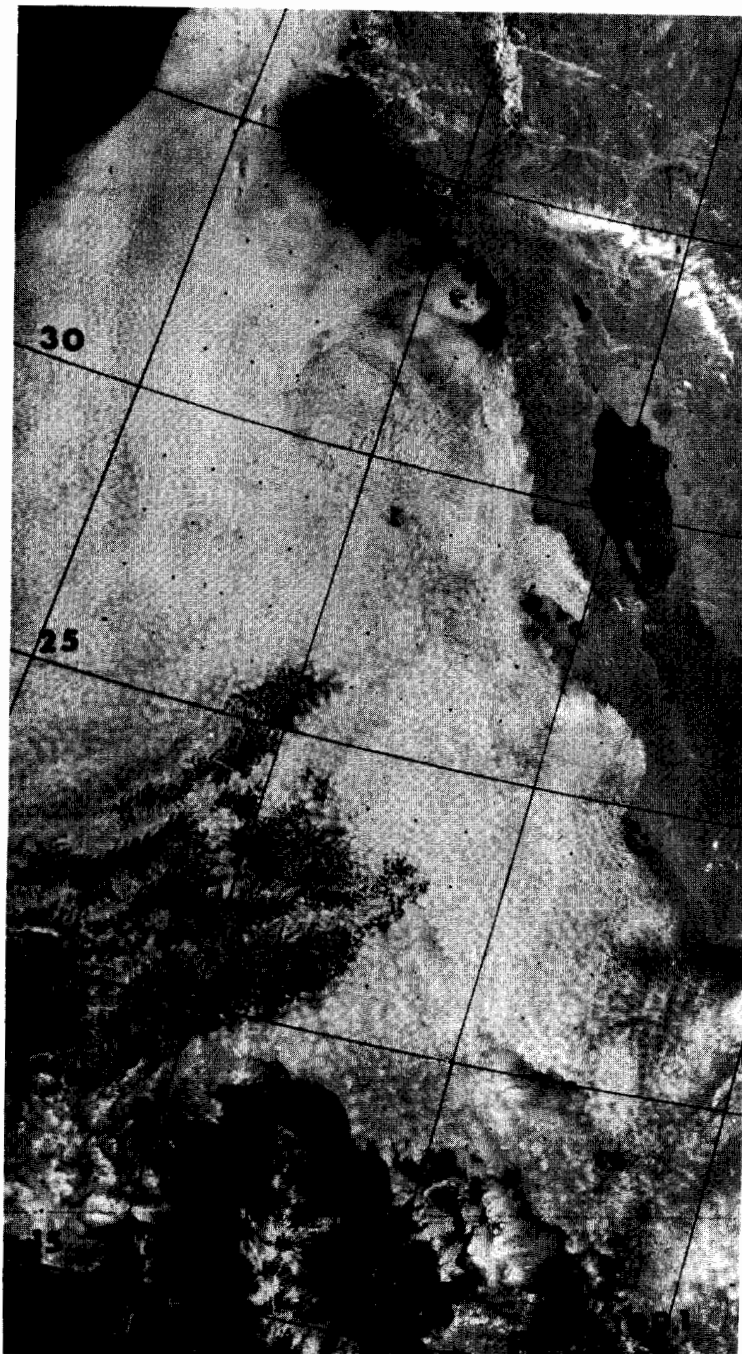 eyewitness observation by Capt McGill, pilot of a weather reconnaissance aircraft, who saw a ship physically forming a cloud trail. On that flight he crossed another cloud trail, noted the location, and later saw the anomalous cloud pattern on satellite imagery for the same time and location. We may conclude that ships are the most likely cause of anomalous cloud lines, [27].

Most anomalous lines do not have a high albedo. Using DMSP data with variable enhancements or VHR Inv mode processing allows the structure of the anomalous lines to be clearly observed. Further investigation of this phenomenon is planned.

Another unique cloud pattern generally found in oceanic regions dominated by high pressure is the actiniform shown in Figure 7-16 west of Mexico near 21°N, 119°W. AWS Technical Report 212 [11] describes the pattern as a possible transition phase between open and closed cells. The pattern is most commonly seen off the west coast of South America.

Faintly visible near 28.5°N, 116.5°W is an eddy pattern in the stratocumulus, formed by the flow of air (cloud) past Guadalupe Island. Eddies are frequently seen in the stratocumulus clouds downwind from Guadalupe Island. Normally they take a spiral-like pattern; however, they have also been observed in a V-pattern (bow wave). For examples see Figures II.5.17 and II.5.20 in [13].

E. Cumulonimbus Patterns

The high enhancement mode of displaying VHR or HR data has been used to bring out the details in high albedo subjects. Figure 4-7 is a good example of this. Figure 7-17 is an example of a mass of highly reflective clouds displayed in the normal (off) mode. It shows tropical cyclone Agnes on its first day of named existence. The main cloud mass is located east of Yucatan (vicinity of 21°N, 85°E).

The storm exhibits very poor organization even though weather reconnaissance aircraft observed maximum winds of 40 knots. Agnes is shown five days later as a well developed storm in Figures 7-9 and 7-10. Within the cloud-blob in Figure 7-17 we know there must be penetrative cumulonimbus clouds. These clouds are masked by the high reflectivity of the dense cirrus clouds covering most of the area. Since Figure 7-17 is imagery using the normal (linear) distribution of gray shades it is difficult to see the cumulonimbi. A better portrayal of the visual imagery would be to use the high enhance mode. Another way to make penetrative convection more perceptible is to display infrared data in the 235K - 210K range using the X4 expand mode. This works well if the entire cirrus cloud mass is not colder than 210K.

A newer and better method is the VHR Inv mode described in Section 5E. The application of this display for cumulonimbus patterns is illustrated in Figure 7-18, which is a VHR Inv of (the 1:7.5 million expansion of) the left hand half of Figure 7-17. In this example an equivalent temperature setting of 290K was chosen. This represents a threshold albedo of 73.1%, compared with a maximum displayable albedo of 91.4%. This narrow range of albedoes results in only the brightest clouds being displayed, with each gray shade representing an albedo range of roughly 1.43%. Since the visual imagery is inverted, the darkest clouds in Figure 7-18 represent those with the highest albedo (whitest) in Figure 7-17. The penetrative cumulonimbus clouds are now clearly outlined. The "hot towers" can easily be located and even counted.

F. Wave Clouds in the Upper Atmosphere.

Wave clouds associated with strong winds aloft can occur either as billow clouds (not associated with terrain) or as lee waves. Both types are observed in DMSP imagery. An example of billow clouds over the Gulf of Mexico is shown in Figure 7-19. An extensive area of billow clouds exists north of Cuba. That area is magnified in Figure 7-20.

The relationship between winds
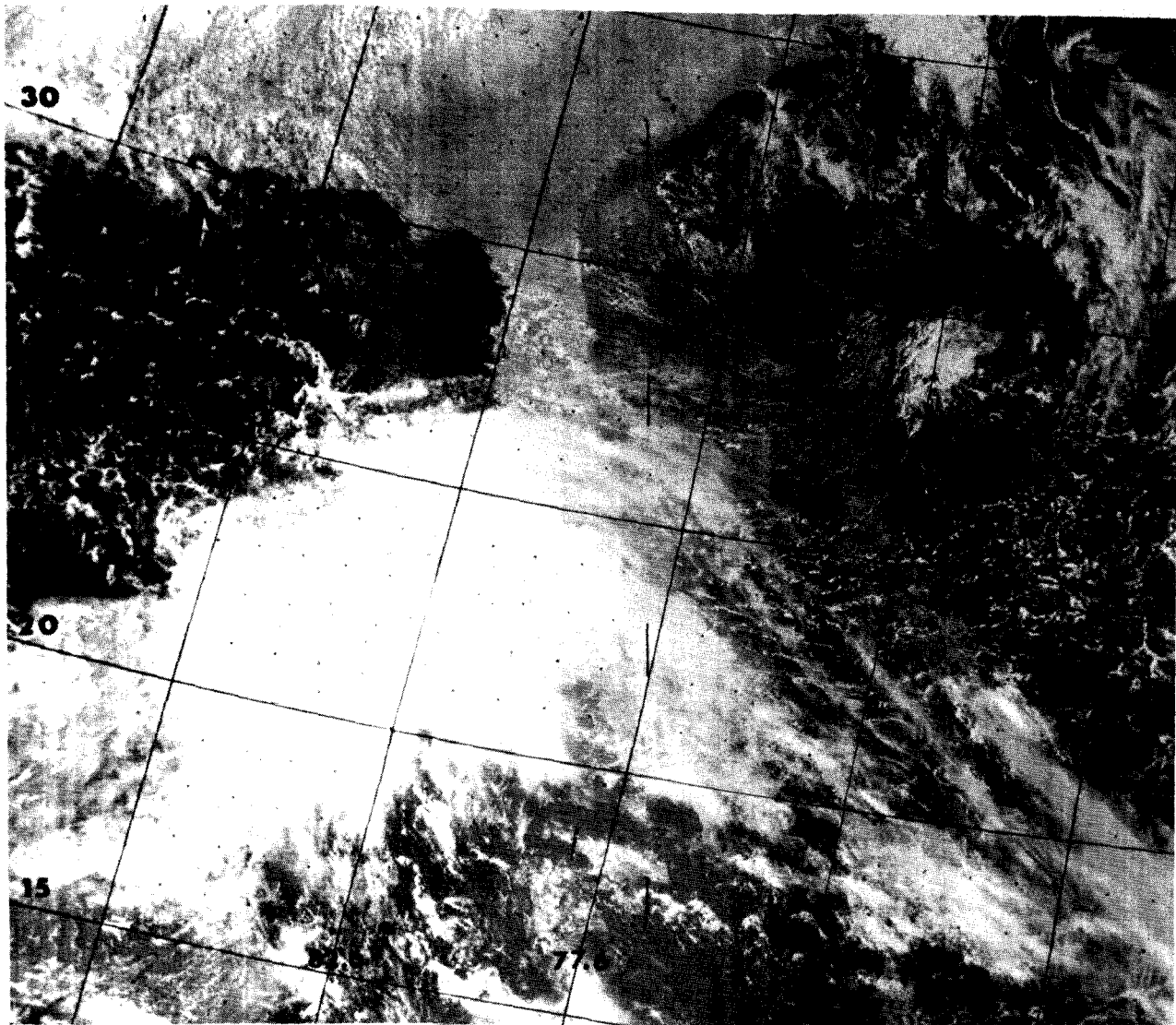
Fig 7-17. Penetrative CB's. 14 Jun 1972, 5528/1165, VHR, Norm, Norm, Off.

aloft and billow phenomena observed at the Hickam AFB DMSP site was studied by Brandli and Lombardo in 1970 [28]. (Their study was subsequently presented at the 1973 spring meeting of the American Geophysical Union [29].) Wind reports were obtained from Hilo, Hawaii rawinsonde data when billows were near there, and from aircraft directed to the billow locations. It was found that the wind direction was normal to the wave cloud lines. Wind speed, using only the spacing between consecutive cloud lines, was found to be given by:

Wind speed = $16.43 + 18.42\lambda$ (Eq 7-1)

where wind speed is in knots, λ is wave length in nautical miles. The linear correlation coefficient of wind speed vs wave length is 0.91. A multiple regression equation of wind

Fig 7-18.   Penetrative CB's. 14 Jun 1972, 5528/1165, VHR, Exp L., Inv,
            290 X4, Off.

speed as a function of temperature and wave length was also computed. It is:

$$\text{Wind speed} = 0.08\ T_{cld} + 19.51\lambda$$

(Eq 7-2)

where wind speed is in knots, λ is the wave length in nautical miles,

and T_{cld} is the cloud top temperature determined from MI data with the atmospheric attenuation corrections included for moisture (Figure 5-4) and scan angle (Figure 5-7). Figure 5-8 can be used in place of Figure 5-4 if a standard atmosphere assumption is used. The correlation coefficient of wind speed as a function of temperature and wave length is 0.996.
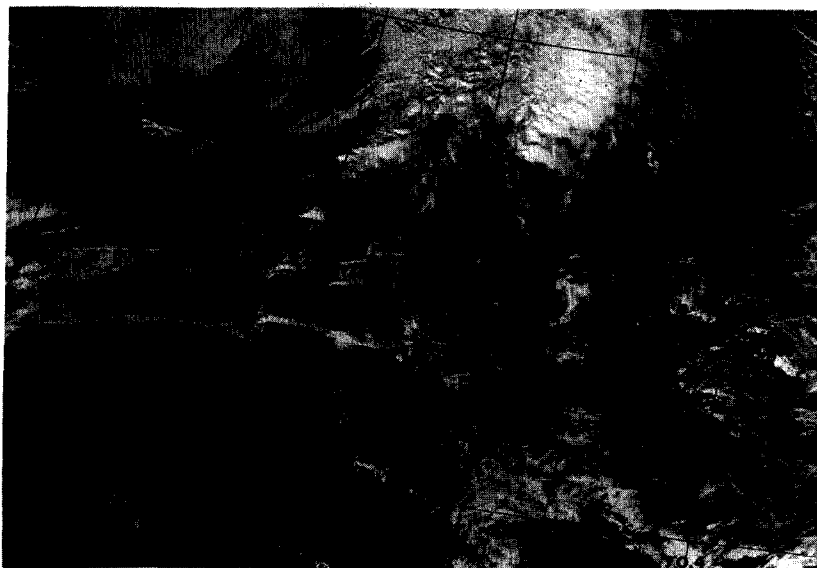
Fig 7-19. Billow clouds. 14 Feb 1973, 5528/4650,
           VHR, Norm, Norm, Off.

The 25 cases yielded the follow-ing results:

1) The average speed difference between calculated and ground truth was 6.4 knots. The greatest dif-ference was 27 knots, and the small-est was zero.

2) The average wind direction difference was 4.6 degrees. 92% of the cases were ten degrees or less, and 72% were five degrees or less.

In 1972 Boselly [30] noticed a case of billow clouds over the Gulf of Mexico, south of the Keesler DMSP site, that were aligned parallel to the wind flow. In an article referred to by Reiter [32], Sekera found that "gravity waves in the region of strong vertical wind shears are oriented
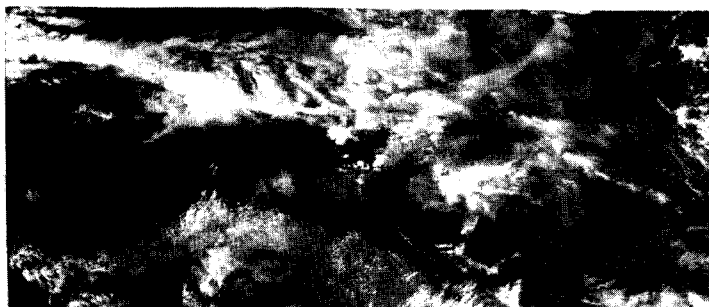
Fig 7-20. Billow clouds. 14 Feb 1973, 5528/4650,
           VHR, Exp C, Norm, Off.

in bands parallel to the wind direc-
tion; with weak shears, however, they
lie normal to the wind direction."
[31]   On 14 February 1973 (imagery
unavailable for publication), Boselly
observed another set of longitudinal
billow clouds that allowed him to
test Sekera's statement. The billow
clouds were south of Eglin AFB,
Florida. An analysis of MI data
showed billow cloud tops to be at
32,000 feet. Radiosonde data from
Eglin showed moisture up to 32,000
feet, and vertical wind shear averag-
ing 15 knots per 1000 feet from
33,000 to 35,000 feet. This strong
shear was immediately above the long-
itudinal billow clouds; thus, though
this case is not conclusive evidence,
it verifies the thesis that longitu-
dinal billow clouds are the result
of gravity waves oriented in the
direction of wind flow with strong
vertical shear.

Reiter [32] states ... "one would
have to expect therefore that in an
area of weak vertical wind shear,
flights conducted parallel to the jet
axis would experience more turbulence
than flights oriented normal to the
wind direction ... with strong
vertical wind shear one should expect
turbulence mainly during flights
normal to the jet axis." Using this,
the existence of billows in DMSP
imagery allows the forecaster to
predict turbulence for aircraft and
inform the pilot how best to pene-
trate the area.

DMSP sites have observed that
billow clouds are much more numer-
ous in imagery from the morning
satellite than imagery from the noon
satellite. This may be related to
solar heating partially destabliz-
ing the layers that the gravity waves
occur in. A final observation is
that transverse billows are much more
common than longitudinal billows.

Examples of orographically
induces wave clouds will not be
shown here. These are discussed in
AWS Technical Report 212 [11, 12],
which includes a graph showing the
variation of mean wind speed with
observed wavelength.

G.   Other Phenomena

Snow cover is commonly observed
by meteorological satellites. Prob-
ably the easiest snow characteris-
tic to observe is the change in snow

cover over a period of time. An
example of this can be observed by
comparing Figure 7-21 with Figure
7-22. It is not easy to find a day
that is mostly clear over the Western
United States; however, on 4 April
1973 there was such a day. This was
near the time of maximum snow accumu
lation. Two months later (5 June
1973) we again have the same view
of the Western United States, this
time with most of the snow melted
away. The light area near 32.9°N,
106.4°W is White Sands, New Mexico.
Most of the snow remaining on 5 June
lies southeast through northeast of
the Great Salt Lake and along the
California – Nevada border. Some
spots of snow remain on the volcanic
peaks of the Cascade Range in the
Northwest. Snow comparisons, such as
these, can be a great aid to hydrol-
ogists. While not shown in this
Technical Report, the use of infra-
red thresholding and VHR Inv can
help quantify snow pack quantity and
aid in flood forecasting/water manage-
ment. One problem is finding clear
days in order to see snow; however,
with two spacecraft, every area in
the world is covered at least four
times daily. That fact, plus the
low light, moonlight capability,
usually insures a visual view of any
area every few days. Although more
difficult to interpret, snow areas
usually are detectable in infrared
imagery.

Figure 7-23 is an example of
icepack, snow covered terrain, and
some clouds near the North Pole.
The poles are viewed on every pass
of the satellite. The location of
large ice leads is important to
resupply ships and fishing fleets.
Iceberg location is important for
main shipping lanes. Note how clouds
are differentiated by highlights on
their sun-facing edges, and shadows
on opposite edges. Infrared views
of a mixed cloud and ice scene are
difficult to interpret due to the
emissive temperatures being so close.
However, infrared views of ice and
water usually show good contrast; and
where there are patches of ice cover-
ing the water, the integrated emis-
sive temperature can be used to esti-
mate the percent of coverage of the
ice. If only visual HR data are
available, then a reverse polarity
can help sharpen the picture's
contrasts to the viewer's eyes.

Figure 7-24 is a view of the
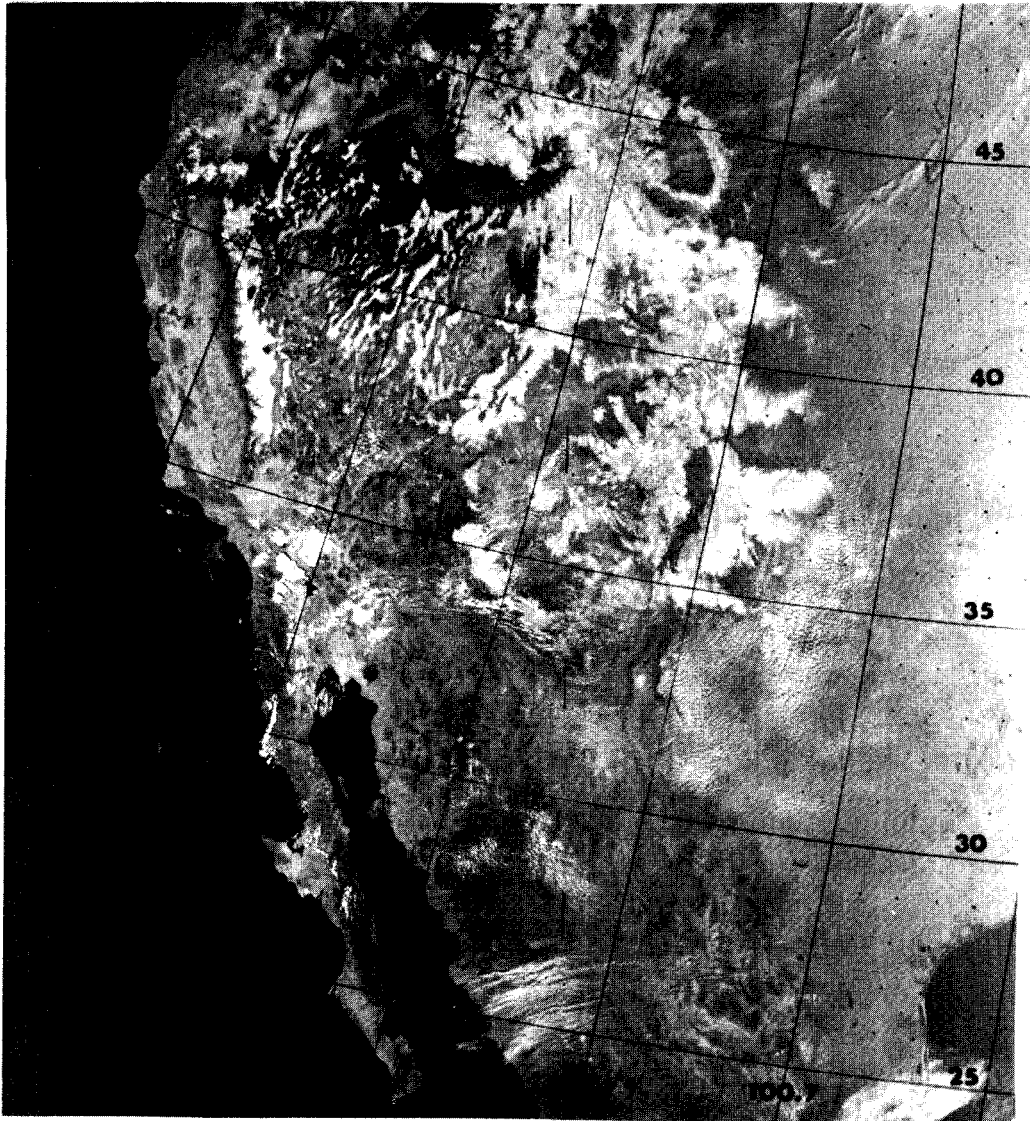
Fig 7-21. Snow. 4 Apr 1973, 5528/5327, VHR, Norm, Norm, Low.

Mississippi River during its record floods during the Spring of 1973. This VHR Inv picture shows clouds black and water white. As a result, the flood plains of the Mississippi and its tributaries show up lighter than the land outside the plain. Close analysis of a series of pictures like this can reveal the general state or trend of soil saturation of bare land. As seasons progress and crops go through their cycles, a general land-use inventory can be maintained. It is possible that DMSP imagery, with its frequent views of terrain, can provide the gap filling continuity imagery that is needed by the users of Earth Resources Technology Satellite (ERTS) imagery. ERTS imagery has considerably better spatial resolution; however, its pictures are limited to 100 nm swaths that repeat only every 18 days.

Figures 7-25 and 7-26 are coincident visual and infrared views of the Gulf of Mexico region. A band of convective clouds stretches from near the tip of Yucatan to the 30°N

December 1974   Technical Report 74-250
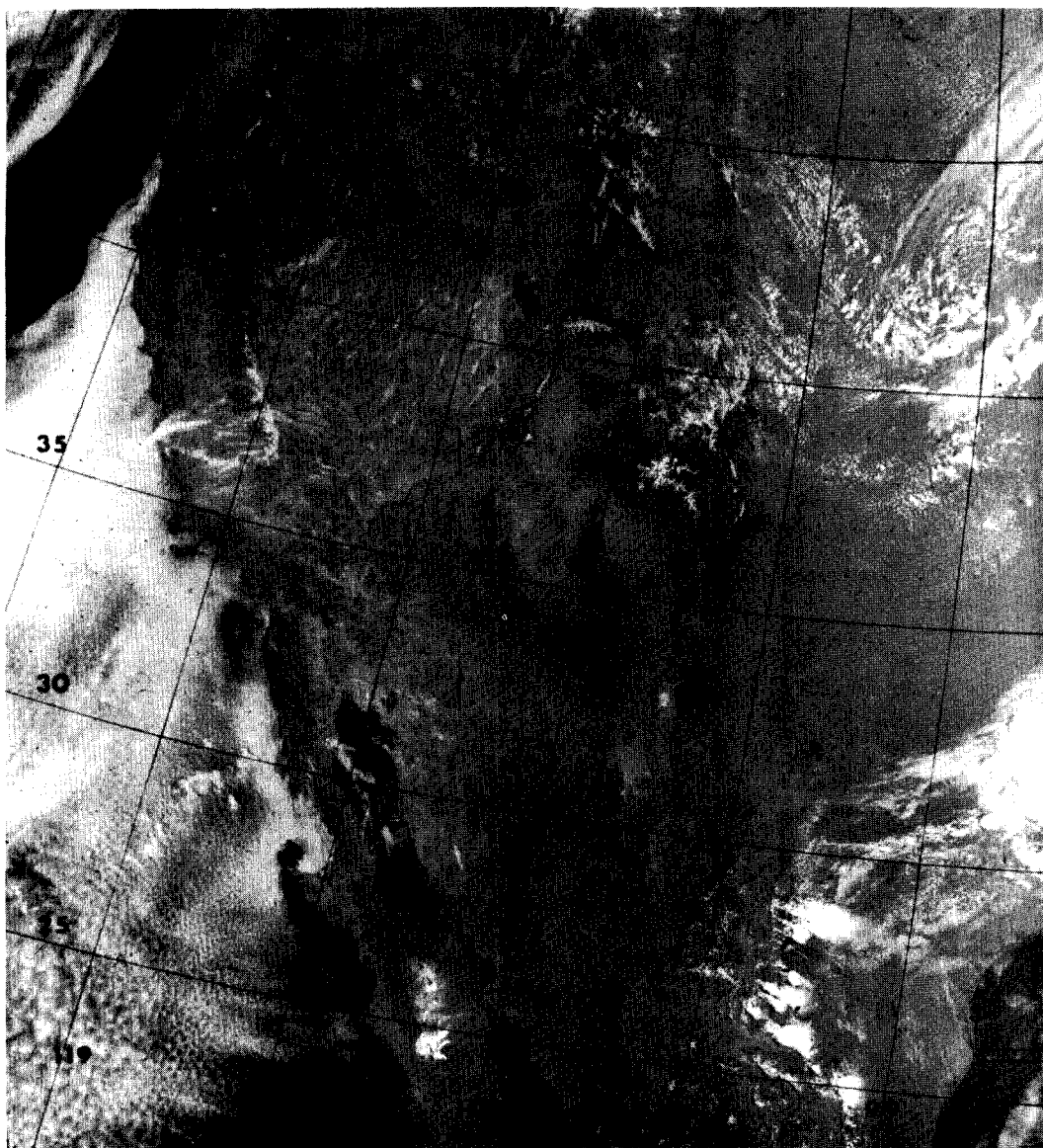
Fig 7-22. Snow. 5 Jun 1973, 5528/6201, VHR, Norm, Norm, Off.

label. One bright spot appears near 21-22°N and 83-84°W in Figure 7-25 There is no trace of it in Figure 7-26. This is a good example of a sun glint caused by the sun's rays reflecting from a water surface to the spacecraft sensor. Another good example can be found near 25°N, 110°W

of Figure 7-22. Besides sun glint from water and marsh surfaces, DMSP has observed sun glint from snow, moon glint from water and snow, and aurora glint from snow/ice.

An interesting and perplexing phenomenon in DMSP visual data is
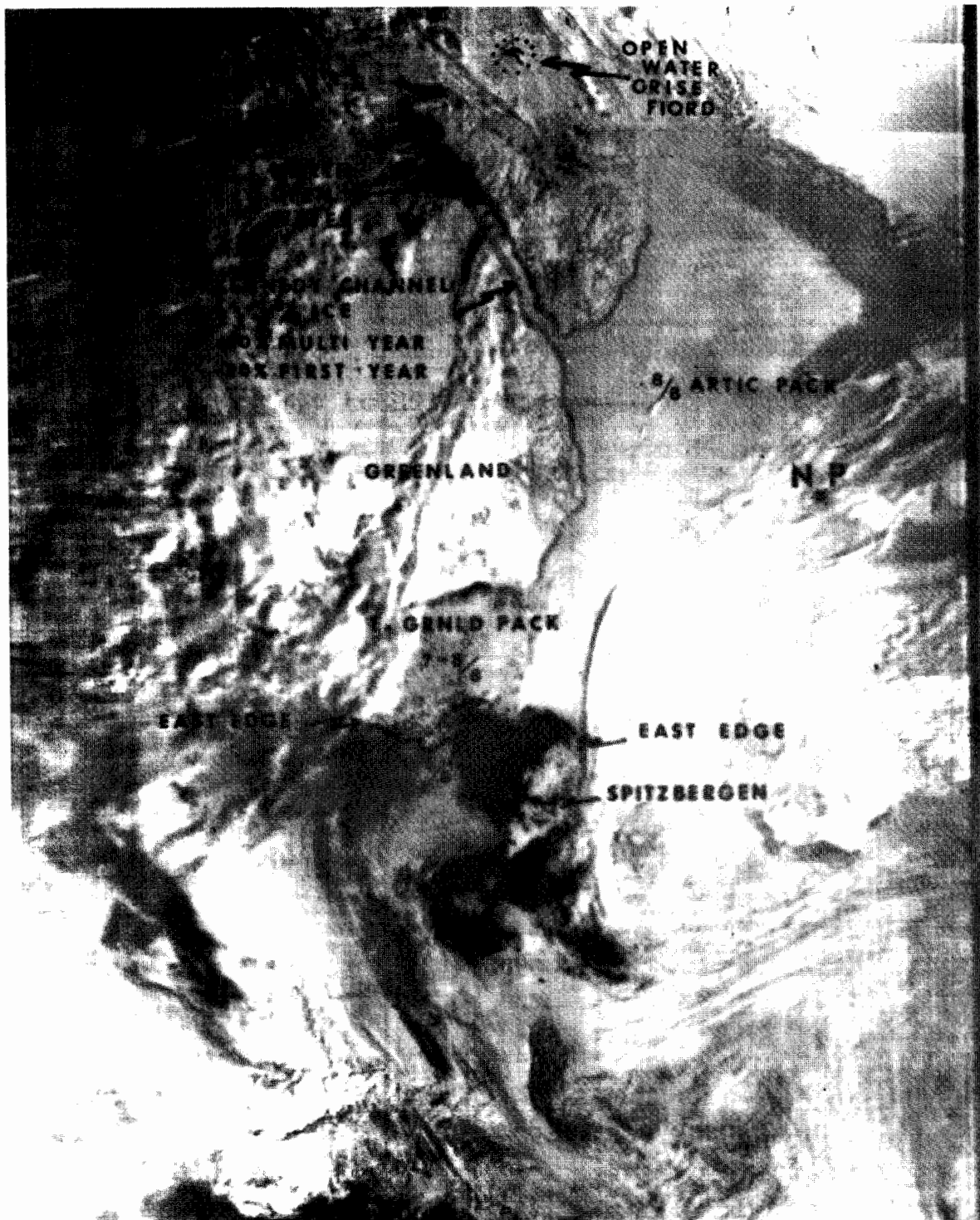
Fig 7-23. Ice. 4 Jun 1971, 3526/1527, HR, Norm, Norm, Off.

December 1974   Technical Report 74-250
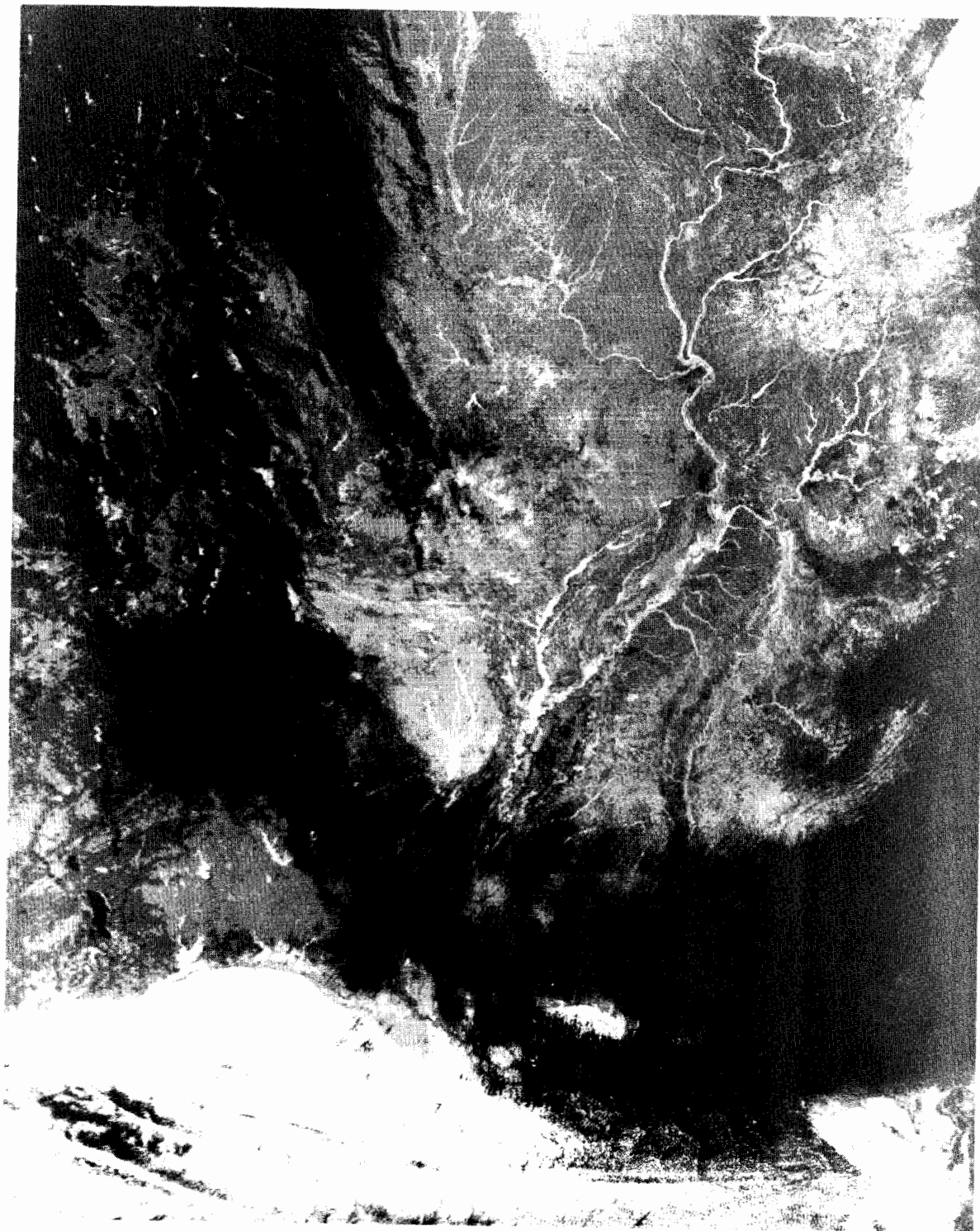
Fig 7-24.   Flood.   21 Mar 1973, 5528/5125, VHR, Exp L. Inv (temperature
            unknown), Off.

Technical Report 74-250

December 1974

the anomalous gray shade pattern that frequently occurs, generally over water. Figure 7-27 shows an anomalous gray shade pattern (lighter shades) extending from western Florida to Louisiana. In Figure 7-28 the left half of Figure 7-27 is expanded and processed as a VHR Inv with equivalent temperature base of 225K. In this X4 mode the albedo range displayed extends from 0% (lightest shade) to 13.7% (darkest shade). All objects brighter than 13.7% are displayed as the darkest shade.

We do not know the full explanation for anomalous gray shades. They

can occur due to a number of reasons which are: 1) shoaling (seeing bottom topography through shallow water, 2) water surface reflectivity changes, 3) thin cirrus, 4) clouds smaller than sensor's spatial resolution, 5) water contamination such as oil, foam, silt, and other debris, 6) aerosols, 7) atmospheric scattering, and 8) water vapor absorption.

Shoaling is a cause of gray shade contouring in DMSP imagery; however, anomalous gray shades have been observed in mid-ocean as well as near continental shelves. The example
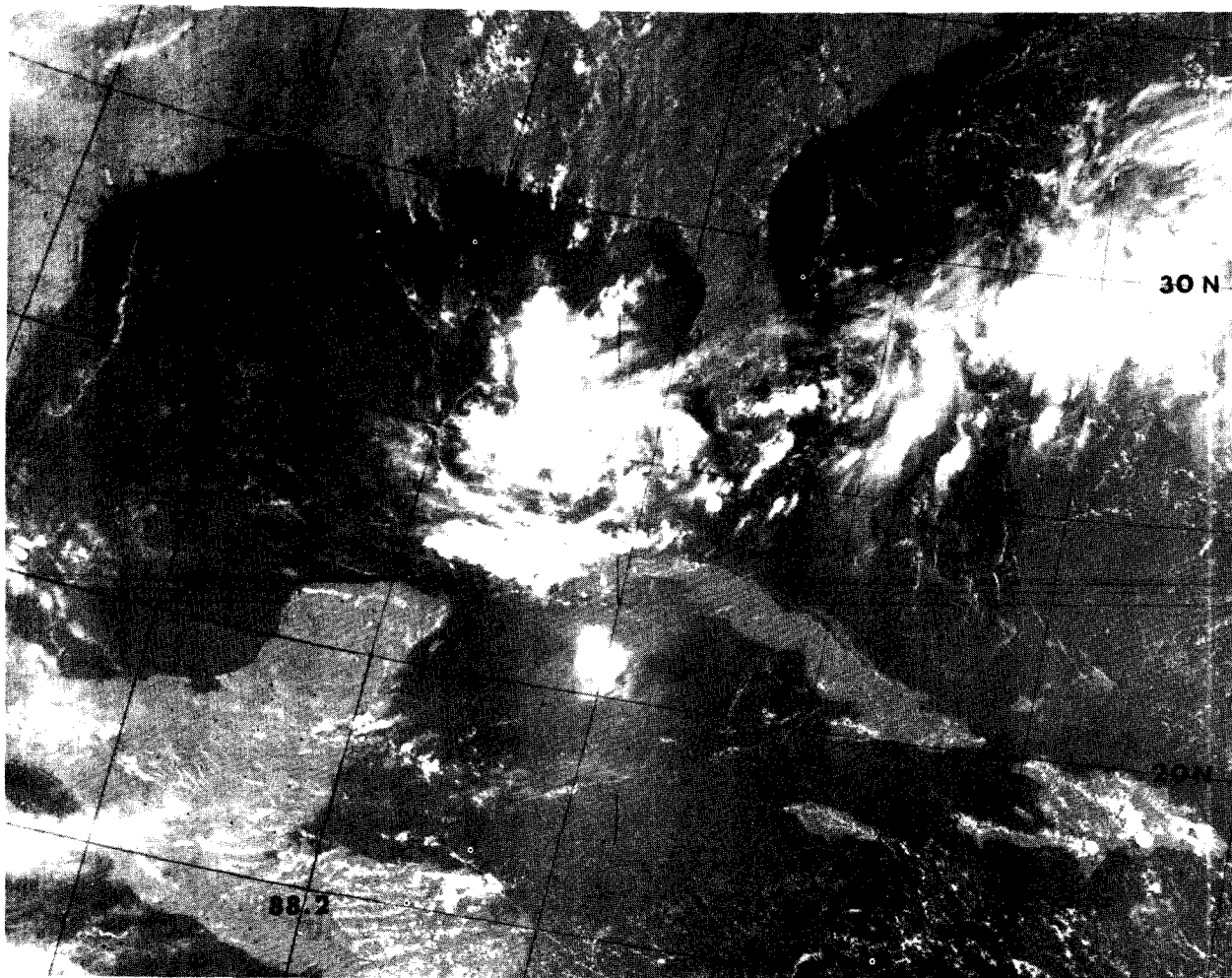
Fig 7-25.   Sun glint.   10 Jul 1973, 5528/6681, VHR, Norm, Norm, Off.
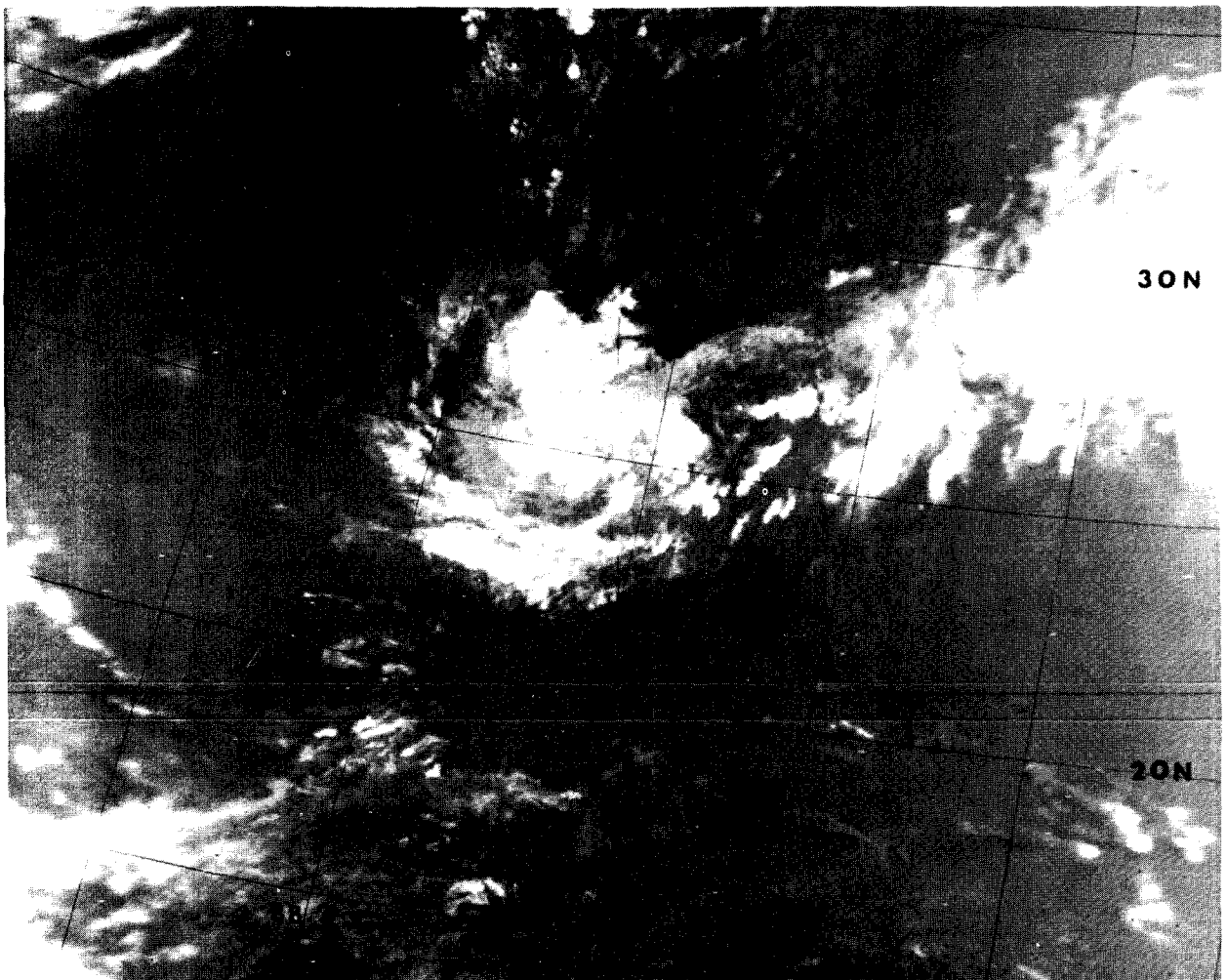
Fig 7-26. Sun glint. 10 Jul 1973, 5528/6681, MI, Norm, Inv 310 Xl, Off.

shown in Figure 7-28 does not conform to bottom contours.

    Water surface reflectivity differences would result from wave size and spacing. This possibility is illustrated by the different appearing sun glints described in [11]. However, we have not noticed any strong correlations between wave size and location of anomalous gray shades. This subject is undergoing further investigation by the Navy's Environmental Prediction Research Facility.

    Thin cirrus could show up as a lightening of gray shades in the midst

of a uniform background (ocean). However, thin cirrus is detected by the infrared sensors, and anomalous gray shades are not detected in the infrared.

    Clouds smaller than the sensor's spatial resolution cause a lightening in gray shades. Probably, this is a cause of some anomalous gray shade pattern. It appears plausible in Figures 7-27 and 7-28 that many small cloud elements could exist between Florida and Louisiana as a trailing portion of the cold front off the East Coast. It is doubtful that small cloud elements are the
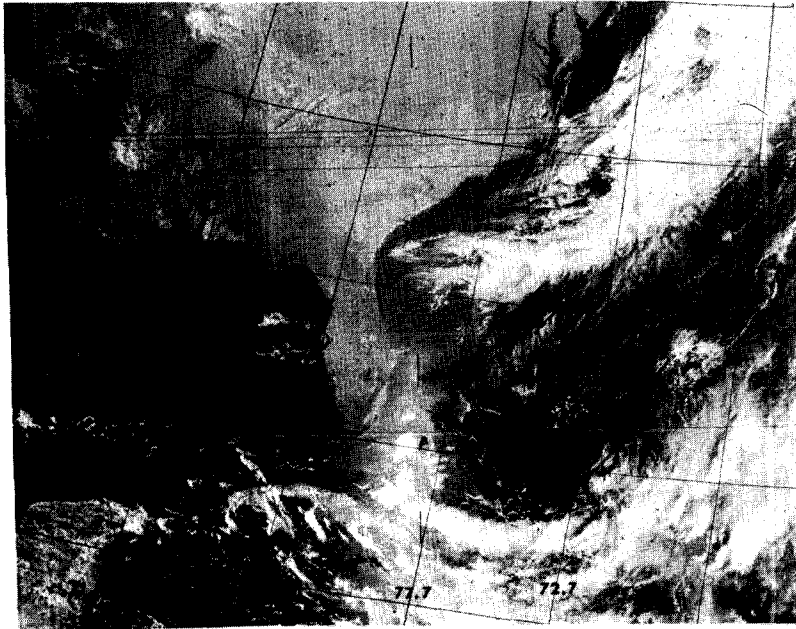
Fig 7-27.   Anomalous gray shades.   7 Jun 1972,
            5528/1066, VHR, Norm, Norm, Low.

major cause of this, or most, anomalous gray shades. A basis for this statement is the fact that VHR and HR data have been compared for anomalous gray shades. Even though the spatial resolution of the VHR sensor is 36 times better than the HR sensor and can detect far smaller clouds, the anomalous gray shade patterns maintain the same size and shading distributions on the two kinds of visual imagery.

Water contamination or water color does show up in DMSP imagery. We suspect that many anomalous gray shades are caused by this effect. Based on conversations with Mr. R. Fett, Environmental Prediction Research Facility, Project Gamefish Skylab (1973) confirms this statement. As part of this experiment, coincident Skylab photography of the Gulf Coast region with DMSP, fishing boat observers, and aircraft showed that water coloration patterns were reflected in DMSP imagery, and from those patterns, the presence of gamefish could be predicted.

Aerosols such as haze, dust, and salt could be a partial cause of anomalous gray shades, but no proof exists. Dust patterns usually cover a far larger area than anomalous gray shades do.

Atmospheric scattering, such as from the smaller haze particles, may contribute to anomalous gray shades; however, maximum scattering occurs in the blue end of the visual spectrum. This is where the DMSP visual sensors' responses are quite low.

Water vapor absorption is significant for three wavelengths in the visual sensors spectral ranges. Three absorption spikes occur near 0.72 μm, 0.81 μm, and 0.94 μm. In the 0.94 μm absorption band atmospheric transmittance is reduced to near 47% for a thickness of one air mass, and to 22% for a thickness of two air masses. An increase in water vapor content in the atmosphere can reduce the amount of reflected radiation from the atmosphere. This is particularly true for the spacecraft sensor, for solar
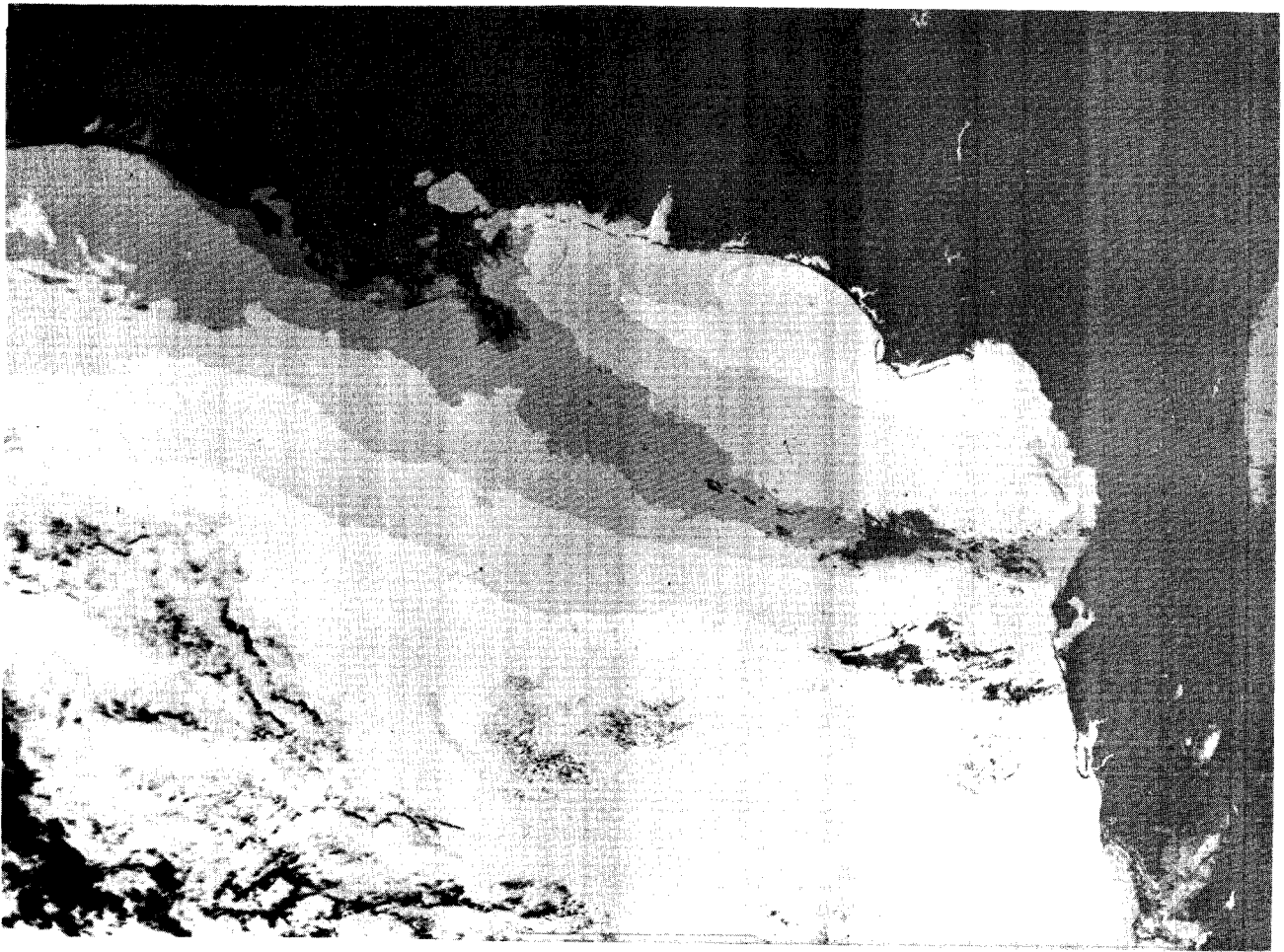
Fig 7-28. Anomalous gray shades. 7 Jun 1972, 5528/1066, VHR, Exp L,
           Inv 225 X4, Off.

radiation, penetrating the atmosphere, is attenuated by moisture. The radiation that reaches the surface is then reflected, and further attenuated by the water vapor on its way to the sensor. As a result, a decrease in atmospheric water vapor content will allow more light to be reflected to the sensor, resulting in a brighter area on these data. An increase in water vapor would result in less reflection and darker imagery; thus anomalous gray shade areas (lighter) should indicate drier atmospheric zones. Naturally, this explanation does not fit logically with the clouds below sensor resolu-

tion explanation, unless the air is abnormally dry above the small cloud elements. As a result, the water vapor absorption explanation for anomalous gray shades appears rather doubtful.

Another reason could include the fact that digitizing the visual signal for tactical site direct read-out may introduce a fictitious anomalous gray shade pattern into the imagery. However, coincident analog data received at AFGWC usually show the same anomalous gray shades. Probably, many of the causes listed here have a bearing on anomalous

Technical Report   74-250

December 1974

gray shades. The dominant cause has yet to be selected.

The low light capability of the HR sensor allows the nighttime observation of lights from the earth's surface, lightning, and aurora. Figure 4-11 is an example of city

lights from Western Europe. Lights from many cities and towns outline the Baltic Sea. England's cities light up most of the Island. Some auroral activity can be seen in the northwest corner of the figure. There was very little moonlight when this picture was taken. As a result,

Fig 7-29. Aurora. 22 Nov 1971, 4527/562, HR, Norm, Norm, Off.

clouds cannot be seen; however, some of the city lights appear blurred and cover a larger area than they do on a clear night. Clouds may be inferred when city lights have a diffused appearance. The amount of areal growth is related to the cloud's optical depth and its altitude.

Infrared imagery is often difficult to grid geographically. A procedure often followed, when precise gridding is necessary, is to process both nighttime HR and infrared data so that their scales are the same. The HR data is gridded first, using city lights as landmarks. Then the infrared data is overlaid on the precisely gridded HR data and the grid lines fit both types of imagery.

Figure 7-29 shows the same general area of Figure 4-11, only three days later. The auroral display is particularly brilliant in this example. The brightest portions of the aurora have saturated the high gain state of the HR sensor. A recent improvement in the gain control of HR sensors now allows the signal to be displayed in a logrithmic fashion so that bright aurora do not wipe-out faint, nearby aurora. This type of imagery can be computer rectified to a geomagnetic coordination system and compared with SSJ or SSJ/2 precipitating electron counts, associated with aurora.

The bright lights of oil drilling operations or refineries show clearly on DMSP low light, HR, imagery. Since they are so bright, oversaturation of the sensor frequently occurs, causing a dark line to appear adjacent to the bright light source. This distinctive characteristic identifies the brightest light sources at night. While no example of oil flares are shown in this Technical Report, a similar phenomenon caused by a volcano is shown in Figure 7-30.

Major Brandli and the site personnel at Hickam AFB, Hawaii commonly saw the city lights of Honolulu in nighttime HR imagery. On 20 September 1970 they suddenly noticed a new light source southeast of Honolulu [6]. The big island of Hawaii had never appeared like this before, so site personnel checked with the University of Hawaii to see

if a lava flow had begun from one of the active volcanoes there. The reply at first was no; however, new lava flows were subsequently confirmed. Throughout October and November the lava flow was observed on nighttime data.

There are several other interesting features about the volcano light in Figure 7-30. First, a black oversaturation line can be seen to the right of the light spot in the center of the rings. The line is to the right because as the spacecraft moves southward during this picture, the sensor is scanning from the spacecraft's right to left. This gives the left to right over-saturation line on the picture when oriented with north at the top.

There are two rings surrounding the volcano light source. The inner ring looks like butterfly wings. If we assume that ice crystals between the light source and the spacecraft sensor are causing refraction of that light source (the butterfly), then by using Figure 7-31 we can calculate the altitude of the ice crystals to be 58 nm. This is the height at which noctilucent clouds typically are found. Conover [27] felt that a much better explanation could be given through the equation [Humphreys, "Physics of the Atmosphere," P. 551]:

$$\sin \theta = (n + 0.22) \lambda/2a \qquad (\text{Eq } 7\text{-}3)$$

where θ is the radius of one of the rings and n is the number of the same ring, counting outward. Substituting the measured angular radii for θ, the number of the ring for n and 0.6 μm for the wavelength, λ, of light, the equation can be solved for a, the size of particles causing the corona. Conover found a particle diameter of 17 μm for the inner ring and 18 μm for the outer ring. He speculates that solid particles of that size are present over volcanoes and oil fires to cause corona. Additionally, since narrow light spectra cause more pronounced corona, and volcanoes are strong emitters in the red, then these facts add to the conclusion that corona cause the rings.

The problem is in explaining what causes the missing segments of
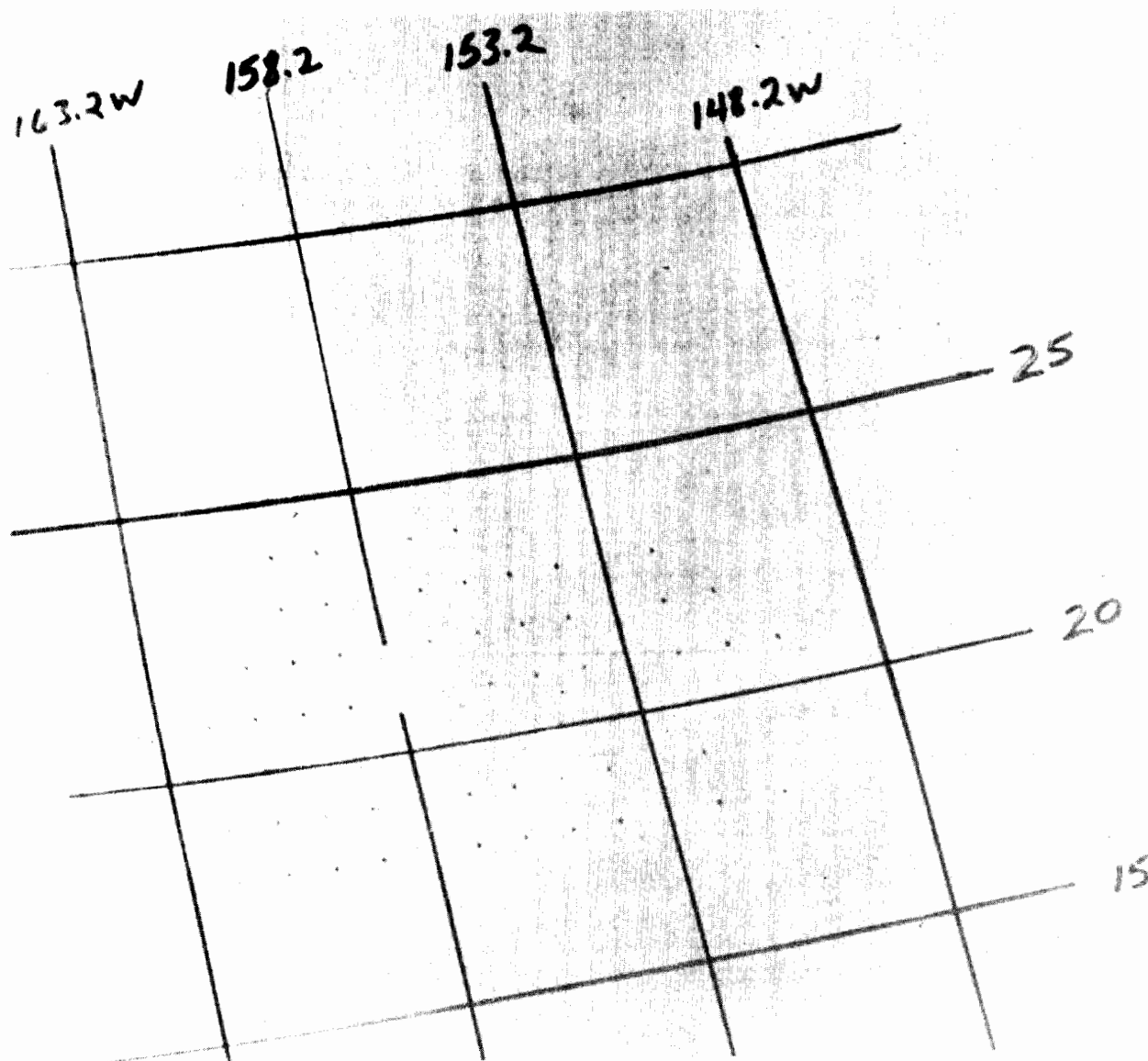
Fig 7-30. Volcano. 28 Oct 1970, 2525/783, HR, Norm, Norm, Off.

the inner ring. The missing seg-
ments do not align with the magnetic
field lines either.

Another possible explanation is
that of internal reflections within
the sensor optics. The fact is,
however, that no complete answer

has been found to the butterfly and
outer ring of volcano and oil fire
phenomena.

H. Conclusion

The examples given already in
this Technical Report have demonstrated

NOCTILUCENT CLOUD DETECTION
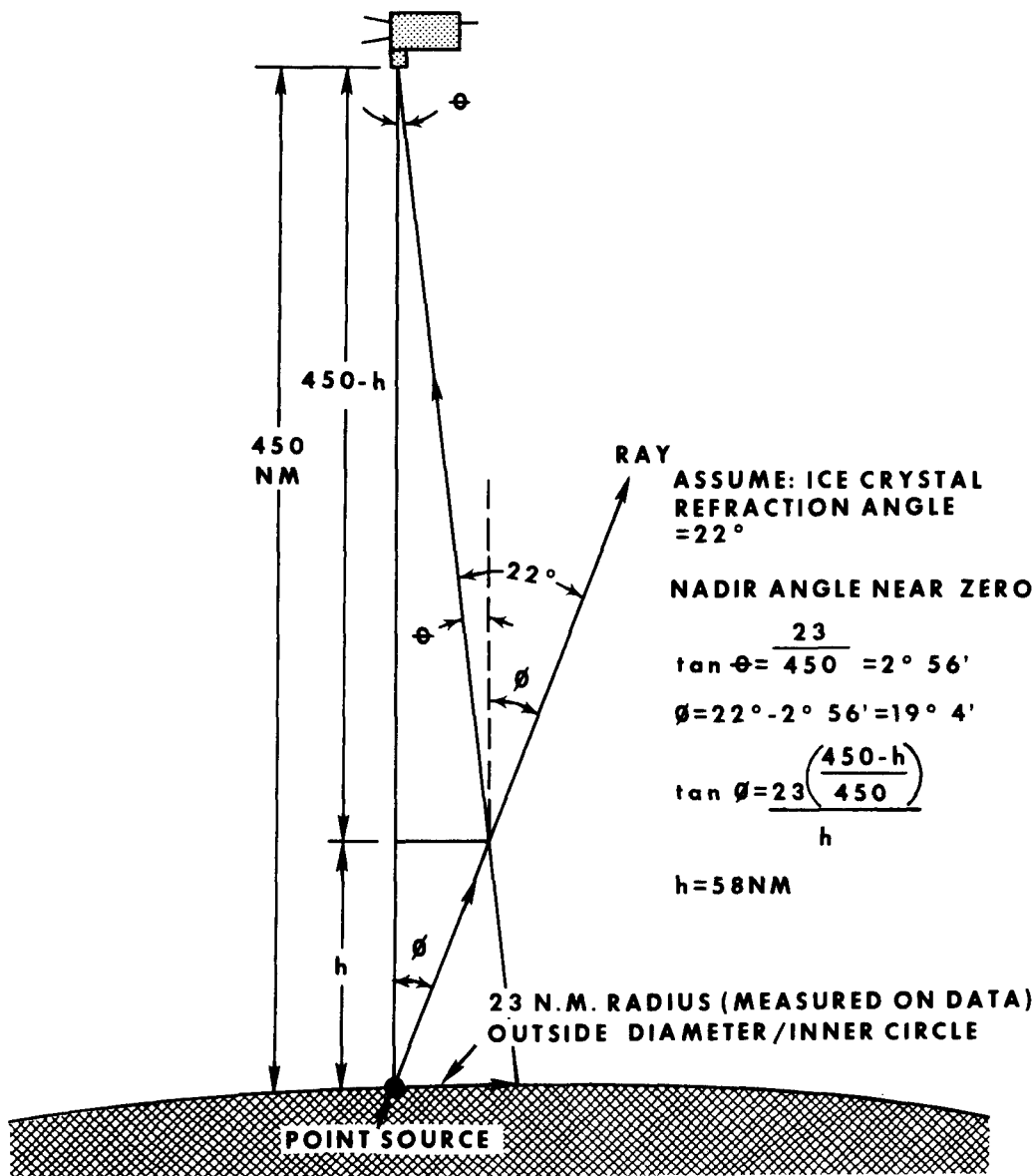
Fig 7-31. Noctilucent cloud detection.

a wide variety of applications for DMSP imagery. Many more applications are possible. A fairly lengthy list of possibilities has been suggested by the meteorologists at the Air Force Eastern Test Range [33]. This list is presented below as Table 7-2. Many further uses will surely be found for data from the current DMSP system. Even more uses will emerge for data from future, more advanced, systems.

I. Meteorology
   A. Clouds
      1. Cloud Location
      2. Cloud Tops
      3. Cloud Patterns
      4. Cloud Movement
      5. Cloud Development
      6. Cloud Dissipation
      7. Invisible Clouds
   B. Systems
      1. Frontal/VTPR (Vertical
Temperature Profile Radiometer)
      2. Easterly Waves
      3. Positive Vorticity Advec-
tion (PVA)
      4. ITCZ (Development/
Dissipation)
      5. Convergent Lines
      6. Squall Lines
      7. Screaming Eagles
      8. TROFS/VTPR
   C. Wind
      1. Low Level Direction/Speed
         a. Streamlines
         b. Lee Waves
         c. Open Cell
         d. Closed Cell
         e. Patterns
         f. Systems
      2. Upper Level.
         a. Billow Clouds
         b. Transverse Bands
         c. Plumes
         d. Streaks
         e. Lee Waves
         f. Systems
   D. Precipitation
      1. Rain
         a. Frontal-Mid-Latitude
         b. Tropical
         c. Convective
         d. Easterly Wave
         e. Screaming Eagles
         f. Typhoon/Hurricane
      2. Snow
         a. Depth
         b. Coverage
         c. Runoff
      3. Modification
         a. Seeding
         b. Development/Dissipa-
tion
   E. Severe Weather
      1. Typhoon/Hurricane
         a. Development
         b. Intensity (wind/
precipitation)
         c. Movement
         d. Dissipation
      2. Thunderstorms/Tornadoes
         a. Convective (Develop-
ment/Dissipation)

      b. Frontal
      c. Squall Lines
      d. ITCZ
   3. Turbulence
      a. Billow Clouds
      b. Lee Waves
      c. Deep Convection
      d. Patterns
   F. Miscellaneous
      1. Pollution
         a. Air, Surface, Upper Air
         b. Water
      2. Lightning
      3. Gravity Waves
      4. Dust

II. Oceanography
   A. Surface Temperature, Currents
   B. Wave Heights
   C. Iceberg Detection/Forecast
   D. Ice Mapping
   E. Fish Detection
   F. Ice Flow/Routes

III. Geophysics
   A. Aurora
      1. Communication
      2. Spacecraft Effects
      3. Solar Relations
      4. Density Anomalies
      5. Weather Effects

IV. Earth Resources
   A. Forest Fires
   B. Forest Mapping
   C. Energy Crisis (Use/Depletion/
Sources)
   D. Vegetation Estimation/Depletion
   E. Crop Harvest (Rice/Sugar Cane)
   F. Oil Refineries/Gas Fields.

V. Miscellaneous
   A. Volcanoes
   B. Anthropology
   C. Light Pollution
   D. City Planning
   E. River Runoff
   F. Locust Movement

Table 7-2. List of potential DMSP applications (military and civilian).

REFERENCES

[1]   Headquarters Space and Missile Systems Organization, Air Force Systems
       Command, USAF: "Block 5 Operating Procedures for Tactical Sites,"
       Revision C, 15 Sep 1973, 137 pp.

[2]   Westinghouse Electric Corp: "Remote Subsystem for Block 5 Display Seg-
       ment," EX96X2-2, 30 July 1971, 232 pp.

[3]   Maj A. R. Coburn: "Three Dimensional Nephanalysis," AFGWC Technical
       Note 70-9, AFGWC, Offutt AFB, NE, 15 Mar 1970, 45 pp.

[4]   R. K. Anderson and A. H. Smith: "Application of Meteorological Satellite
       Data in Analysis and Forecasting." Supplement No 1 to ESSA Technical
       Report NESC 51 (Also issued as Air Weather Service Technical Report No.
       212), Nov 1971, 72 pp.

[5]   Headquarters Air Weather Service/DNT, Military Airlift Command, USAF:
       "Data Acquisition and Processing Program (DAPP) User's Guide," Volume II,
       15 April 1971, 78 pp.

[6]   Headquarters Air Weather Service/DNT, Military Airlift Command, USAF:
       "Data Acquisition and Processing Program (DAPP) User's Guide," Volume I,
       15 April 1971, 150 pp.

[7]   J. N. Howard: "Transmission and Detection of Infrared Radiation," In:
       Handbook of Geophysics and Space Environments, Air Force Cambridge
       Research Laboratories, Office of Aerospace Research, USAF, 1965, pp.
       10.1 - 10.6.

[8]   Air Weather Service, Military Airlift Command, USAF: "Use of the Skew T,
       Log P Diagram in Analysis and Forecasting," AWS Manual 105-124, 15 July
       1969, 138 pp.

[9]   Maj L. G. Dickinson and Capt S. E. Boselly, III: "Comparison of Actual
       to Indicated Temperatures for W and MI Data," Unpublished study, 11 Dec
       1972, 3 pp.

[10]   Capt S. E. Boselly, III; Capt W. S. Burgmann; and Capt D. D. Waltman, Jr;
       "The Use of Fictitious Display Settings for Acquiring Additional Data,"
       Unpublished Study, Mar 1973, 17 pp.

[11]   R. K. Anderson, Capt J. P. Ashman, F. E. Bittner, Maj G. R. Farr, E. W.
       Ferguson, V. J. Oliver, and A. H. Smith: "Application of Meteorological
       Satellite Data in Analysis and Forecasting," AWS Technical Report 212
       (Also issued as ESSA Technical Report NESC 51), June 1969, 230 pp.

[12]   Capt R. W. Skidmore and J. F. W. Purdom: "Application of Meteorological
       Satellite Data in Analysis and Forecasting," Supplement No. 2 to ESSA
       Technical Report NESC 51 (Also issued as Air Weather Service Technical
       Report No. 212), March 1973, 62 pp.

[13]   R. K. Anderson, Capt J. P. Ashman, Maj G. R. Farr, W. E. Ferguson, G. N.
       Isayeva, V. J. Oliver, F. C. Parmenter, T. P. Popeva, Capt R. W. Skidmore,
       A. H. Smith, and N. F. Veltishchev, edited by R. K. Anderson and N. F.
       Veltishchev: "The Use of Satellite Pictures in Weather Analysis and
       Forecasting," World Meteorological Organization Technical Note No. 124
       (Revised version of Technical Note No. 75), WMO-No. 333, 1973, 292 pp.

Appendix 1

[14] F. E. Bittner and Cdr K. W. Ruggles: "Guide for Observing the Environment with Satellite Infrared Imagery," NWFR F-0970-158, Project FAMOS Hillcrest Heights, MD, Sep 1970, 478 pp.

[15] U. S. Department of Commerce, NOAA, EDS: "Daily Weather Maps Weekly Series," April 16-22, 1973, 8 pp.

[16] J. L. McLucas: "Remarks by the Honorable John L. McLucas, Under Secretary of the Air Force, Announcing the Data Acquisition and Processing Program," United States Air Force News Release, The Pentagon, 6 Mar 1973, 12 pp.

[17] S. Fritz, L. Hubert, and A. Timchalk: "Some Inferences from Satellite Pictures of Tropical Disturbances," Monthly Weather Review, Vol 94, No. 4, 1966, pp 231-236.

[18] V. F. Dvorak: "A Technique for the Analysis and Forecasting of Tropical Cyclone Intensities from Satellite Pictures," NOAA Technical Memorandum NESS 45, February 1973, 19 pp.

[19] Capt C. P. Arnold, Jr: "Tropical Cyclone Positioning and Intensity Analysis Using Satellite Data," 1 WW Pamphlet 105-10, 25 April 1974, 116 pp.

[20] V. J. Oliver and J. F. W. Purdom: "Mesoscale Convective Processes in the Tropics as Revealed by Satellite Imagery," Abstract in the Bulletin of the American Meteorological Society, Vol. 54, No. 12, December 1973, p 1304.

[21] Maj H. W. Brandli: "Cumulus Cloud Lines or Streets near the Equator," 1 Oct 1970, Unpublished.

[22] Capt F. H. Wells: "The Use of Small Tropical Cumulus to Define Gradient-Level Flow," August 1973 Draft, In Press, 18 pp.

[23] J. F. W. Purdom: "Satellite Imagery Applied to the Mesoscale Surface Analysis and Forecast," Abstract in the Bulletin of the American Meteorological Society, Vol 54, No. 12, December 1973, p 1304.

[24] F. C. Parmenter: "Observing and Forecasting Local Effects from Satellite Data," Abstract in the Bulletin of the American Meteorological Society, Vol 54, No. 12, December 1973, p 1303

[25] J. H. Conover: "Anomalous Cloud Lines," Journal of the Atmospheric Sciences, Vol. 23, No. 6, November 1966, pp 778-785.

[26] J. H. Conover: "New Observations of Anomalous Cloud Lines," Journal of the Atmospheric Sciences, Vol. 26, No. 5, Part 2, September 1969, pp 1153-1154.

[27] J. H. Conover: Personal Communication, "Interpretation of DAPP Products," 14 Sep 1971, 3 pp.

[28] Maj H. W. Brandli and Capt F. Lombardo, "High Level Wave Clouds not Associated with Terrain (Billows)," 1970, unpublished.

[29] Maj L. G. Dickinson, Maj H. W. Brandli, and Maj F. Lombardo, "Determination of Wind Velocity from Satellite Observed Billow Clouds," Abstract in EOS, Vol. 54, No. 4, April 1973, p 289.

[30] Capt S. E. Boselly, III, "A Study of High-Level Wave Clouds Induced by Strong Vertical Shear," 26 March 1973, unpublished draft, 18 pp.

[31] Z. Skera, "Helmholtz Waves in a Linear Temperature Field with Vertical Wind Shear," Journal of Meteorology, Vol. 5, 1948, pp 93-102.

[32]   E. R. Reiter, Jet Stream Meteorology, University of Chicago Press, 1963, 515 pp.

[33]   STAFFMET Section, Detachment 11, 6 Weather Wing, Air Weather Service, Military Airlift Command, USAF: "Defense Meteorological Satellite Program (DMSP)," 1974, 15 pp.

ACRONYMS AND ABBREVIATIONS

AFCRL		Air Force Cambridge Research Laboratories
AFGWC		Air Force Global Weather Central
AMS		American Meteorological Society
APT		Automatic Picture Transmission
ASAGC		Along scan automatic gain control
ATS		Applications technology satellite
AVCS		Advanced vidicon camera system
AVE		Aerospace vehicle electronics
AWS		Air Weather Service
BI		Brilliance inversion
β		Sensor scan angle
CDO		Central dense overcast
CRT		Cathode-ray tube
D/A		Digital-to-analog
DAPP		Data Acquisition and Processing Program (Now DMSP)
DDS		Data display segment
DFS		Digital facsimile system
DMSP		Defense Meteorological Satellite Program
DRIR		Direct readout infrared
DRSR		Direct readout scanning radiometer
DSAP		Defense Systems Application Program (Now DMSP)
DW		Half data width
ERT		Effective radiative temperature
ESSA		Environmental Science Services Administration (absorbed by NOAA)
	also	Environmental survey satellite
ETS		Equivalent temperature setting
Exp C		Expand center
Exp L		Expand left
Exp R		Expand right
FNWC		Fleet Numerical Weather Central
FTV		Flight test vehicle
GOES		Geostationary operational environmental satellite
High Enc		High enhancement
HR		High resolution (visual)
IMS		Intermediate maintenance shop
Inv		Invert
ITOS		Improved TIROS operational satellite
JTWC		Joint Typhoon Warning Center

Appendix 2

Low Enh	Low enhance
Low/High Enh	Low/high Enhance
MI	Mode infrared
NASA	National Aeronautics and Space Administration
NESS	National Environmental Satellite Service
NGSDC	National Geophysical and Solar-Terrestrial Data Center
NM	Nautical mile
NOAA	National Oceanic and Atmospheric Administration
Norm	Normal
Off Enh	Off enhance
OT	Orbit time
SAMSO	Space and Missile Systems Organization
SAP	Sensor AVE package
SESS	Space environmental support system
Sig Proc No 1	Signal processor Number 1
Sig Proc No 2	Signal processor Number 2
SRP	Selective reconnaissance program
SSB	Supplemental sensor B
SSE	Supplemental sensor E (vertical temperature)
SSJ	Supplemental sensor J (energetic electrons)
SSJ/2	Supplemental sensor J/2 (improved SSJ)
SSL	Supplemental sensor L (lightning)
TIROS	Television and infrared observation satellite
TOS	TIROS operational satellite
USAFETAC	United States Air Force Environmental Technical Applications Center
VHR	Very high resolution (visual)
VHRR	Very high resolution radiometer
VTPR	Vertical temperature profile radiometer
WHR	Very high resolution (infrared)
X1	Expand one
X2	Expand two
X4	Expand four
3 D-Neph	Three dimensional nephanalysis

Appendix 2